U.PORTO
FEUP FACULDADE DE ENGENHARIA
UNIVERSIDADE DO PORTO

Lepabe
Laboratory for Process Engineering,
Environment, Biotechnology and Energy

Chemical Engineering Department

Development and Characterization of Titania-based Photocatalysts and their Incorporation in Paint Coatings

Joana Raquel Monteiro Ângelo

Dissertation presented to obtain the degree of
Doctor in Chemical and Biological Engineering
by the
University of Porto

Supervisors:
Adélio Miguel Magalhães Mendes, Full Professor
Luís Miguel Palma Madeira, Associate Professor
Luísa Manuela Madureira Andrade Silva, Assistant Researcher

2016

UNIÃO EUROPEIA
Fundo Europeu de Desenvolvimento Regional
Governo da República Portuguesa
FCT Fundação para a Ciência e a Tecnologia
MINISTÉRIO DA CIÊNCIA, TECNOLOGIA E ENSINO SUPERIOR
POPH QUALIFICAR É CRESCER.
erc European Research Council
Established by the European Commission
PORTUGAL 2020
COMPETE 2020

Acknowledgements

I am grateful to LEPABE, DEQ and FEUP for providing me the conditions to carry out my work. The present work was financially supported by: Project POCI-01-0145-FEDER-006939 (Laboratory for Process Engineering, Environment, Biotechnology and Energy – LEPABE) funded by FEDER funds through COMPETE2020 – Programa Operacional Competitividade e Internacionalização (POCI) – and by national funds through FCT – Fundação para a Ciência e a Tecnologia – within the PhD grant (SFRH/BD/79974/2011).

I would like to thank my supervisors, Professor Adélio Mendes, Professor Miguel Madeira and Dr. Luísa Andrade, for the opportunity of working in such an interesting field and for all the support during my path that embodies this work. Professor Adélio, thank you for believing in me and for helping me to sought out and achieve my objectives. Professor Madeira, I thank your availability and all the helpful discussions. Luísa, thank you for the incentive and understanding in the most crucial moments of this journey.

I would like to thank Professor Regina Moreira for welcoming me in her research group and for providing me with all the means and materials necessary to accomplish my work. To all the members of LEMA for all the support and for welcoming me with an open heart, making me feel part of their group. A special acknowledgement to Vanessa and to Carolina and her family for receiving me so well and for all their friendship.

I would like to thank all my laboratory colleagues for the friendship, support and for all the shared knowledge. Especially to César Águia, Daniel Ferreira, Joana Cabral, Roberto Magalhães and Vera Gonçalves, for accompanying me throughout this long journey!! I would also like to thank Cecilia Pedrero, Margarida Catarino and to Tânia Lopes for the help and fruitful discussions. For my girls, Ana Pereira, Andreia Cruz, Isabel Mesquita, Paula Dias, Rute Santos and Suélen Amorim, I want to thank for their affection and for all the good moments that we spent together. And to show gratitude to Pedro Magalhães for the scientific discussions and for all the friendship throughout these years.

To all my friends, a sincere thank you for all the patience, care and good moments cherished together. To Rui and Catarina, a special recognition for being a part of my life.

To my parents, my gratefulness for being the root of who I am and for all the love and support during all my life. To my dear sister, thank you for being my example and for being my shelter.

To my little prince Hugo and my little princess Leonor, thank you for making me feel so special!

And to you, Pedro, a simple "thank you" is not enough... Since the first day you have encouraged, believed and supported my choice. Thank you for all the love, care and support and for making me smile every day.

To my beloved nephews …

Preface

The present work was developed in the Laboratory for Process Engineering, Environmental, Biotechnology and Energy (LEPABE), in the Chemical Engineering Department of the Faculty of Engineering of the University of Porto (FEUP), between 2012 and 2016 and under the FCT grant SFRH/BD/79974/2011.

During my PhD a straight collaboration was developed with the Laboratory of Energy and the Enviromental Processes (LEMA) in Federal University of Santa Catarina, resulting in an intership of two months in Brazil.

This thesis presents a compilation of four scientific papers, one review and three research papers, and a final chapter with the overall conclusions and perpectives for future work.

Contents

Part I

PART II

PART III

Abstract

In last decades air pollution has been a serious environmental concern. This kind of pollution contributes for human diseases (respiratory, cardiovascular and lung cancer), global warming and induces severe damages in buildings and monuments. Nitrogen oxides (NO_x) are one of the most common pollutants present in the atmosphere, being responsible for the production of tropospheric ozone and acid rains; moreover, it contributes for global warming and human diseases. The concern with air pollution has been motivating the formulation of specific regulations to control the emissions of pollutants. Photocatalysis, and namely solar induced photocatalysis, is being considered a promising strategy for the abatement of pollutants such as NO_x. Therefore, this thesis aimed at a more fundamental understanding of these photocatalytic mechanisms as an approach to obtain more efficient photocatalytic technologies for NO_x abatement.

Photocatalytic paint is a promising route for degrading pollutants under real outdoor conditions. Paints are used as a 3D support for the photocatalyst (TiO_2), allowing a greater amount of nanoparticles to absorb light and contact with pollutants leading to their photodegradation. Photocatalytic paints were formulated incorporating commercial titanium dioxide into a reference paint and tested under laboratory and outdoor conditions. Both laboratorial and outdoor characterization of these photocatalytic paints revealed a very good photocatalytic performance, validating the use of this type of supports for the degradation of air pollutants.

Even if titanium dioxide has been reported as an ideal photocatalyst due to its suitable properties such as non-toxicity, thermal stability, chemically inertness, etc., e^-/h^+ recombination and a reduced light absorption spectrum have been also identified as important drawbacks. To improve the photocatalytic performance, a TiO_2/graphene composite catalyst was developed. Despite the great interest of this kind of composites and the obtained improvements in photocatalytic activity, a deeper understanding of the charge transport phenomenon on the semiconductor and the redox reactions kinetics occurring at its surface is essential. Thus, electrochemical impedance spectroscopy (EIS) was presented as a standard procedure to study the electrical behavior of photocatalytic systems and particularly to evaluate phenomena occurring at

the semiconductor/electrolyte interface. An electrical analogue model was chosen and fitted to the experimental results. The model proved to fit well to the experimental results, allowing obtaining the charge transfer resistance and the space charge capacitance of the photocatalysts. Indeed, this technique allowed discriminating the different charge pathways that control the performance of photocatalysts.

Finally, a design of experiments concerning NO photooxidation on P25 photocatalyst was performed to study the role of the different operating conditions. A phenomenological model able to describe the photocatalytic reactions occurring in a NO photoabatement process was also proposed. This model is based on the adsorption of reagents and products on the active sites of titanium dioxide and considers that surface lattice oxygen radicals $\left(O_s^{\bullet -}\right)$ are the main oxidising species for NO photooxidation. The proposed model was then fitted to experimental values and a good agreement was showed.

Sumário

Nas últimas décadas a poluição atmosférica tem sido uma grande preocupação ambiental. Este tipo de poluição contribui para o aparecimento de doenças (associadas ao sistema respiratório, cardiovascular e cancro de pulmão), aquecimento global e pode também provocar danos estruturais em edifícios e monumentos. Os óxidos de azoto (NO_x) são dos poluentes mais comuns na atmosfera, sendo responsáveis pela produção de ozono troposférico, chuvas ácidas, assim como pelo aquecimento global e aparecimento/agravamento de doenças. A preocupação com a poluição atmosférica motivou a formulação de normas específicas para controlar a emissão destes poluentes. A fotocatálise, nomeadamente a fotocatálise induzida por luz solar, é considerada uma estratégia promissora para a degradação de poluentes como os NO_x. Assim, esta tese propõe uma compreensão mais fundamental destes mecanismos fotocatalíticos com o objetivo de obter tecnologias mais eficientes para a degradação dos NO_x.

As tintas fotocatalíticas são suportes promissores para a degradação de poluentes em condições reais, de exterior. As tintas funcionam como um suporte 3D para o fotocatalisador (TiO_2), permitindo que as nanopartículas absorvam a luz e contactem com os poluentes, degradando-os. Estas tintas foram formuladas incorporando dióxido de titânio comercial numa tinta de referência e testadas sob condições laboratoriais e reais de exterior. Esta caracterização revelou um bom desempenho fotocatalítico destas tintas, validando o uso deste tipo de suportes para a degradação de poluentes atmosféricos.

Apesar do dióxido de titânio ser descrito como um fotocatalisador ideal por ser não-tóxico, termicamente estável, quimicamente inerte, etc., a recombinação dos pares e^-/h^+ e a sua reduzida capacidade de absorção do espectro solar foram identificadas como desvantagens relevantes. Para melhorar o desempenho fotocatalítico, foi preparado um catalisador compósito de TiO_2/grafeno. Apesar do grande interesse deste tipo de compósitos e do aumento da atividade fotocatalítica obtido, é essencial um conhecimento mais detalhado sobre o fenómeno de transporte de carga no semicondutor assim como das cinéticas das reações que ocorrem na sua superfície. Desde modo, a espectroscopia de impedância eletroquímica (EIS) foi apresentada como um procedimento padrão para estudar o comportamento elétrico dos sistemas fotocatalíticos, e em particular para avaliar os fenómenos que ocorrem na interface semicondutor/eletrólito. Foi escolhido um análogo elétrico equivalente para ajustar os resultados experimentais. O modelo demonstrou ajustar bem os resultados experimentais, permitindo obter a resistência à transferência de carga e a capacitância da "*space charge*" dos fotocatalisadores. De facto, esta técnica permitiu discriminar os diferentes mecanismos de transferência de carga que controlam o desempenho dos fotocatalisadores.

Por fim, foi realizado um planeamento de experiências relativo à foto-oxidação do NO usando o fotocatalisador P25 para se estudar o papel das diferentes condições operatórias. Foi proposto um modelo fenomenológico inovador capaz de descrever as reações fotocatalíticas que ocorrem num processo de fotoabatimento de NO. Este modelo baseia-se na adsorção dos reagentes e produtos em centros ativos do dióxido de titânio e considera os radicais oxigénio da estrutura do TiO_2 $\left(O_s^{\bullet -}\right)$ como as principais espécies oxidantes. O modelo proposto foi ajustado aos valores experimentais e uma boa concordância foi mostrada.

Figure Captions

Table Captions

List of Abbreviations and Symbols

Variables	Definition	Units
A	area	m^2
A'	constant of proportionality	
a_V	active surface area per unit of reactor volume	m^{-1}
b	adsorption affinity constant	bar^{-1}
C_{H_2O} or $[H_2O]$	water concentration	$mol \cdot m^{-3}$
C_i	concentration of specie i	$mol \cdot m^{-3}$
C_{NO} or [NO]	NO concentration	ppm or $mol \cdot m^{-3}$
C_{NO_2} or $[NO_2]$	NO_2 concentration	ppm or $mol \cdot m^{-3}$
C_{SC}	space charge capacitance	F
C_{TiO_2}	concentration of active site on TiO_2 surface	$mol \cdot m^{-2}$
$C_{TiO_2\,free}$	concentration of free active sites on TiO_2 surface	$mol \cdot m^{-2}$
d	Model parameter	
D_{TiO_2}	Fraction of active photocatalyst	$g \cdot g^{-1}$
E	energy	J
E_a	activation energy	$J \cdot mol^{-1}$
E_{BG}	bandgap energy	J
E_C	conduction band energy	J
E_F	Fermi level energy	J
E_V	valence band energy	J
G_{e^-}	electron generation term	$m^{-3} \cdot s^{-1}$
H	height of reactor	m^{-1}
I	Irradiance	$W \cdot m^{-2}$
I_0	Incident photon flux	$m^{-2} \cdot s^{-1}$
K	adsorption equilibrium constant	$m^3 \cdot mol^{-1}$
k	reaction rate constant	
k'_A	reaction rate constant of specie A	$m^3 \cdot mol^{-1} \cdot s^{-1} \cdot g^{-1}_{catalyst}$
k'_B	reaction rate constant of specie B	$s^{-1} \cdot g^{-1}_{catalyst}$
K'_{H_2O}	adsorption equilibrium constant of water	$m^3 \cdot mol^{-1}$

K'_{NO}	adsorption equilibrium constant of NO	$m^3 \cdot mol^{-1}$
$K'_{\mathrm{NO_2}}$	adsorption equilibrium constant	$m^3 \cdot mol^{-1}$
k_0	pre-exponential factor	
m_e^*	effective mass of electrons	kg
m_h^*	effective mass of holes	kg
N_{C}	density-of-states at the conduction band	m^{-3}
$n_{\mathrm{e^-}}$	density of electrons	m^{-3}
$n_{\mathrm{h^+}}$	density of holes	m^{-3}
n_{i}	intrinsic carrier concentration	cm^{-3}
N_{V}	density-of-states at the valence band	m^{-3}
q	adsorbed concentration	$mol \cdot kg^{-1}$
Q	volumetric flow rate	$dm^3 \cdot min^{-1}$
q_j^{calc}	adsorbed concentration calculated	$mol \cdot kg^{-1}$
$q_j^{\exp}$	experimental adsorbed concentration	$mol \cdot kg^{-1}$
q_m	saturation adsorbed concentration	$mol \cdot kg^{-1}$
r	reaction rate	$mol \cdot m^{-2} \cdot s^{-1}$
R_{CT}	charge transfer resistance	Ω
RH	relative humidity	%
$-r_{\mathrm{NO}}$	reaction rate of NO	$mol \cdot m^{-3} \cdot s$
R_{s}	series resistance	Ω
S	selectivity	%
$S\mathrm{g}$	specific surface area	$m^{-2} \cdot g^{-1}$
T	temperature	K
V	applied Potential	V
v	linear velocity	$m \cdot min^{-1}$
W	Warburg element	Ω
W	widht of reactor	m^{-1}
X_{NO}	conversion of NO	%
$\mathrm{Z_{imag}}$	Imaginary part of impedance	Ω
$\mathrm{Z_{Re}}$	Real part of impedance	Ω
$\lvert Z \rvert$	Magnitude impedance	Ω

Greek symbols	Definition	Units
α	light absorption coefficient	m^{-1}
ΔH_i	enthalpy of the reaction	$J\cdot mol^{-1}$
ε_r	dielectric constant of the semiconductor	
η_{air}	dynamic viscosity of air	$kg\cdot m^{-1}\cdot s^{-1}$
η_{inj}	injection efficiency	%
θ_A	fractional coverage of the surface by A	
θ_B	fractional coverage of the surface by B	
κ	radiation absorption coefficient of photocatalyst	m^{-1}
λ	wavelength	nm
μ_{air}	kinematic viscosity	$m^2\cdot s^{-1}$
ν	frequency	Hz
ρ	density	$g\cdot dm^{-3}$
τ	residence time	s
τ_{e-}	electron lifetime	ms
χ	dimensionless factor	
Φ	phase shift	degree
ϕ_λ	primary quantum yield	$mol\cdot W^{-1}\cdot min^{-1}$

Physical constants	Definition	Units
h	Planck constant	6.63×10^{-34} J·s
k_B	Boltzman constant	1.38×10^{-23} $J\cdot K^{-1}$
q	Charge of electron	1.60×10^{-19} C
R	Universal gas constant	8.31 $J\cdot K^{-1}\cdot mol^{-1}$
ε_0	Permittivity of free space	8.85×10^{-12} $F\cdot m^{-1}$

Abbreviations	Definition
7HC	7-hydroxycoumarin
$CaCO_3$	calcium carbonate
CB	conduction band
CCD	central composite design

COU	coumarin
e^-	electrons
EDS	energy dispersive X-Ray spectroscopy
EIS	electrochemical impedance spectroscopy
FTO	fluorine doped tin oxide
h^+	holes
J-V	photocurrent density-potential
NO	nitrogen monoxide
NO_2	nitrogen dioxide
NO_2^-	nitrite
NO_3^-	nitrate
NO_x	nitrogen oxides
$O_2^{\bullet -}$	superoxide anion
$OH^{\cdot}$	hydroxyl radical
O_s^-	surface lattice oxygen radical
PEC	photoelectrochemical cell
RHE	reversible hydrogen electrode
RSM	response surface methodology
SC	semiconductor
SEM	scanning electron microscopy
TCO	transparent Conducting Oxide
TiO_2	titanium dioxide
UVCON	accelarated agging test
VB	valence band
XRD	X-ray diffraction

Subscripts	**Definition**
act	active
ads	adsorption
des	desorption
in	inlet
out	outlet

PART I: Chapter 1

Introduction

Introduction[1]

Presently, urban environments are facing serious problems concerning air pollution, mainly due to exhaust gases from traffic and burning fuels in industries, leading to a major environmental issue on a global scale. This has a great impact on human health, animal life, plants and climate. There are two main air pollutants sources: natural sources, such as volcanic eruption, soil erosion, forest fires; and anthropogenic sources, in particular emissions resulting from human actions. The latter is actually the most active cause of air quality degradation. In particular, urban areas present a high level of air pollution mainly due to the intensification of industrial activity and the increasing number of motor vehicles in circulation [1].

Air pollutants can be classified according to their origin as primary or secondary pollutants. Primary pollutants are those that are emitted directly by the sources to the atmosphere, like carbon monoxide (CO), sulfur dioxide (SO_2), nitrogen oxides (NO_x) and particles (PM10 and PM2.5). Secondary pollutants are formed from chemical reactions occurring in atmosphere, such as tropospheric ozone (O_3), nitric acid (HNO_3) and sulfuric acid (H_2SO_4) [1, 2]. Nitrogen oxides will be the focus of this review; they are derived naturally from volcanic activity, transported by diffusion from high to low atmosphere, and from the decomposition of organic matter by microbial and solar action. However, a very significant fraction of emissions of these pollutants results from human activities. Among the anthropogenic sources of NO_x emissions, the combustion processes in stationary and mobile units are very relevant. The most common nitrogen oxides are nitrogen monoxide (NO) and nitrogen dioxide (NO_2). There are three basic mechanisms leading to the formation of nitrogen oxides during combustion and thus three types of NO_x are identified: prompt NO_x, fuel NO_x and thermal NO_x [3, 4]. Prompt NO_x is formed from hydrocarbon radicalar reactions with N_2 species. The corresponding reactions are summarized by the *Fenimore* mechanism, as shown in Equations 1.1-1.3 [3, 5].

---

[1] Adapted from Ângelo, J.; Andrade, L.; Madeira L.M.; Mendes, A., An overview of photocatalysis phenomena applied to NO_x abatement, Journal of Environmental Management 129 (2013), pp 522-539.

$$CH + N_2 \rightleftarrows HCN + N \qquad 1.1$$

$$C + N_2 \rightleftarrows CN + N \qquad 1.2$$

$$N + O_2 \rightleftarrows NO + O \qquad 1.3$$

Formation of prompt NO_x occurs during the rich combustion, where high concentrations of hydrocarbons are present and, therefore, more likely to form the corresponding radical. Activation energies of these reactions are relatively low, occurring very quickly during combustion. Fuel NO_x is formed by oxidation of nitrogen compounds present in the fuel. The fuel contains nitrogen compounds with N-H and C-N bonds. During combustion, the ring structures are broken and species such as HCN, NH_3 or $NH_2^{\bullet}$ and $CN^{\bullet}$ are formed, which by reaction with O_2 originate NO_x; fuel NO_x only depends on the nitrogen content in the fuel [3, 5]. Thermal NO_x is formed by high-temperature (normally above 1600 °C) reactions between nitrogen and oxygen. The reactions can be summarized by the *Zeldovich* mechanism, as shown in Equation 1.3-1.4 [3, 5].

$$N_2 + O \rightleftarrows NO + O \qquad 1.4$$

Thermal NO_x formation increases with temperature in the flame zone and thus is strongly dependent on the combustion temperature.

In a combustion process, the three types of NO_x and the radicals involved in their formation may interact with each other. The importance of each type of NO_x in the total amount of pollutants emitted depends on the combustion temperature, residence time, ratio air/fuel and type of fuel used.

NO_x pollution is a serious environmental concern. This kind of pollution is responsible for well-known effects that have been widely discussed as production of tropospheric ozone, acid rains, global warming and human diseases, particularly respiratory and in the immune systems – Figure 1.1. This brings specific regulations to control NO_x emissions, established by the US Environmental Protection Agency (EPA) and by the European Environmental Agency (EEA). EPA and EEA established the hourly NO_x air concentration limits at 0.1 ppm [6, 7].

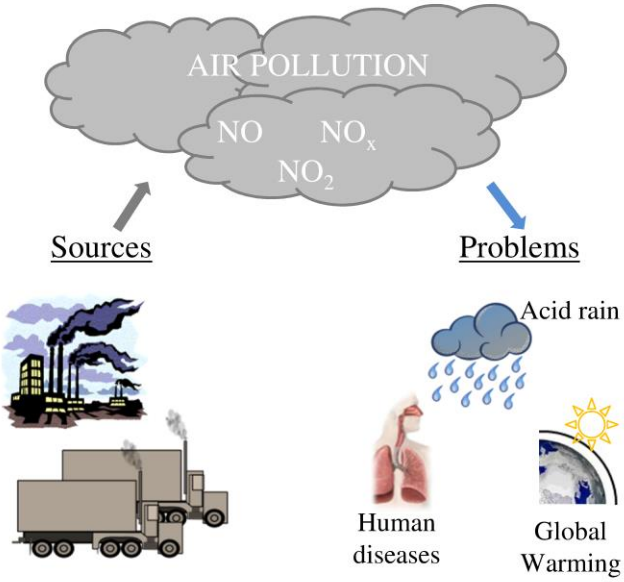

Figure 1.1. Problems and sources associated to NO_x air pollution.

Some methods have been developed and implemented in order to control NO_x emissions, which are divided into primary and secondary methods [8]. Primary methods refer to preventing the formation of NO_x, while the secondary methods are applied to reducing the already formed NO_x. Some prevention methods include the replacement of common fuel by a low-level nitrogen fuel, the usage of fuel additives and the fuel pretreatment. However, combustion control techniques are not enough to ensure the low emissions required by the present legislation and, furthermore, they cannot be used in all situations. If the combustion waste is heterogeneous, secondary treatment methods are required. Selective non-catalytic or selective catalytic reductions are examples of processes used to reduce the NO_x formed [8-10]. An alternative method to decompose this type of pollutants is photocatalysis with titanium dioxide (TiO_2). Thus, in the next sections of this chapter the current approaches of TiO_2 photocatalysis applied to NO_x abatement are summarized according to the following structure. The basic photoelectrochemistry fundamentals will be overviewed and related to the NO_x photoabatement mechanisms to provide a better understanding of the phenomena behind those photocatalytic systems. Then, titanium dioxide photochemistry will be discussed since TiO_2 is the most used semiconductor with photocatalysis for environmental applications and, in particular, for NO_x abatement. The effect of the operational conditions on the photocatalytic activity with titanium dioxide systems will be also briefly analyzed, as well as experimental details about the most used photoreactor designs. Finally, different methods for TiO_2 immobilization will be described to bring to discussion this topic, which strongly limits the photocatalytic process but that is often forgotten.

1.1 Fundamentals of photoelectrochemical processes

Photocatalysis is a photoelectrochemical phenomenon that given its complexity has been interpreted essentially based on empirical knowledge. However, the fundamental understanding gained from the study of photoelectrochemical phenomena in areas such as photoelectrochemical cells for solar fuels production showed to be of great importance for exploring and improving the photocatalytic effect. There are various ways of harvesting solar radiation to produce useful products: devices converting directly solar energy to electrical energy (*e.g.* photovoltaic-solar cells) or to chemical energy (*e.g.* hydrogen, synthesis gas). Those systems are based on photoelectrochemical cells where one or both electrodes are photoactives. A photoelectrochemical (PEC) cell is constituted by a semiconductor (anode) and a counter electrode (cathode), immersed in an aqueous electrolyte solution. When exposed to sunlight, the semiconductor absorbs photons with sufficient energy to inject electrons from the valence band to its conduction band, creating electron-hole pairs [11, 12]. Semiconductor-based photoelectrochemical cells are regarded as an important class of solar energy conversion systems since they offer a simple and efficient way of converting light into electricity, into a fuel or simply for photoabatement of pollutants present in air or in water. Solar energy conversion by semiconductors gained special attention from researchers as a very promising technology since the work by Fujishima and Honda in 1972 [13].

1.1.1 Semiconductors physics

(i) Energy bands

Semiconductors have intermediate electrical conductivities, between those of conductors and insulators, roughly in the range of 10^{-2} to 10^{4} S·cm^{-1}. The energy band diagrams of semiconductors are rather complex. Nevertheless, it is possible to simplify the energy band diagram since only the electrons in the highest almost-filled band (valence band - VB) and the lowest almost-empty band (conduction band - CB) dominate the behavior of the semiconductor. This leads to a simplified energy band diagram for semiconductors as shown in Figure 1.2.

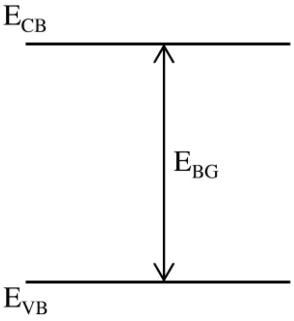

Figure 1.2. Schematic representation of semiconductor energy band.

Semiconductors differ from conductors and insulators since they contain an "almost-empty" conduction band and an "almost-full" valence band. This also means that the transport of charge in both bands has to be considered. The energy difference between conduction and valence edges is the bandgap energy of the semiconductor (E_{BG}) - Figure 1.2. The semiconductor energy bandgap is usually in the range of 1- 4 eV and it is a forbidden energy region or gap in which energy states do not exist – Table 1.1. When semiconductors are irradiated with photons with energy equal or higher than its bandgap energy, electrons (e^-) are excited from the valence to the conduction band, leaving positively charged vacancies in the valence band, called holes (h^+). Both conduction band electrons and valence band holes contribute to electrical conductivity. To be precise, holes actually do not move. It is a neighboring electron that moves to fill the hole, leaving a hole at the place it has just came from; in this way holes appear to move and behave as if they were actual positively charged particles.

Table 1.1. Examples of semiconductors used for photoelectrochemical processes.

Semiconductor	Conductivity type	Optical band gap energy /eV
Si	n,p	1.11
GaAs	n,p	1.42
GaP	n,p	2.26
InP	n,p	1.35
CdS	n	2.42
CdSe	n	1.70
CdTe	n,p	1.50
TiO_2 (rutile)	n	3.00
TiO_2 (anatase)	n	3.20
ZnO	n	3.35

There are two types of bandgaps: direct and indirect bandgaps. The bandgap is called direct if the momentum of electrons and holes is the same in both the conduction band and the valence band – Figure 1.3(a). In case of indirect transitions an electron cannot shift from the lowest-energy state in the conduction band to the highest-energy state in the valence band without a change in momentum. The needed momentum is obtained when the injecting electron absorbs a phonon – Figure 1.3(b). One of the simplest methods for probing whether a bandgap is direct or indirect is to measure the absorption spectrum. For a direct transition it is obtained a parabolic energy structure - equation 1.5:

$$\text{Direct transition: } \alpha = A'\sqrt{h\nu - E_{\mathrm{BG}}} \qquad 1.5$$

where α is the light absorption coefficient, A' is a constant of proportionality, h is the Planck constant and ν is the frequency. Plotting $(\alpha h\nu)^2$ *vs.* $h\nu$ should yield a straight line and the E_{BG} can be determined from the intercept with the abscissa axis. For an indirect transition the relation between α and $h\nu$ is given by equation 1.6:

$$\text{Indirect transition: } \alpha = A'(h\nu - E_{\mathrm{BG}})^2 \qquad 1.6$$

A straight line will be obtained by plotting $(\alpha h\nu)^{1/2}$ *vs.* $h\nu$ [14].

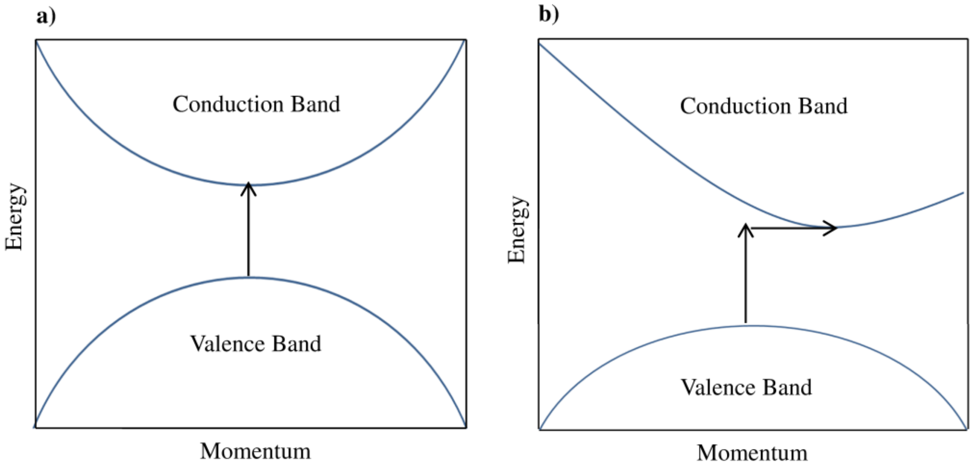

Figure 1.3. Schematic representation of direct (a) and indirect (b) energy band.

(ii) Electron distribution in semiconductors

The number of electrons, n_{e^-}, per unit of volume occupying levels in the conduction band is the integral of the product between the density of states in the conduction band and the Fermi-Dirac distribution over all energies in the conduction band. The Fermi-Dirac distribution function, also called Fermi function, provides the probability of occupancy by an electron at energy level E and in thermal equilibrium (at a constant temperature with no external injection or generation of carriers). The Fermi function is given by equation 1.7.

$$f(E)=\frac{1}{1+\exp\left(\frac{E-E_\mathrm{F}}{k_\mathrm{B}T}\right)} \tag{1.7}$$

The system is characterized by its temperature, T, and Fermi energy, E_F; k_B is the Boltzman constant. However, for energies well above E_F, the exponential term of Equation 1.7 is quite higher than unity and it reduces to the Boltzmann equation ($E-E_\mathrm{F}>>k_\mathrm{B}T$) – equation 1.8.

$$f(E)\approx\exp\left(-\frac{E-E_\mathrm{F}}{k_\mathrm{B}T}\right) \tag{1.8}$$

Since the conduction band energy (E_C) is normally well above the Fermi level the corresponding electron density is given by equation 1.9.

$$n_{e^-} = N_C \exp\left(-\frac{E_C - E_F}{k_B T}\right) \tag{1.9}$$

A similar approach is held for holes, according to equation 1.10.

$$n_{h^+} = N_V \exp\left(-\frac{E_F - E_V}{k_B T}\right) \tag{1.10}$$

N_C and N_V are the density-of-states at the conduction and valence bands, respectively, and they are given by equations 1.11 and 1.12 [14];

$$N_c = 2\left[\frac{2\pi m_e^* k_B T}{h^2}\right]^{3/2} \tag{1.11}$$

$$N_V = 2\left[\frac{2\pi m_h^* k_B T}{h^2}\right]^{3/2} \tag{1.12}$$

where h is the Planck constant and m_h^* and m_e^* are the effective masses of holes and electrons, respectively.

In an undoped (intrinsic) semiconductor in thermal equilibrium, the number of electrons in the conduction band equals the number of holes in the valence band: $n_{e^-} = n_{h^+} = n_i$ (n_i is the intrinsic carrier concentration). The number of charge carriers is therefore determined by the properties of the material itself instead of the amount of impurities. Considering Equations 1.9 and 1.10, the intrinsic carrier concentration is given by equation 1.13.

$$ni = \sqrt{n_{e^-} n_{h^+}} = \sqrt{N_c N_v}\exp\left(\frac{E_v - E_c}{2k_B T}\right) = \sqrt{N_c N_v}\exp\left(\frac{-E_{BG}}{2k_B T}\right) \tag{1.13}$$

For an intrinsic semiconductor, the Fermi Level lies at the mid-point of the bandgap (Figure 1.4(a)) and the energy of its Fermi Level can be calculated as presented in equation 1.14 [15].

$$E_F = \frac{1}{2}(E_v + E_c) + \frac{1}{2}\left(k_B T \ln \frac{N_v}{N_c}\right) \tag{1.14}$$

On the other hand, doping semiconductors means the introduction of deliberate impurity atoms in their structure - extrinsic or impurity doped semiconductor. They can be either n-type or p-type depending if donors (D) or acceptors (A) states are introduced, respectively. The relative position of the band edges, as well as the Fermi level in the bulk of the semiconductor, depends on the doping level. When a semiconductor is doped with donors or acceptor atoms, then the corresponding energy levels are introduced within the called forbidden zone. In case of n-type semiconductors the Fermi level is below the conduction band - Figure 1.4(b) - and in case of p-type semiconductors the Fermi level is above the valence band – Figure 1.4(c). The majority charge carriers for p-type and n-type semiconductors are holes and electrons, respectively.

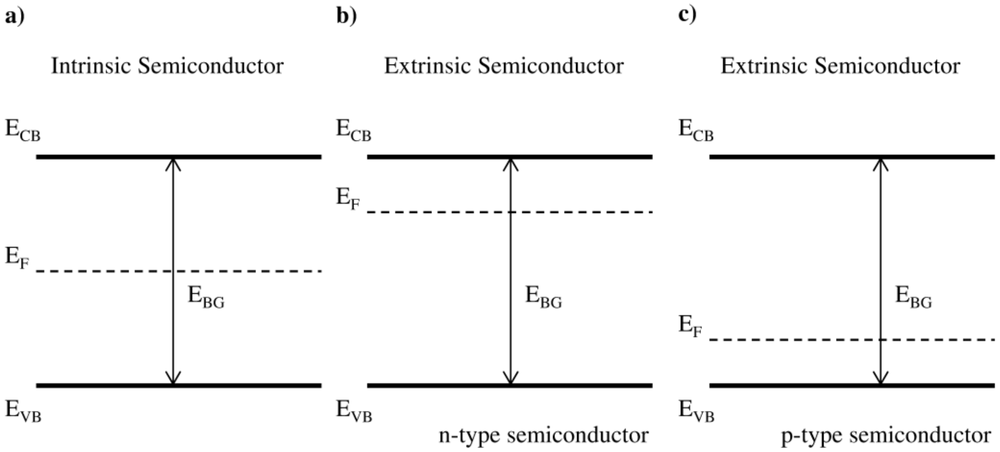

Figure 1.4. Schematic representation of semiconductor energy band – intrinsic (a) and extrinsic semiconductors (b and c).

If the energy level, E_D, introduced by a donor atom is sufficiently close to the conduction band, there will be sufficient thermal energy to allow the extra electron to occupy a state in the conduction band. The donor state will be then positively charged (ionized). On the other hand, if an acceptor state is introduced in the lattice, it will become negatively charged (ionized). Assuming that all donors and acceptors are completely ionized, in n-type materials and in p-type materials one can write respectively $n_{e^-} \approx n_D = N_C e^{-(E_C - E_F)/k_B T}$ and $n_{h^+} \approx n_A = N_V e^{-(E_F - E_V)/k_B T}$. Thus, the Fermi energy is given by equation 1.15 for an n-type semiconductor and by equation 1.16 for a p-type semiconductor[15, 16].

$$E_F = E_C + k_B T \ln\left(\frac{n_{e^-}}{N_C}\right) \qquad 1.15$$

$$E_F = E_V + k_B T \ln\left(\frac{N_V}{n_{h^+}}\right) \qquad 1.16$$

1.1.2 Semiconductor-electrolyte interface

When a semiconductor comes into contact with an electrolyte containing a redox couple, both with different initial chemical potentials, charges are transferred between them until equilibrium is established. The balance of the chemical potentials occurs by transferring charges from the semiconductor to the electrolyte. This produces a space charge layer in the semiconductor, also called a depletion layer since the region is depleted of the respective majority charge carriers (electrons in the case of n-type semiconductors and holes for p-type). Nevertheless, a charged layer also exists in the electrolyte adjacent to the interface with the solid electrode – Helmholtz layer. This layer consists of charged ions from the electrolyte adsorbed on the solid electrode surface. Figure 1.5 shows a diagram for a semiconductor-electrolyte junction [17]. The electrochemical potential of the liquid phase is determined by its redox potential; on the other hand, the electrochemical potential of the semiconductor material is determined by the corresponding Fermi level.

Considering an n-type semiconductor, the Fermi level is typically higher than the redox potential of the electrolyte solution, so electrons move from the semiconductor to the electrolyte solution leaving a positive charge in the space-charge region. In the process, the Fermi level in the semiconductor moves “down” and the process stops when it equals the redox potential of the electrolyte side. This movement is also followed by the conduction band edge, giving rise to an upward band bending – Figure 1.5(a). As the space-charge region is depleted of majority charge carriers - electrons - a depletion layer is formed in this region. In the case of a p-type semiconductor, the Fermi level is lower than the redox potential of the electrolyte solution, so electrons move from the electrolyte solution to the semiconductor leading to accumulation of negative charge in the space-charge region; this causes downward band bending – Figure 1.5(b). As the space-charge region in the semiconductor is depleted of majority charge carriers, in this case holes, a depletion layer is also formed.

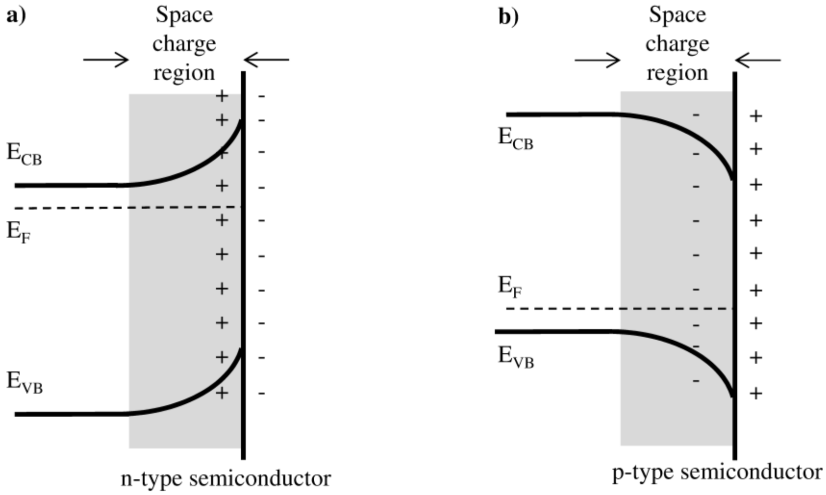

Figure 1.5. Depletion layer for n-type (a) and p-type (b) semiconductors.

Other types of space charges can also be formed in semiconductors: inversion layer, deep depletion layer and accumulation layer. An inversion layer occurs when the number of adsorbed surface charges increases beyond a certain number, the Fermi level crosses the middle of the bandgap and the n-type surface region becomes a p-type or the p-type surface region becomes n-type. A deep depletion layer is usual for materials with large bandgaps, larger than 2 eV, because they have less minority carriers; this means that minority carriers are consumed faster than they are generated. An accumulation layer is formed to compensate the free majority carriers accumulated near the surface. This layer is formed when an excess of positive or negative charges are adsorbed at the surface of n-type or p-type semiconductors, respectively.

When no net excess charge in the interface of a semiconductor is observed – Figure 1.2 – the bands are flat reflecting the potential of zero charge. This potential is called the flat band potential V_{fb} and it is the potential that is necessary to apply to the semiconductor to reduce the band bending to zero. This potential can be determined by several techniques, *e.g.* measurement of the photocurrent onset potential, electrolyte electroreflectance (EER) or Mott-Schottky analysis. Actually, this last technique is the most used. Mott-Schottky is a graphical analysis of the inverse square of space charge capacitance $1/C_{SC}^2$ plotted as a function of the applied potential *V*, yielding a straight line. The space-charge layer capacitance is inversely proportional to the width of the depletion layer. As the depletion layer approaches zero (no band-bending, flat band potential conditions), the capacitance approaches infinity. Hence, $1/C_{SC}^2$ will be zero at the flat band potential; its value is given by the intercept of the straight line on the potential axis, according to equation 1.17:

$$\frac{1}{C_{SC}^2} = \frac{2}{\varepsilon_0 \varepsilon_r q N_\mathrm{D} A^2}\left(V - V_\mathrm{fb} - \frac{k_B T}{q}\right) \qquad 1.17$$

where ε_r is the dielectric constant of the semiconductor, ε_0 is the permittivity of free space, N_D is the donor density (electron donor concentration for an n-type semiconductor and hole acceptor concentration for p-type semiconductor), *q* is the charge of electron, k_B is the Boltzman constant, *T* is the absolute temperature and *A* is the electrode area. The donor density N_D can be calculated from the slope of $1/C_{SC}^2$ *vs.* applied potential *V.*

1.1.3 Photocatalysis

Photocatalysis is one example of a photoelectrochemical process. Actually, all the extensive knowledge obtained during the development of semiconductor photoelectrochemistry during the 1970s and 1980s has greatly biased the development of photocatalysis. For environmental applications, usually TiO_2 anatase is used as semiconductor and water present in air humidity is the electrolyte. Titanium dioxide is an n-type semiconductor with 3.2 eV of bandgap energy – Table 1.1. In this semiconductor, the energy of incident photons have to be greater or equal to the bandgap energy to excite the electrons, corresponding this value mainly to the UV light region.

Photocatalysis principle is the activation of a semiconductor with sun or artificial light. When exposed to sunlight, the semiconductor absorbs photons with sufficient energy to inject electrons from the valence band to its conduction band, creating electron-hole pairs. Those holes have a potential sufficiently positive to generate radicals from water molecules adsorbed onto the semiconductor surface, which can oxidize then organic contaminants. The electrons react with oxygen molecules to form the superoxide anion, $O_2^{\bullet -}$ – Figure 1.6. The photocatalytic efficiency depends on the competition between the process in which the electron reacts with a chemical species on the semiconductor surface and the electron-hole recombination process, which results in heat or radiation release. One aspect of particular interest in this type of catalytic process is the usage of the sun as the energy source. Actually, the sun is our primary source of clean and abundant energy, striking 120 PW of radiation onto the surface of Earth [18-23]. Nevertheless, the possibility of occurring electron-hole recombination greatly limits the photocatalytic activity and thus several efforts are envisaged to allow a more efficient charge carrier separation [24-27].

Photocatalysis is governed by the kinetics of charge carriers and redox reactions that take place at the surface of the photocatalyst. Therefore, the understanding of the electronic processes occurring at the semiconductor nanoparticles level, as well as the dynamics of charge separation/transport and reactive mechanisms in the different interfaces is of great importance. In the semiconductor context, the photocatalysis process is usually interpreted with a band model, where at least two reactions may occur simultaneously: i) oxidation from photogenerated holes and ii) reduction from photogenerated electrons. These processes should occur at the same rate to maintain the photocatalyst mostly electrically neutral. Figure 1.6 shows the following sequence of charge transfer processes responsible for the photocatalytic process:

1. Photons with energy higher than the bandgap of the semiconductor (SC) generate electron-hole pairs in the conduction and valence bands, respectively:

$$\mathrm{SC} \xrightarrow{h\nu} e^{-}_{\mathrm{CB}} + h^{+}_{\mathrm{VB}} \qquad 1.18$$

2. Holes react with water molecules adsorbed on the semiconductor surface, resulting in the formation of hydroxyl radicals:

$$\mathrm{SC}\left(h^{+}_{\mathrm{VB}}\right) + \mathrm{H_2O} \rightarrow \mathrm{SC} + \mathrm{OH}^{\bullet}_{\mathrm{ads}} + \mathrm{H}^{+} \qquad 1.19$$

3. Electrons in the conduction band reduce the adsorbed oxygen to superoxide:

$$SC\left(e^{-}_{CB}\right) + O_{2\ ads} \rightarrow SC + O_2^{\bullet -} \qquad 1.20$$

For a semiconductor to be photochemically active, the potential of the photogenerated valence band hole must be sufficiently positive to generate radicals, which can subsequently oxidize the organic pollutant. The redox potential of the photogenerated conduction band electrons must be sufficiently negative to be able to reduce adsorbed oxygen to superoxide. The surface adsorbed water on the photocatalyst particles is essential to photocatalysis since it provides the electrolyte support needed for the redox reaction promoted by the e^-/h^+ pairs generated by the excited semiconductor.

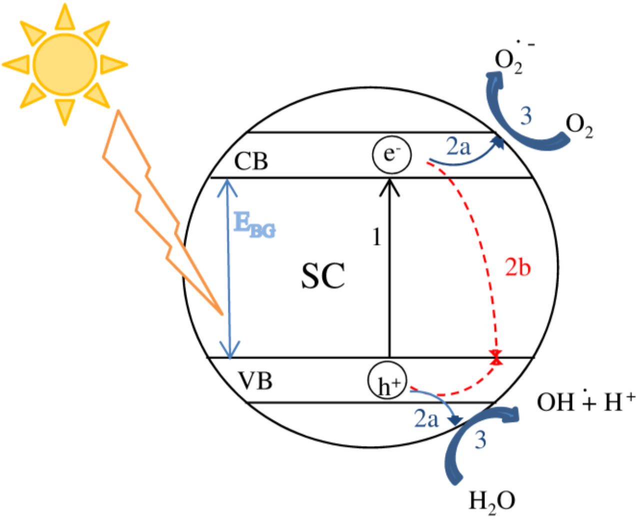

Figure 1.6. Mechanism of photocatalysis with main reaction: electron-hole pair generation (1), charge separation and migration to surface reaction sites (2a) and to recombination sites (2b) and surface chemical reaction on active sites (3).

1.2 NO_x photoabatement

As mentioned throughout this work, a promising approach for decreasing the high levels of nitrogenous oxides NO_x in urban environments is their ability to be photochemically converted to nitrates by heterogeneous photocatalytic oxidation. Even though earlier works focused mainly on the treatment of waste water, heterogeneous photocatalytic oxidation has received particular attention regarding removal of air pollutants in the last years. TiO_2 material has strongly contributed for that due to its excellent photocatalytic properties and, therefore, these characteristics will be discussed below. The effect of the operational conditions on the photocatalysis process for photodegradation of NO_x compounds; experimental details concerning the main photoreactors used for that purpose; as well as an overview of the Langmuir-Hinshelwood model will be also discussed. Besides, it is well known that a variety of experimental materials for NO_x photoabatement were already developed in several research laboratories; nevertheless, they are still not being currently used in real world applications. This is mainly due to difficulties on finding effective ways of immobilizing the developed photocatalysts and thus the immobilization issues will be also discussed. Some real applications will be presented to illustrate that photocatalysis is indeed a promising way for pollutants degradation.

1.2.1 TiO_2 photochemistry

In 1791, titanium dioxide was isolated by the first time by Reverend William Gregor, but the industrial production of this substance only started in the 20th century. Over the years, several studies were developed to improve titanium dioxide properties as a pigment for paints, plastics, paper and synthetic fibers [28, 29]. Titanium dioxide exists in three crystalline forms: anatase, rutile and brookite. However, due to the difficulty of producing brookite crystals in laboratory, only anatase and rutile are usually considered. For photocatalysis, anatase has been widely used because it presents higher photocatalytic activity and it is easier to prepare. However, rutile is the most thermodynamically stable crystal structure of titanium dioxide, whereas anatase and brookite are considered meta-stable. In fact, anatase and brookite phases convert to rutile upon heating, while the reverse process is not possible [25, 30-35].

As mentioned before, when TiO_2 is subjected to irradiation with photons of energy higher than its bandgap (3.2 eV for anatase and 3.0 eV for rutile – Table 1.1), the generated electron–hole pairs can induce the formation of reactive oxygen and hydroxyl species during the photocatalytic process. Indeed, titanium dioxide is a light-sensitive oxide which absorbs electromagnetic radiation in the ultraviolet region [23, 25]. From the available semiconductors that can be used as photocatalysts (Table 1.1), TiO_2

is generally considered to be the best material [18, 25, 36]. In fact, titanium dioxide is close to being an ideal photocatalyst, exhibiting almost all of the required properties for an efficient photocatalytic process, only with the important drawback of not absorbing visible light. Furthermore, TiO_2 is non-toxic, thermally stable, chemically inert, photostable (i.e. not prone to photocorrosion), readily available and relatively cheap. It shows band edges well positioned, exhibiting strong oxidizing power at ambient temperature and pressure (3.0 V) and the photogenerated electrons are able to reduce oxygen to superoxide (-0.2 V).

Going back to Figure 1.6, there are three key processes for an efficient photocatalytic process using TiO_2 semiconductor. The first key process (i) is the ability of absorbing photons to generate electron-hole pairs. This is directly determined by the bandgap of the semiconductor since the energy of the incident light has to be greater than the bandgap energy. Since TiO_2-anatase form presents a bandgap of 3.2 eV this constitutes a primary reason for the present low solar photoconversion efficiency; TiO_2 with its bandgap of 3.2 eV absorbs mainly UV light at wavelengths lower than 386 nm, which actually covers only about 5 % of the solar spectrum reaching Earth. Thus, the development of a photocatalyst with a bandgap lower than 3.2 eV is of great interest to red-shift light harvesting into de visible range. Photocatalytic activity of titanium dioxide in the visible light region is being improved by different techniques, such as: i) semiconductor sensitization; ii) doping and co-doping; or iii) using spatially structured titanium dioxide [37].

The second key process (ii) is the effective charge separation and transport of photogenerated electron and holes. They should travel through the nanoparticle to the surface reactive sites where the oxidation and reduction reactions will occur. However, simultaneously a recombination process may happen, through which active photogenerated charges are lost. Time resolved spectroscopic studies revealed that electron-hole trapping and recombination rates are extremely fast, lowering significantly the photocatalytic activity [38]. At this point, nanosize engineering plays a crucial role in controlling the recombination. Actually, this backward reaction occurs mainly in the boundaries and defects of the particles and thus reducing their size, the photogenerated charges have to travel a smaller distance until they reach the surface reaction sites, making recombination less probable. Important to mention that this approach may be not straightforward since the decreasing of the nanoparticles size may induce additional surface defects. Therefore, it is of utmost importance to develop synthesis routes where the quality of the particle and its size are balanced [39].

The third key process concerns the surface chemical reactions, for which engineering surface features (active surface sites) and size (surface area available) is very important. Co-catalysts may improve the catalytic activity by introducing active sites in the surface. An appropriate selection of a co-catalyst may also prevent the backward reaction. The use of highly porous materials of nanosized particles and nanostructures increases the surface area available to promote the forward reaction and the adsorption of reactants and indeed facilitate transfer of reactants to the active sites [30].

In summary, there are three main approaches to enhance the TiO_2 photocatalytic activity: i) bandgap tuning to visible light harvesting; ii) minimizing electron-hole recombination; and iii) promote the forward reaction at the surface of the particles and the adsorption of reactants.

There are already a number of commercial photocatalytic TiO_2 products available on the market. The most used commercial photocatalyst is P25, from Evonik (Germany), composed by anatase and rutile (ca. 75:25 wt.:wt.). This semiconductor is used as a standard reference in several photocatalytic research works [23, 36, 40-43].

1.2.2 Photocatalytic performance

Photo-oxidation of NO forms nitrite $\left(\mathrm{NO_2^-}\right)$, nitrate $\left(\mathrm{NO_3^-}\right)$ and nitrogen dioxide (NO_2). Since NO_2 is even more harmful than NO to human health, the desired reaction products are the ionic species. In this way, two parameters are used to characterize the photocatalyst performance: conversion of NO (equation 1.21) and selectivity for the formation of ionic species (equation 1.22).

$$X_{\mathrm{NO}} = \left(\frac{[\mathrm{NO}]_{\mathrm{in}} - [\mathrm{NO}]_{\mathrm{out}}}{[\mathrm{NO}]_{\mathrm{in}}} \right) \times 100 \tag{1.21}$$

$$S = \left(1 - \frac{[\mathrm{NO_2}]_{\mathrm{out}}}{[\mathrm{NO}]_{\mathrm{in}} - [\mathrm{NO}]_{\mathrm{out}}} \right) \times 100 \tag{1.22}$$

X_{NO} is the conversion of NO, S is the selectivity for the formation of ionic species, $[NO]$ and $[NO_2]$ stand for the concentration of NO and NO_2, respectively, and the superscripts (in and out) refer to the reactor's inlet and outlet streams.

1.2.3 Operating conditions effect

The photocatalytic activity of titanium dioxide semiconductor is strongly dependent on several operating and process conditions, namely: i) inlet concentration of the pollutant; ii) air humidity; iii) light intensity and light spectrum; iv) flow rate/residence time; v) photocatalyst amount per active area; vi) substrates [33, 44, 45].These aspects will be reviewed in the following sub-sections.

(i) Inlet concentration

The inlet concentration of NO has an important effect on photocatalytic activity. Numerous authors demonstrated that the highest values of degradation rate of pollutants are obtained for the lowest feed concentrations, independently of the substrates used [44, 46-52] – Figure 1.7 illustrates this effect for the case of NO.

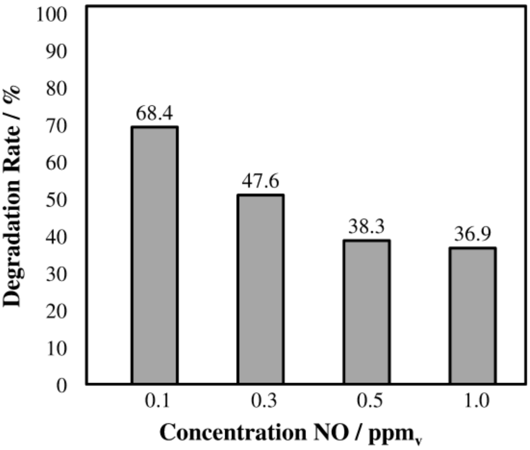

Figure 1.7. Effect of inlet NO concentration on NO_x degradation rate (adapted from [49]).

Assuming that the photocatalytic reaction is controlled by the adsorption of the pollutant, for an inlet concentration high enough, saturation of the adsorption sites on titanium dioxide surface occurs and the photocatalytic degradation rate levels out. Accordingly, Herrman *et al.* [53] and Hüsken *et al.* [49] observed that in the low range of inlet concentrations small changes on this parameter have a deeper effect in the photocatalytic conversion of the pollutants than in the high range of inlet concentrations.

(ii) Relative Humidity

The relative humidity (*RH*) effect on photocatalytic reaction was studied and reported by several authors. Water is essential for photocatalysis because it is responsible for the formation of $OH^{\bullet}$ and $O_2^{\bullet -}$ radicals, crucial species in the photoabatement; for this reason it is expectable that increasing the relative humidity the pollutant conversion increases [48, 50, 54]. Nevertheless, many authors have shown that the pollutant conversion increases with relative humidity only up to 40-50 % of *RH*, becoming the conversion constant afterwards - Figure 1.8 [46, 47, 51]; this effect was assigned to limitations on the UV light availability to form hydroxyl/superoxide radicals [51, 55] and to competition between water and pollutant for the adsorption sites on titanium dioxide. Maggos *et al.* [56] concluded that relative humidity effect on the conversion of pollutants is also influenced by their concentration: if pollutants concentration is at ppb level the competition for adsorption sites is much higher than if they are at ppm concentrations. This happens because for feed concentrations at ppb level it is needed only a small amount of water to produce enough hydroxyl/superoxide radicals.

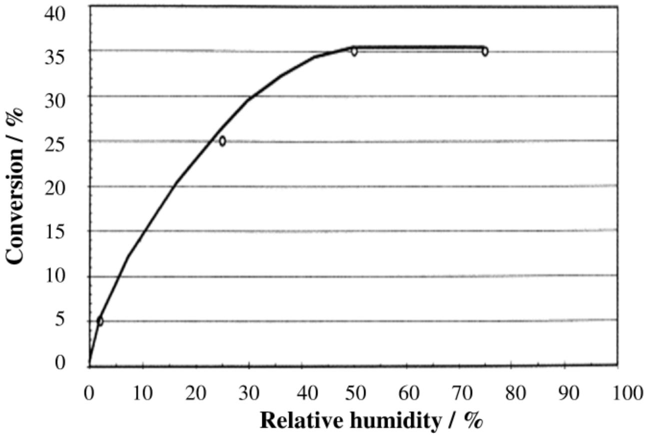

Figure 1.8. Effect of the relative humidity on the NO conversion[46].

(iii) Light intensity and light spectrum

In photocatalytic reactions the light source is responsible for providing enough energy to generate electron-hole pairs on the photocatalyst surface, leading to the photocatalytic oxidation of pollutants. Therefore, a high light intensity is able to produce a high amount of electron-hole pairs that will participate in the oxidation/reduction steps during the photocatalytic phenomenon and thus increasing the degradation of pollutants [44, 46, 49, 50, 57]. The electron generation term is described by the Beer-Lambert law, which relates the absorption of light to the properties of the material through which light is travelling: $G_{e^-} = \eta_{inj}\alpha\left(\lambda\right)I_0 e^{-\alpha(\lambda)x}$. η_{inj} is the injection efficiency, $\alpha(\lambda)$ is the wavelength-dependent absorption coefficient of the material and I_0 is the incident photon flux. Considering a material being irradiated with energy higher than its bandgap, electrons will be excited from the valence band to the conduction band. This absorption process is wavelength-dependent and is described by the absorption coefficient α of the material, which increases with the decrease of the wavelength of light incident on it.

Several studies were developed to better understand the light intensity effect on the photocatalytic phenomenon for different inlet concentrations. Yu and Brouwers [50] observed a logarithmic relation between light intensity and NO_x ($NO + NO_2$) conversion for low values of inlet concentration (0.5 and 1.0 ppm), in the range of light intensities of 0.1 up to 1.3 $mW\cdot cm^{-2}$ - Figure 1.9. Devahasdin *et al.* [46] performed the same type of studies but for higher inlet concentrations of NO – 5 and 40 ppm – under close light intensities, from 0.2 to 0.8 $mW\cdot cm^{-2}$. Contrary to what was observed by Yu and Brouwers, for low inlet concentrations (*ca.* 5 ppm), the degradation rate does not depend on light intensity, whereas for values of inlet concentration of ca. 40 ppm an increase of 20 % in the degradation rate was observed - Figure 1.10. It is important to mention that these discrepancies may be due to the use of different systems and thus different photocatalytic behaviors are observed. Moreover, reactors were also different: in the study by Yu and Brouwers a wall paper was used while in the study by Devahasdin *et al.* a cylindrical photocatalytic reactor was considered. The role of light intensity on the degradation rate is still scarcely understood and should be further studied.

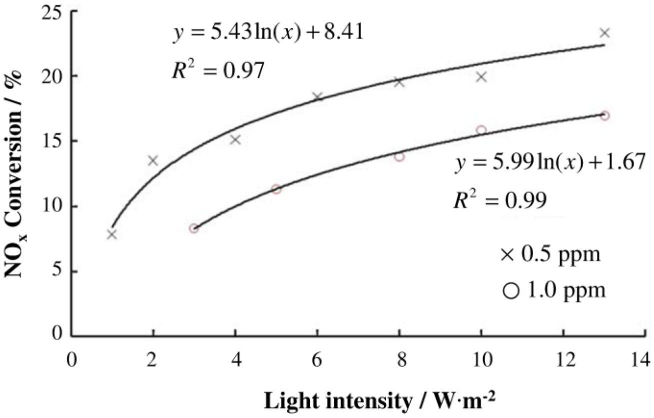

Figure 1.9. Effect of light intensity on the NO_x ($NO + NO_2$) conversion[50].

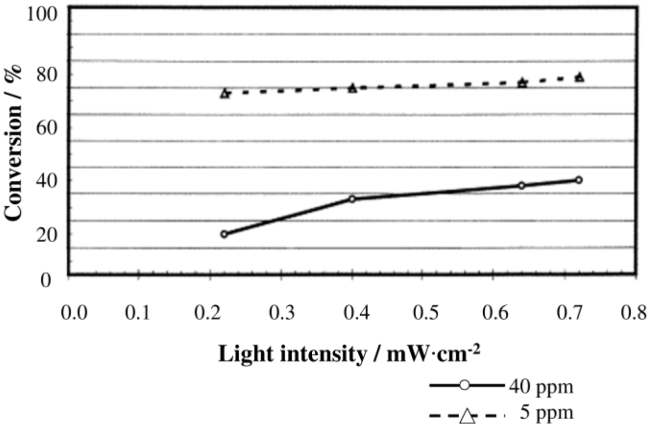

Figure 1.10. Effect of light intensity on the NO conversion[46].

(iv) Flow rate/residence time

Another parameter that influences the photocatalytic activity is the flow rate of polluted air, which is directly related to the residence time on the photoreactor. If, during the photocatalytic reaction, high flow rates are considered, the polluted air will have small residence times meaning short contact times with the photocatalyst; those short contact times yield smaller pollutant conversions. Most works that studied the flow rate effect have reported flow rates between 1.0 and 5.0 L min^{-1} - Figure 1.11 [47, 49-52, 57]. Devahasin *et al.* [46] and Wang *et al.* [48] describe an increase of the photocatalytic conversion with the residence time but only up to 12-15 s; above that value the degradation rate of the pollutant becomes constant. This happens because the reaction equilibrium is reached [46, 48].

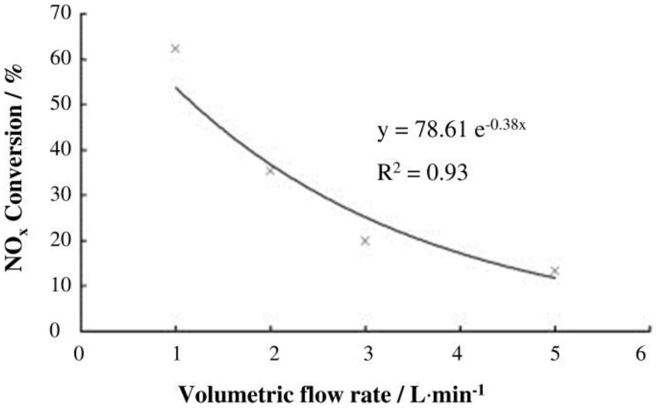

Figure 1.11. Effect of the volumetric feed flow rate on the NO_x conversion [50].

(v) Photocatalyst amount per active area

The amount of photocatalyst present in the substrate used for photocatalytic processes influences the pollutant degradation rate [49, 50, 52, 53, 58]. As expected, the pollutant degradation increases with the TiO_2 amount [49, 50] up to a certain level, which is reached when the upper TiO_2 layers hide the light to reach the lower layers – Figure 1.12 [52, 53, 58] – optical thickness. The degradation rate increase is related to the larger illuminated catalyst surface area available to promote the reaction.

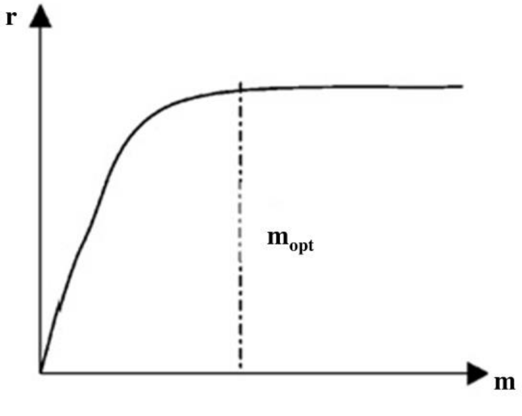

Figure 1.12. Influence of the mass of catalyst (m) on reaction rate, *r*[53].

(vi) Substrate

The photocatalytic activity is greatly influenced by the type of substrate and by the technique used for depositing the photocatalytic material. These two elements should be carefully combined in order to maximize the photocatalytic activity and its long-term stability. Literature describes different substrates such as optical fibre, fibreglass, quartz, borosilicate glass and stainless steel. The substrate shape also can affect performance, depending on if they are cylinders, tubes, sheets or plate, beads, etc.

Several studies comparing different substrates have been performed. For instance, photocatalytic degradation of NO by immobilized-TiO_2 on an activated carbon filter compared with TiO_2 immobilized on a glass fiber filter seems to be higher and consequently the generation of NO_2 is smaller [59]. This situation may be explained by the improved adsorption capacity of the activated carbon. Other comparisons were also performed. A porous building material as mortar was compared with a non-adsorptive substrate as glass [52]. A decrease on conversion of NO_x over time for the TiO_2-immobilized on glass was observed, while NO_x oxidation on a mortar substrate remained constant [52]. This behavior was justified by the adsorption of nitrate ions produced from NO_2 oxidation on the surface of substrates, occupying the active sites and thus leading to deactivation. For mortars, ions are also formed but this deactivation does not happen or it is retarded due to the large adsorption capacity of the substrate [52].

1.2.4 Langmuir-Hinshelwood model

As mentioned before, photocatalysis is a surface phenomenon that originates hydroxyl radicals $\left(OH^{\bullet}\right)$ and superoxide anions $\left(O_2^{\bullet -}\right)$, which are the oxidation mediators of the organic contaminants. According to Yu *et al.* [60], the mechanism of photocatalytic degradation of NO_x can be divided in three stages: i) adsorption of gas reactants in the photocatalyst surface (equation 1.23 to 1.25); ii) generation/recombination of electron-hole pairs (equation 1.26 and 1.27); and iii) oxidation of NO and water reduction (equations 1.28 to 1.32).

$$TiO_2 + H_2O \xrightleftharpoons{K_{H_2O}} H_2O_{ads} \qquad 1.23$$

$$TiO_2 + O_2 \xrightleftharpoons{K_{O2}} O_{2\,ads} \qquad 1.24$$

$$TiO_2 + NO \xrightleftharpoons{K_{NO}} NO_{ads} \qquad 1.25$$

$$TiO_2 + h\nu \longrightarrow e^- + h^+ \qquad 1.26$$

$$e^- + h^+ \longrightarrow \mathit{heat} \qquad 1.27$$

$$h^+ + H_2O_{ads} \longrightarrow OH^{\bullet}_{ads} + H^+ \qquad 1.28$$

$$e^- + O_{2\,ads} \longrightarrow O_2^{\bullet -} \qquad 1.29$$

$$NO_{ads} + OH^{\bullet}_{ads} \xrightarrow{k_{NO}} HNO_{2\,ads} \qquad 1.30$$

$$HNO_{2\,ads} + OH^{\bullet}_{ads} \xrightarrow{k_{HNO2}} NO_{2\,ads} + H_2O \qquad 1.31$$

$$NO_{2\,ads} + OH^{\bullet}_{ads} \xrightarrow{k_{NO2}} NO^{-}_{3\,ads} + H^+ \qquad 1.32$$

When TiO_2 is irradiated by sunlight it absorbs photons with energy ($h\nu$) higher than the bandgap of the semiconductor, generating free electrons $\left(e^-\right)$ in the conduction band and free holes $\left(h^+\right)$ in the valence band - equation 1.26. Then, electrons and holes can react accordingly to equations 1.28 and 1.29, originating hydroxyl radicals $\left(OH^{\bullet}\right)$ and superoxide anions $\left(O_2^{\bullet -}\right)$. However, at the photocatalyst surface, free electrons and free holes instead of generating radicals can recombine (surface recombination) as shown in equation 1.27, which strongly limits the photocatalytic activity [61, 62]. Additionally, another back reaction process can occur: generated hydroxyl radicals and superoxide anions can be consumed by inactive species [63].

The photocatalytic degradation of NO should result in the production of HNO_3; though, two other intermediate products can also be generated in this process: HNO_2 and NO_2. HNO_2 is totally consumed as reaction (31) is very fast; on the other hand, not all NO_2 is converted into HNO_3 and ends desorbing – equation 1.33.

$$TiO_2 + NO_2 \xrightleftharpoons{K_{NO2}} NO_{2\,ads} \qquad 1.33$$

Finally, to describe the photocatalytic phenomenon reactants adsorption on the active sites of TiO_2 has to be also analyzed. The adsorption equilibrium is reached when NO adsorption $\left(r_{\text{ads}}\right)$ and desorption $\left(r_{\text{des}}\right)$ rates are equal – equation 1.34 [50, 60].

$$r_{\text{ads}} - r_{\text{des}} = k_{\text{ads}} C_{\text{TiO}_2\text{free}} C_i - k_{des} C_{\text{i ads}} = 0 \qquad 1.34$$

where *i* is the species NO, NO_2 or H_2O; k_{ads} and k_{des} are the adsorption and desorption kinetic constants, respectively; and $C_{\text{TiO}_2\text{free}}$ is the concentration of free active sites on TiO_2 surface. Therefore, manipulating equation 1.34, the concentration of adsorbed species comes as described in equations 1.35 and 1.36.

$$C_{\text{i ads}} = K_i C_{\text{TiO}_2\text{free}} C_i \qquad 1.35$$

$$K_i = \frac{k_{\text{ads}}}{k_{des}} \qquad 1.36$$

The total concentration of active sites in the titanium dioxide surface is given by the sum of the concentration of free active sites and the concentration of occupied sites by NO, NO_2 and H_2O species – equation 1.37.

$$C_{\text{TiO}_2} = C_{\text{TiO}_2\text{free}} + C_{\text{NO ads}} + C_{\text{NO}_2\text{ ads}} + C_{\text{H}_2\text{O ads}} \qquad 1.37$$

Substituting equation 1.35, applied to the different adsorbed species, into equation 1.37, the concentration of total active sites in TiO_2 becomes:

$$C_{\text{TiO}_2} = C_{\text{TiO}_2\text{free}} + K_{\text{NO}} C_{\text{TiO}_2\text{free}} C_{\text{NO}} + K_{\text{NO}_2} C_{\text{TiO}_2\text{free}} C_{\text{NO}_2} + K_{\text{H}_2\text{O}} C_{\text{TiO}_2\text{free}} C_{\text{H}_2\text{O}} \qquad 1.38$$

Solving to $C_{\text{TiO}_2\text{free}}$ as follows:

$$C_{\text{TiO}_2\text{free}} = \frac{C_{\text{TiO}_2}}{1 + K_{\text{NO}} C_{\text{NO}} + K_{\text{NO}_2} C_{\text{NO}_2} + K_{\text{H}_2\text{O}} C_{\text{H}_2\text{O}}} \qquad 1.39$$

Finally, the concentration of each adsorbed species can be obtained combining equation 1.35, applied to the different adsorbed species, and equation 1.39:

$$C_{\mathrm{NO\ ads}} = \frac{K_{\mathrm{NO}} C_{\mathrm{TiO_2}} C_{\mathrm{NO}}}{1 + K_{\mathrm{NO}} C_{\mathrm{NO}} + K_{\mathrm{NO_2}} C_{\mathrm{NO_2}} + K_{\mathrm{H_2O}} C_{\mathrm{H_2O}}} \quad 1.40$$

$$C_{\mathrm{NO_2\ ads}} = \frac{K_{\mathrm{NO_2}} C_{\mathrm{TiO_2}} C_{\mathrm{NO_2}}}{1 + K_{\mathrm{NO}} C_{\mathrm{NO}} + K_{\mathrm{NO_2}} C_{\mathrm{NO_2}} + K_{\mathrm{H_2O}} C_{\mathrm{H_2O}}} \quad 1.41$$

$$C_{\mathrm{H_2O\ ads}} = \frac{K_{\mathrm{H_2O}} C_{\mathrm{TiO_2}} C_{\mathrm{H_2O}}}{1 + K_{\mathrm{NO}} C_{\mathrm{NO}} + K_{\mathrm{NO_2}} C_{\mathrm{NO_2}} + K_{\mathrm{H_2O}} C_{\mathrm{H_2O}}} \quad 1.42$$

The photocatalytic process is governed by the kinetics of the different reactions occurring during it usually described by a Langmuir–Hinshelwood (L-H) model, which allows formulating the photocatalytic oxidation rate equation. Thus, considering a generic reaction of the type A + B → C + D (assumed irreversible), the reaction rate r is given by equation 1.43 [53].

$$r = k\theta_{\mathrm{A}}\theta_{\mathrm{B}} \quad 1.43$$

θ_{A} and θ_{B} are given by equations 1.44 and 1.45, respectively:

$$\theta_{\mathrm{A}} = \frac{K_{\mathrm{A}} X_{\mathrm{A}}}{1 + K_{\mathrm{A}} X_{\mathrm{A}}} \quad 1.44$$

$$\theta_{B} = \frac{K_{B} X_{B}}{1 + K_{B} X_{B}} \quad 1.45$$

where K_{A} and K_{B} are the adsorption equilibrium constants in the dark, X_{A} and X_{B} are the concentrations in the liquid phase or partial pressures in the gas phase and k is the reaction rate constant. According to Arrhenius' law, k depends only on temperature - equation 1.46;

$$k = k_0 \exp\left(-\frac{E_a}{RT}\right) \quad 1.46$$

where E_{a} is the activation energy, T the absolute temperature and R is the universal gas constant.

In the same way, equilibrium constants K_A and K_B depend on the temperature according to the van't Hoff's law (Equation 1.47), where ΔH_i is the enthalpy of the reaction:

$$K_i = \left(K_i\right)_0 \exp\left(-\frac{\Delta H_i}{RT}\right) \qquad 1.47$$

Applying now the L-H model as described above to the photo-oxidation of NO, the corresponding reaction rate can be written. For that, it is important to consider the reactional mechanism at steady state proposed by Devahasdin and illustrated in Figure 1.13; HNO_3 and NO_2 species are in equilibrium on the catalyst surface [46].

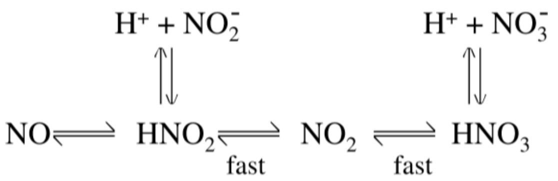

Figure 1.13. Reaction scheme for the photocatalytic oxidation of nitric oxide on TiO_2.

This mechanism considers that the reaction that produces HNO_3 occurs very fast; when the catalyst becomes saturated with HNO_3 the reaction stops at NO_2 production, which starts desorbing according to equation 1.33. Indeed, the reaction rate of NO degradation becomes as described by equation 1.48.

$$-r_{\mathrm{NO}} = \frac{k'_{\mathrm{A}} C_{\mathrm{NO}} C_{\mathrm{H_2O}} - k'_{B} C_{\mathrm{NO_2}}}{\left(1 + K'_{\mathrm{NO}} C_{\mathrm{NO}} + K'_{\mathrm{NO_2}} C_{\mathrm{NO_2}} + K'_{\mathrm{H_2O}} C_{\mathrm{H_2O}}\right)^2} \qquad 1.48$$

$-r_{\mathrm{NO}}$ is the reaction rate of NO, k'_{A} and k'_{B} are the reaction rate constants, $K'_{\mathrm{H_2O}}, K'_{\mathrm{NO}}, K'_{\mathrm{NO_2}}$ are the adsorption equilibrium constants of water, nitrogen oxide and nitrogen dioxide, respectively, $C_{\mathrm{H_2O}}, C_{\mathrm{NO}}, C_{\mathrm{NO_2}}$ are concentrations of water, nitrogen oxide and nitrogen dioxide in the gas phase.

This Langmuir-Hinshelwood approach has been used by several authors to describe the photocatalytic oxidation of nitrogen oxides in different semiconductor materials. For instance, Wang *et al.* [48] modeled the photocatalytic behavior of TiO_2 loaded on a woven glass fabric and Folli *et al.* [64] used TiO_2 coated on glass beads. In both studies the L-H model was applied and similar results were obtained for the kinetic constant *k* and for the adsorption equilibrium constant in the dark *K* [48, 64]. However, other authors report more complex studies where the L-H model takes also into account the influence of other experimental conditions such as: volumetric flow rate, irradiance, relative humidity, amount of photocatalyst and reactor size [60, 65]. For all these different cases, the Langmuir-Hinshelwood model was applied to describe the photocatalytic reaction rate of nitrogen oxide and a good agreement was achieved between experimental data and the modeling results [46, 48, 60, 64, 65].

1.2.5 Photocatalytic reactors

Several photocatalytic reactors can be used for studying air treatment, so it is important to choose the right configuration of the reactor to improve the photocatalytic efficiency, allowing comparable and repeatable measurements. Even if the experimental setup includes other elements such as the light source, NO_x analyzer or the gas supplier, the core of the test setup is the photo-reactor, which is responsible for an effective contact among photocatalyst, pollutants, water and light [32, 66, 67].

Reactors are usually categorized by their mode of operation or by their geometry that determines the reactor design; still they can be also categorized by the light source used or by the way the photocatalyst is introduced in the reactor [66, 67]. According to the mode of operation, the photoreactors can be classified as batch reactors or continuous flow reactors. Batch reactors are very interesting for lab-scale applications since they are usually used for determining the reaction kinetics and for characterizing newly developed photocatalysts [66, 68]. On other hand, continuous flow reactors are usually used in applications with a continuous source of pollutants. Moreover, they are especially useful for industrial applications that handle with process gases, thus reducing harmful gases emissions into the atmosphere. This type of reactors is also used at laboratory scale, where the inlet concentration of pollutants is known and the output concentration is continuously measured to calculate the pollutant removal efficiency [52, 69-72].

Reactors can be tubular, annular or flat plate. Tubular reactors are quite common since they are easy to assemble and to handle. They can be composed of one – single tubular reactor - or more glass tubes – multitubular reactor - where the photocatalyst is applied under several forms, e.g. a coated film, fluidized particles, free powder on a support, etc. The single or multiple tubes are then placed in the glass reactor vessel and the light sources are located externally to the tubes and parallel to them; the gas flow is fed along the axis of the tubes. Several authors used tubular reactors mainly to study the photocatalytic oxidation of organic compounds targeting air purification [73-75].

Typical annular reactors have two concentric tubes and pollutant stream flows between them; the light source is placed inside of the inner tube - Figure 1.14. This configuration ensures that the active material absorbs all emitted photons. Several studies have been reporting photocatalytic degradation of NO_x using annular flow reactors [76-78]. Removal efficiencies of NO_x pollutants higher than 90 % under UV light were reported [76, 78]. On the other hand, Lim *et al.* [77] compared the typical annular photoreactor with a modified two-dimensional fluidized-bed photo-reactor and concluded that the NO removal is higher in this type of reactor.

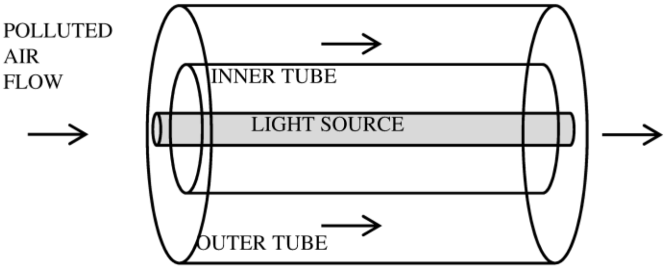

Figure 1.14. Annular flow reactor

Flat plate reactors accommodate the photocatalyst support, also flat and usually made of glass or metal, and the polluted stream flows parallel and on the top of the photocatalyst support - Figure 1.15. The light source can be placed inside the reactor chamber or otherwise can be located outside the reactor that then has to have a glass window. TiO_2 immobilized on materials such as paints or mortars is usually characterized on flat plate reactors [50, 69, 79-81].

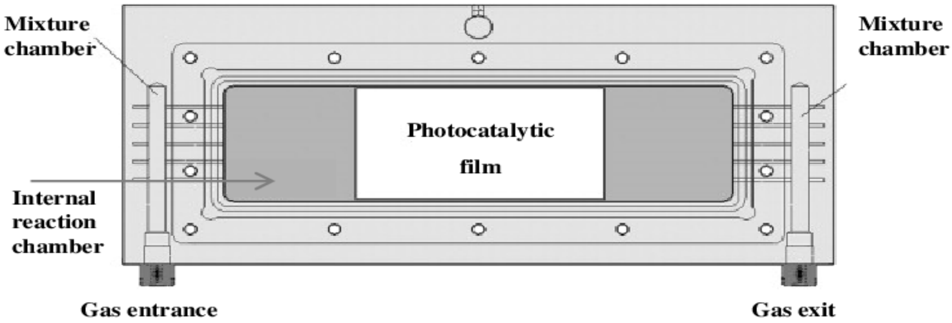

Figure 1.15. Schematic representation of the flat plate reactor, in this case, authors used a UV lamp external to the reactor and parallel to sample (top view) [36].

1.2.6 Immobilization of TiO_2

As discussed above titanium dioxide exhibits several advantages as a photocatalyst for environmental applications. Usually this material is used in suspension and mainly for water treatment; however, several technical difficulties arise for TiO_2 removal, as it brings additional costs to the process. Thus, this material can be immobilized in specific supports, eliminating the removal extra step that brings complexity to the final photocatalysis process. This is especially important in water and wastewater treatment. Nevertheless, the photocatalytic activity strongly depends on the type of immobilization and on the supports used, and so this will be discussed hereafter [82-85]. TiO_2 semiconductor is a nanoparticulated powder that may cause some risks to the human health when inhaled. Consequently, the immobilization process may also contribute to diminish this risk [86]. The choice of the right support and methods to immobilize the titanium dioxide have some specific requirements, as follows:

a) the photocatalytic activity should not be inhibited during the immobilization process;

b) there must be good adhesion of the particles to the support;

c) the support has to be chemically inert;

d) the support should have a large specific surface area (this is an important factor because the photocatalytic reaction is a surface reaction);

e) the support should be compatible with the environmental use.

Materials that satisfy all the above requirements are difficult to obtain. Up to now, several approaches have been proposed for immobilization on various supports, *e.g.* sol-gel, dip coating, physical and chemical vapor deposition, electrophoretic methods, among others.

(i) Dip coating technique

Dip coating is a process to create thin films; the substrates are immersed in the solution of the coating material and a layer is formed on the substrate. Then, this substrate is removed from the solution and the solvent is allowed to evaporate – Figure 1.16. Fernández *et al.* [87] applied this technique on two supports, glass and quartz, which were immersed in a solution of titanium tetra-isopropoxide up to three times to increase the films thickness. At the end, samples were calcined to eliminate solvent and impurities. These supports were characterized by several techniques and their photocatalytic ability tested and compared. The photocatalytic activity was analyzed based on the degradation of malic acid. For this reaction, quartz was the better support because it showed higher photocatalytic activity comparatively with glass: the degradation of malic acid occurred in 1 hour in the quartz support and in case of glass this reaction took 3 hours, under the employed conditions. These two supports were chosen by their characteristics; they are chemically and photocatalytically inert. The differences observed in the photocatalytic activity were associated to the interaction between titanium dioxide particles and the support during the immobilization process. The dip-coating process needs a step of heat treatment to ensure good adhesion of the material to the support. The heat treatment was made at a temperature close to the melting point of the glass, which induces the ions diffusion from glass to the titanium dioxide layer. This ions transfer was verified by XPS analysis and sodium was identified on the titanium dioxide surface. The transition of ions to the deposited layer led to electron-hole recombination that conducted to photocatalytic activity inhibition. Quartz showed stability under heating, proved by XPS analysis. Therefore, this support presents a higher degree of purity leading to better results of photocatalytic activity. Thereby, these authors used this support to immobilize titanium dioxide and assess the photocatalytic activity of these films on another study [88].

More recently, Kwon *et al.*[89] investigated the deposition of TiO_2 and TiO_2-SiO_2 on glass by dip coating. Similarly to Fernández *et al.*[87], a high temperature step was also considered to promote a good adhesion of titania to the support. However, these authors also added silica to titanium dioxide to improve this adhesion; they observed that a molar ratio of 1:1 presented the best compromise between adhesion and photocatalytic activity. The photocatalytic activity of these materials was measured based on the degradation of methylene blue.

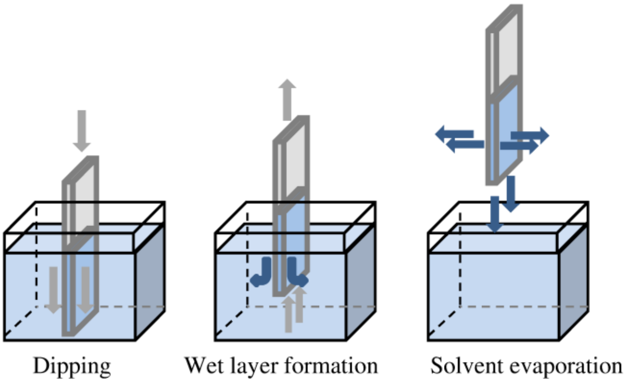

Figure 1.16. Schematic diagram of the dip coating process.

(ii) Sol-gel technique

Sol-gel is a method that involves a colloidal suspension, sol, that after gelation and by means of precursors allows the formation of a gel [90]. Different precursors can be used, *e.g.* titanium alkoxide, titanium tetrachloride or titanium halogenide. The sol-gel method - Figure 1.17 - includes as a final step spread coating or dip coating but the latter offers the possibility to coat both surfaces of the substrate. This method has some important advantages as it is a low temperature process and allows to coat large areas with high homogeneity at a low cost [91, 92]. Lim *et al.* [90] studied sol-gel with dip-coating over fiberglass, woven fiberglass, aluminum plate and glass slide. The efficiency of titanium dioxide immobilization to the support and the photocatalytic activity were evaluated for all supports; the photoactivity was assessed based on the degradation of methylene blue. Woven fiberglass and fiberglass showed the best results in terms of immobilization, while glass slide showed the lowest photocatalytic activity. As a support material, fiberglass has the advantage of providing a larger surface area;

on the other hand, glass slides present a flat surface and so the adhesion of titanium dioxide to the support did not present the expected results. The aluminum plate was not a good substrate because it has also a flat surface and exhibits a high thermal expansion that leads to cracking problems on deposition.

Páez and Matousek [93] also studied the deposition of TiO_2 layers on a glass support by sol-gel with dip coating technique. Contrary to what was stated before, these authors reported a good adhesion to a soda-lime glass of the titania layer. This good adhesion may be related to the use of different precursors for the preparation of titanium dioxide and to the thermal treatments performed between layers deposition. Chen and Dionysiou [94] reported a study of titanium dioxide deposition on stainless steel by sol-gel technique and the adhesion of this titanium dioxide layer to the support was assessed. These authors incorporated different amounts of titanium dioxide (P25, Evonik) to prepare the sol-gel and concluded that to have a good adhesion of titania to the stainless steel this amount has to be less than 50 g·L^{-1}.

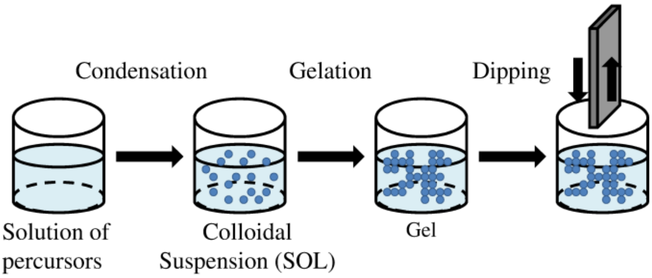

Figure 1.17. Schematic diagram of sol-gel method associated to dip-coating.

(iii) CVD technique

Another technique used to immobilize titanium dioxide is the chemical vapor deposition (CVD). CVD uses a reactor, a source of gas and a precursor – Figure 1.18. For TiO_2 deposition, organic, inorganic or mixed precursors can be used, such as titanium tetra-isopropoxide, titanium tetrachloride or titanium tetra-isopropoxide with titanium tetrachloride, respectively [95, 96]. Ding *et al.* [96] described TiO_2 immobilization by CVD on porous solids, e.g. carbon, γ-alumina and silica gel as supports, and titanium tetra-isopropoxide as precursor. Deposition of TiO_2 on silica gel produced the best immobilized system, demonstrated by the highest level of photocatalytic degradation of phenol in water. The authors justified this observation since silica gel has more surface hydroxyl groups and higher macropore surface area. In fact, high surface area is crucial to get high photocatalytic activity. Another important characteristic is the anatase particles size that should be small; this allows to a better distribution of titanium dioxide on supports with more active sites for the photocatalytic reaction.

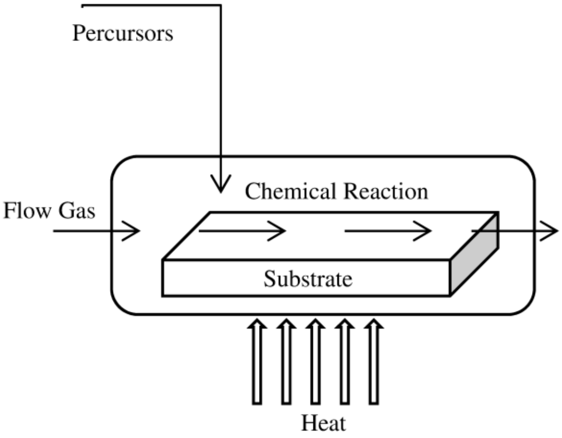

Figure 1.18. Schematic diagram of chemical vapor deposition method (adapted from [53]).

Mills *et al.* [97] compared a thin film of TiO_2 deposited by CVD technique on a glass support with another thin film of P25 particles immobilized by spin-coating. These authors concluded that both types of films have photocatalytic activity, but P25 film presents a better performance. However, the film obtained by CVD presents optical clarity and produces a more robust film. These two advantages can make viable the commercialization of films prepared by CVD. This technique can also be used to deposit titanium dioxide on other substrates as window glasses; TiO_2-coated windows are self-cleaning and fog proof [95].

(iv) PVD technique

Physical vapor deposition (PVD) technique, also known as sputtering, allows to form thin films wherein atoms or molecules are ejected from a target material to the substrate – Figure 1.19 [98-100]. Among the techniques for coating thin films onto supports, PVD is one of the most versatile and environmental-friendly. In particular, a magnetron sputtering system consists of a vacuum chamber containing a target of the material to be deposited and a substrate. This method allows precise control of film thickness, grain size and layer composition and microstructure. Wenjie Zhang *et al.* [99] used PVD to deposit TiO_2 thin films on microscope glass and fused quartz slides, using a precursor of titania with a very high purity (99.9 %). The decomposition of aqueous methyl orange was determined in this work to evaluate the photocatalytic activity of the films produced; the authors concluded that the photocatalytic activity increases with thickness from 300 to 900 nm. However, the increase of thicknesses above a certain limit did not have any significant effect on the photocatalytic activity; this saturation occurs because films exhibit more opacity, so it is more difficult to pass the light.

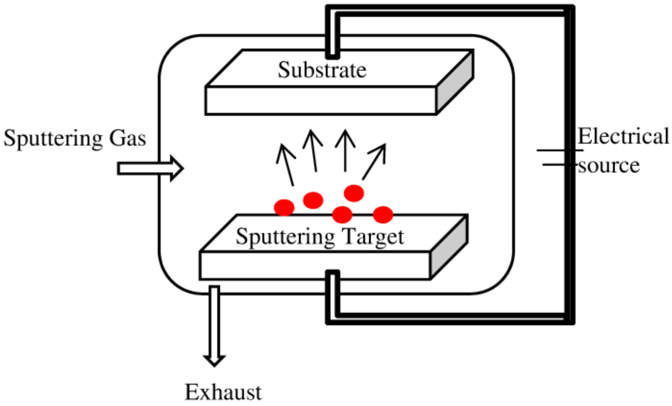

Figure 1.19. Schematic diagram of physical vapor deposition.

Zhang *et al.* [100] also studied the PVD deposition of titanium dioxide on glass substrates. They studied the influence of the vacuum pressure of PVD chamber on the titania film photocatalytic activity towards methyl orange degradation. In this study, these authors concluded that deposition of titania at high pressure (1.4 Pa) exhibits higher photocatalytic activity. The film obtained at this higher pressure allowed to completely degrade the methyl orange after 5 hours of UV irradiation [99, 100].

(v) Electrophoretic technique

Electrophoretic technique is used for deposition of particles on metallic substrates. Powder material is dispersed in a solvent where two electrodes are immersed, the metallic substrate and the counter-electrode, both arranged in parallel. Then, an electric potential is applied to the system and particles move towards the metallic substrate to make the film – Figure 1.20.

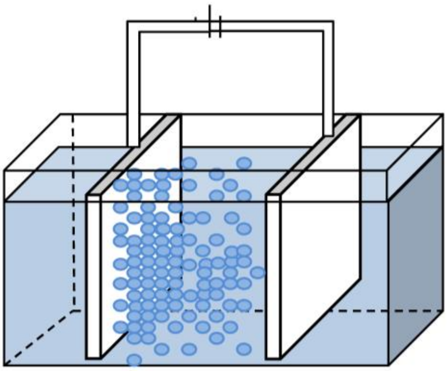

Figure 1.20. Schematic diagram of electrophoretic deposition.

Fernández *et al.* [87] used electrophoretic technique to deposit titania on stainless steel and they compared the corresponding photocatalytic activity with other films prepared by dip-coating and supported on glass and quartz. These authors concluded that the films deposited on stainless steel and glass showed lower photocatalytic activity and adhesion problems when compared to films deposited on quartz. In the deposition process the adhesion was prompted by heating the samples, and some cations migrated from the support to the photocatalytic layer. The presence of these cations in the lattice of titania enable the electron-hole recombination which inhibits the photocatalytic activity of the titania. Byrne *et al.* [101] studied the deposition of titanium dioxide on stainless steel substrates, on titanium alloys substrates, on tin oxide coated glass substrates and on titanium metal substrates and the corresponding photocatalytic activity was evaluated by degradation of phenol. Among all supports, stainless steel and titanium alloys seem to present the best performance on phenol degradation. It was expected tin oxide coated glass to show good rate of degradation because it has the advantage of being satisfactorily transparent to UV-A light giving thus the possibility of irradiation above and below the coated surface. However, glass supports are breakable and expensive. The use of cheaper materials as stainless steel is envisaged in order to turn TiO_2 immobilization a cost-effective process; actually electrophoretic technique allows to deposit titanium dioxide on cheapest supports unlike other techniques as for instance sol-gel.

A support with a large surface area is one of the main requirements mentioned above for an efficient immobilization process. Besides glass, quartz and stainless steel, other types of supports should be used to enhance this property. Therefore, Rachel *et al.* [98] analyzed the viability of using brick, cement and ceramic tiles as substrates by PVD. However, the photocatalytic activity exhibited by immobilizing TiO_2 on these substrates was very low. The immobilization of titanium dioxide on pumice stone by dip coating technique was also investigated by Rachel *et al.* [102]. Pumice stone was immersed in a sonicated slurry of TiO_2 to impregnate this semiconductor on the substrate and it was observed that calcination steps between layers deposition allow to obtain an improved deposition [87, 98].

In what NO_x photoabatement is concerned, Kaneko and Okura [82] described three supports with a porous structure to provide a large surface area for TiO_2 immobilization: i) PTFE-based sheets (fluorocarbon polymer); ii) hardened cement past; and iii) an alkoxysilane-based paint. The titanium dioxide was added to the supports by mechanical mixture. PTFE sheets exhibited the best results on degradation of NO (concentration between 0.05 and 10 ppm) from air, however, paint films and cement plates also demonstrated ability to efficiently abate this pollutant.

Paint coatings, in opposition to the previous deposition methods, allow creating a 3D layer where TiO_2 nanoparticles are available for photocatalysis up to the optic thickness, which is around 100 µm (wet thickness). A photocatalytic paint coat has a very large interfacial illuminated area available for photocatalysis, originating then very photoactive surfaces. Magos *et al.*[56] studied two commercial paints containing TiO_2 to degrade NO and NO_2. In this study, mineral silicate paint and a water-based styrene acrylic paint were used, allowing to obtain very efficient TiO_2-immobilized photocatalysts: in the case of the silicate paint it was observed a photodegradation of 74 % for NO and 27 % for NO_2; for the acrylic paint, these values are significantly higher, 91 % for NO and 71 % for NO_2, under the tested conditions. Águia *et al.*[36] studied the immobilization of different commercial titanium dioxide samples on a water-based vinyl paint. Photocatalytic titanium dioxide from different manufactures were tested, *e.g.* from Kemira, Millenium, Evonik, Sachtleben, Kronos and Tayca. It was measured the conversion of NO for all the paints. TiO_2 from Millenium, Sachtleben and Tayca showed the highest values of conversion, about 40-50 %. On the other hand, TiO_2 from Kemira showed the lowest level of conversion, about 15 %.

1.2.7 Applications of TiO_2 photocatalyst

As described before, when the photocatalyst is irradiated in presence of water hydroxyl radicals are formed and the photocatalytic degradation occurs. Actually, in recent years interest has been focused on the use of semiconductor materials as photocatalysts for the removal of organic and inorganic species from aqueous phase. This approach has been suggested for environmental protection due to TiO_2 ability to oxidize organic and inorganic substrates, leading in some cases to the total mineralization of these water pollutants. Photodegradation in water presents lower efficiency than photodegradation in air because it faces some limitations such as: a) in water the pollutant concentration is higher; b) pollutants have less contact with the photocatalyst; c) when used dispersed, recovery of the semiconductor from water causes engineering difficulties in automatic operation [27, 82, 83, 103].

For photoabatement of atmospheric pollutants, like in air purification and deodorizing, TiO_2 is used to treat air outdoor (under sunlight illumination) and air streams in reactors illuminated with UV lamps. The former approach is used for odors elimination, such as cigarette smoke and for degradation of air pollutants, such as nitrogen oxides [45, 82, 83, 103].

Several commercial photocatalytic products are being developed and tested. These products are essentially for self-cleaning, antibacterial, antifogging, air purification and water mineralization [45]. Examples are hereafter described. Masakazu [104] reported some applications of TiO_2 photocatalyst in green chemistry. Table 1.2 presents commercial products, made available recently, and the corresponding producers.

In 2007 was estimated that in Japan more than 50 000 m^2 of different surfaces, *e.g.* houses, monuments, buildings, roads, etc., have been coated with photocatalytic titanium dioxide [105]. Kaneko and Okura [82] described a case study of a highway in Tokyo with photocatalytic panels to reduce the level of pollutants in that area. The photocatalytic panels are made of a polyvinyl chloride resin and placed alongside a six-lane highway. These panels had a Pyrex® glass window that allows solar UV light to pass and polluted air was pumped between the panel and glass. Nitrogen oxides in air were in consequence oxidized to nitrates. The panels showed a fraction of pollutants removal between 31-69 % of NO_x; 67-79 % of SO_2 and 17-20 % of nonmethane hydrocarbons (NMHC).

Table 1.2. Some producers of photocatalytic materials.

Product	Companies
Air cleaner containing TiO_2 photocatalysts	Sharp Co. Ltd; Daikin Ind. Ltd; Toyota Home Ltd
White paper containing TiO_2 photocatalysts	Mitsubishi Paper Mills, Inc.
Antibacterial textile fibers containing TiO_2 photocatalysts	Kurare, Inc.
Systems for the purification of polluted air, e.g., the elimination of NO_x	Furukawa Kikai-Kinzoku Ind., Inc.
Super-hydrophilic, self-cleaning systems, and coating materials for cars	Toto, Inc.
Soundproof walls using TiO_2 photocatalysts	Furukawa Kikai-Kinzoku Ind., Inc.
Photocatalyst coated lamps (or lamp covers)	Toshiba Light. & Tech., Inc.
Cement containing TiO_2 photocatalysts	Taiheiyou Cement, Inc.
Self-cleaning tent	Taiyo Ind., Inc.

Photocatalytic titanium dioxide products used on outdoor surfaces to air treatment are usually also used for self-cleaning purposes. The self-cleaning effect concerns preventing the accumulation of dirt in the surfaces, keeping surfaces cleaned. However, the products can only be optimized for one of these applications, since the best material for one application may not be the best material for the other. Therefore, *TOTO Inc.* in Japan is producing another interesting photocatalytic product, the TiO_2-based self-cleaning tiles (Figure 1.21), already applied on several buildings in Japan. Buildings covered with the common type of tiles have to be cleaned every 5 years, while with the new technology it is predicted that the tiles could stay clean for more than 20 years. Besides the self-cleaning characteristic, these tiles can also reduce air pollutants, such as NO_x[106].

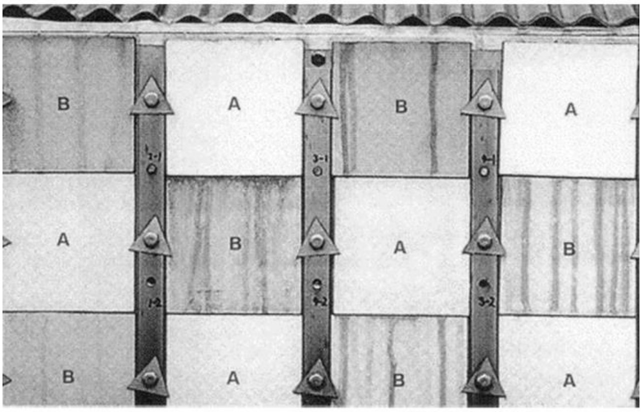

Figure 1.21. Comparison of self-cleaning effect on treated tiles (A) and common tiles (B)[106].

The Italian group *Italcementi* developed the TX Active® [107-109], a product with photocatalytic properties to apply on different substrates, such as mortars, paints or pavements. TX Active gives self-cleaning properties to materials but it has also showed to be able to oxidize nitrogen oxides (NO_x), sulfur oxides (SO_x), volatile organic compounds (VOCs), ammonia, carbon monoxide, hydrogen sulfide and urban smog. Consequently, the performance of these products was characterized in terms of self-cleaning properties and ability to decompose pollutants. One of the most famous buildings protected with this material is the Dives in Misericordia Church in Rome – Figure 1.22. This church was designed by the architect Richard Meier and it was concluded in 2003 [105, 107-109]. Borgo Palazzo Street in Bergamo (Italy) was also protected by this material. This project consisted in the requalification of 500 m of the mentioned street with grey paving stones for the road and red ones for the sidewalks, both coated with TX Active. The pollution level was measured during two weeks in two different occasions, November 2006 and January 2007. The results were compared to the asphalt reference existing in the same street. This new pavement showed a NO_x pollution decrease between 30 % and 40 % [108]. Another well-known application of TX Active is on Umberto I Tunnel in Rome (Italy), outfitted with an artificial UV lighting system in order to enhance the photocatalytic activity. The pollution level was measured before and after this rehabilitee and yielded a NO_x reduction of about 25 %[108]. In France, the efficiency of degradation of NO_x by TiO_2-mortar panels with TX Active was also tested. Three artificial canyon streets were constructed and the level of NO_x pollution was monitored. Differences on the NO_x concentration level were observed between the TiO_2-protected area and the reference canyon. NO_x values in TiO_2 canyon were 37 to 82 % lower than the ones observed for the reference [110].

Figure 1.22. Dives in Misericordia Church in Rome designed by Richard Meier[108].

Boysen® KNoxOUT™ is a photocatalytic commercial paint used for NO_x photoabatement, able to convert pollutants and harmless compounds. This paint was developed for interior and exterior applications; for interior an acrylic-based paint is used, while for exterior it is a silicone-based one. These paints also present self-cleaning, anti-bacterial and de-odorizing properties. To test the efficiency of this new product, the Vinci Car Park in Paris was coated with this paint and an impressive 90 % reduction of NO_x levels was observed. Due to the great first results obtained with this product, other studies are ongoing as project EDSA – "Everyone Deserves Safe Air" [111, 112]. STOphotosan NO_x® is another photocatalytic paint for nitrogen oxides degradation, composed by VLP 7000 from Kronos as photocatalytic TiO_2 and an organic binder [113]. More recently, the host laboratory developed four photocatalytic paints for NO_x abatement. These paints are derived from a commercial water-based vinyl paint by CIN S.A.. The photocatalytic activity of these paints was assessed under laboratory and outdoor conditions. The best performing paint was formulated with photocatalyst PC500 from Cristal and it presents a NO conversion of 70 % under laboratory conditions and 95 % under outdoor conditions [114].

1.3 Objectives and outline of this work

In the last decades, photocatalysis has been presented as a promising approach for air purification. The research on photocatalysis has been following mostly an empirical pathway; the lack of more fundamental and scientific results is noticeable, which cannot be grounded only on the complexity of the topic. A fundamental understanding of the relevant photocatalytic and induced redox reaction mechanisms is essential for further developing this exciting and very relevant research area.

Following, the main goal of this thesis is to contribute to a better understanding of the photocatalysis leading to development of suitable photocatalytic based solutions for the solar abatement of atmospheric NO_x.

This work is divided into three parts. **Part I** (**Chapter 1**) introduces the photocatalysis technology for environmental remediation and, in particular, for the NO_x abatement. The fundamentals of photocatalysis / photoelectrochemistry are reviewed. The main developments on heterogeneous photocatalysis are briefly discussed giving particular emphasis to the pioneer works in this field. **Part II** (**Chapter 2, 3 and 4)** studies the development, characterization and modelling of photocatalytic materials applied to NO_x photoabatement. **Chapter 2** focuses on the development of efficient photocatalytic paints for ambient air purification. Paint coatings were formulated, characterized by different techniques and tested under laboratory and outdoor conditions. The aim of **Chapter 3** is to suggest specific techniques to characterise the efficiency of charge transfer and charge transport within the studied photocatalysts assessing the influence of electronic processes in the photocatalytic performance. In **Chapter 4** a design of experiments for NO photooxidation process was developed to study the influence of operating conditions. An innovative phenomenological model and corresponding experimental validation is proposed, using as reference semiconductor P25 photocatalyst. Finally, **Part III** (**Chapter 5**) presents the main conclusions of this work and suggestions for future developments.

References

1. Colls, J., *Air Pollution.* **2002**
2. Nevers, N., *Air Pollution Control Engineering*. 2th ed: McGrawHill, **2000**.
3. Charles, B., *Everything you need to know about NO_x: Controlling and minimizing pollutant emissions is critical for meeting air quality regulations.* Metal Finishing, 103(11): p. 18-24, **2005**
4. Roy, S., Hegde, M.S., and Madras, G., *Catalysis for NO_x abatement.* Applied Energy, 86(11): p. 2283-2297, **2009**
5. Mahmoudi, S., Baeyens, J., and Seville, J.P.K., *NO_x formation and selective non-catalytic reduction (SNCR) in a fluidized bed combustor of biomass.* Biomass and Bioenergy, 34(9): p. 1393-1409, **2010**
6. EPA, Available from: http://www.epa.gov/; [accessed **November 2015**].
7. EEA, Available from: http://www.eea.europa.eu/; [accessed **November 2015**].
8. Chen, M. and Chu, J., *NO_x photocatalytic degradation on active concrete road surface - from experiment to real-scale application.* Journal of Cleaner Production, 19(11): p. 1266-1272, **2011**
9. Gómez-García, M.A., Pitchon, V., and Kiennemann, A., *Pollution by nitrogen oxides: an approach to NO_x abatement by using sorbing catalytic materials.* Environment International, 31(3): p. 445-467, **2005**
10. Skalska, K., Miller, J.S., and Ledakowicz, S., *Trends in NO_x abatement: A review.* Science of The Total Environment, 408(19): p. 3976-3989, **2010**
11. Allen J. Bard, M.S., Stuart Licht *Fundamentals of Semiconductor Electrochemistry and Photoelectrochemistry*, in *Encyclopedia of Electrochemistry - Semiconductor Electrodes and Photoelectrochemistry,* Wiley-VCH, **2002**.
12. Rajeshwar, K., *Hydrogen generation at irradiated oxide semiconductor–solution interfaces.* Journal of Applied Electrochemistry, 37(7): p. 765-787, **2007**
13. Fujishima, A. and Honda, K., *Electrochemical photolysis of water at a semiconductor electrode.* Nature, 238: p. 37-38, **1972**
14. Memming, R., *Semiconductor Electrochemistry*: Wiley-VCH, **2001**.
15. Luque, A. and Hegedus, S., *Handbook of Photovoltaic Science and Engineering*: Wiley, **2003**.

16. Würfel, P., *Physics of Solar Cells: From Principles to New Concepts*: John Wiley & Sons, **2008**.
17. Nozik, A.J., *Photoelectrochemistry: Applications to Solar Energy Conversion.* Annual Review of Physical Chemistry, 29(1): p. 189-222, **1978**
18. Fujishima, A., Rao, T.N., and Tryk, D.A., *Titanium dioxide photocatalysis.* Journal of Photochemistry and Photobiology, C: Photochemistry Reviews, 1(1): p. 1-21, **2000**
19. Kuhn, K.P., Chaberny, I.F., Massholder, K., Stickler, M., Benz, V.W., Sonntag, H.G., and Erdinger, L., *Disinfection of surfaces by photocatalytic oxidation with titanium dioxide and UVA light.* Chemosphere, 53(1): p. 71-77, **2003**
20. Muneer, M., Bahnemann, D., Qamar, M., Tariq, M.A., and Faisal, M., *Photocatalysed reaction of few selected organic systems in presence of titanium dioxide.* Applied Catalysis A: General, 289(2): p. 224-230, **2005**
21. Yu, J., Zhou, M., Cheng, B., Yu, H., and Zhao, X., *Ultrasonic preparation of mesoporous titanium dioxide nanocrystalline photocatalysts and evaluation of photocatalytic activity.* Journal of Molecular Catalysis A: Chemical, 227: p. 75-80, **2005**
22. Mahmoodi, N.M., Arami, M., Limaee, N.Y., Gharanjig, K., and Nourmohammadian, F., *Nanophotocatalysis using immobilized titanium dioxide nanoparticle: Degradation and mineralization of water containing organic pollutant: Case study of Butachlor.* Materials Research Bulletin, 42(5): p. 797-806, **2007**
23. Markowska-Szczupak, A., Ulfig, K., and Morawski, A.W., *The application of titanium dioxide for deactivation of bioparticulates: An overview.* Catalysis Today, 169(1): p. 249-257, **2011**
24. Hager, S. and Bauer, R., *Heterogeneous photocatalytic oxidation of organics for air purification by near UV irradiated titanium dioxide.* Chemosphere, 38(7): p. 1549-1559, **1999**
25. Teh, C.M. and Mohamed, A.R., *Roles of titanium dioxide and ion-doped titanium dioxide on photocatalytic degradation of organic pollutants (phenolic compounds and dyes) in aqueous solutions: A review.* Journal of Alloys and Compounds, 509(5): p. 1648-1660, **2011**

26. Lin, C., Song, Y., Cao, L., and Chen, S., *Effective photocatalysis of functional nanocomposites based on carbon and* TiO_2 *nanoparticles.* Nanoscale, 5(11): p. 4986-4992, **2013**
27. Dong, H., Zeng, G., Tang, L., Fan, C., Zhang, C., He, X., and He, Y., *An overview on limitations of* TiO_2*-based particles for photocatalytic degradation of organic pollutants and the corresponding countermeasures.* Water Research, 79: p. 128-146, **2015**
28. Carp, O., Huisman, C.L., and Reller, A., *Photoinduced reactivity of titanium dioxide.* Progress in Solid State Chemistry, 32: p. 33-177, **2004**
29. Meinhold, G., *Rutile and its applications in earth sciences.* Earth-Science Reviews, 102: p. 1-28, **2010**
30. Alemany, L.J., Bañares, M.A., Pardo, E., Martín-Jiménez, F., and Blasco, J.M., *Morphological and Structural Characterization of a Titanium Dioxide System.* Materials Characterization, 44(3): p. 271-275, **2000**
31. Hu, Y., Tsai, H.L., and Huang, C.L., *Effect of brookite phase on the anatase–rutile transition in titania nanoparticles.* Journal of the European Ceramic Society, 23(5): p. 691-696, **2003**
32. Birnie, M., Riffat, S., and Gillott, M., *Photocatalytic reactors: design for effective air purification.* International Journal of Low-Carbon Technologies, 1(1): p. 47-58, **2006**
33. Hassan, M.M., Dylla, H., Mohammad, L.N., and Rupnow, T., *Evaluation of the durability of titanium dioxide photocatalyst coating for concrete pavement.* Construction and Building Materials, 24(8): p. 1456-1461, **2010**
34. Bellardita, M., Di Paola, A., Palmisano, L., Parrino, F., Buscarino, G., and Amadelli, R., *Preparation and photoactivity of samarium loaded anatase, brookite and rutile catalysts.* Applied Catalysis B: Environmental, 104: p. 291-299, **2011**
35. Zhang, J., Yan, S., Fu, L., Wang, F., Yuan, M., Luo, G., Xu, Q., Wang, X., and Li, C., *Photocatalytic Degradation of Rhodamine B on Anatase, Rutile, and Brookite* TiO_2*.* Chinese Journal of Catalysis, 32: p. 983-991, **2011**
36. Águia, C., Ângelo, J., Madeira, L.M., and Mendes, A., *Photo-oxidation of NO using an exterior paint - Screening of various commercial titania in powder*

pressed and paint films. Journal of Environmental Management, 92(7): p. 1724-1732, **2011**

37. Rehman, S., Ullah, R., Butt, A.M., and Gohar, N.D., *Strategies of making TiO_2 and ZnO visible light active.* Journal of Hazardous Materials, 170(2–3): p. 560-569, **2009**
38. Hoffmann, M.R., Martin, S.T., Choi, W., and Bahnemann, D.W., *Environmental Applications of Semiconductor Photocatalysis.* Chemical Reviews, 95(1): p. 69-96, **1995**
39. Yu, J.C., Yu, J., Ho, W., and Zhang, L., *Preparation of highly photocatalytic active nano-sized TiO_2 particles ultrasonic irradiation.* Chemical Communications, (19): p. 1942-1943, **2001**
40. Hussain, M., Ceccarelli, R., Marchisio, D.L., Fino, D., Russo, N., and Geobaldo, F., *Synthesis, characterization, and photocatalytic application of novel TiO_2 nanoparticles.* Chemical Engineering Journal, 157(1): p. 45-51, **2010**
41. Lydakis-Simantiris, N., Riga, D., Katsivela, E., Mantzavinos, D., and Xekoukoulotakis, N.P., *Disinfection of spring water and secondary treated municipal wastewater by TiO_2 photocatalysis.* Desalination, 250(1): p. 351-355, **2010**
42. Abramovic, B., Sojic, D., Despotovic, V., Vione, D., Pazzi, M., and Csanádi, J., *A comparative study of the activity of TiO_2 Wackherr and Degussa P25 in the photocatalytic degradation of picloram.* Applied Catalysis B: Environmental, 105: p. 191-198, **2011**
43. Águia, C., Ângelo, J., Madeira, L.M., and Mendes, A., *Influence of paint components on photoactivity of P25 titania toward NO abatement.* Polymer Degradation and Stability, 96(5): p. 898-906, **2011**
44. Sikkema, J.K., Ong, S.K., and Alleman, J.E., *Photocatalytic concrete pavements: Laboratory investigation of NO oxidation rate under varied environmental conditions.* Construction and Building Materials, 100: p. 305-314, **2015**
45. Spasiano, D., Marotta, R., Malato, S., Fernandez-Ibañez, P., and Di Somma, I., *Solar photocatalysis: Materials, reactors, some commercial, and pre-industrialized applications. A comprehensive approach.* Applied Catalysis B: Environmental, 170–171: p. 90-123, **2015**

46. Devahasdin, S., Fan Jr, C., Li, K., and Chen, D.H., *TiO_2 photocatalytic oxidation of nitric oxide: transient behavior and reaction kinetics.* Journal of Photochemistry and Photobiology, A: Chemistry, 156(1–3): p. 161-170, **2003**
47. Jeong, J., Sekiguchi, K., Lee, W., and Sakamoto, K., *Photodegradation of gaseous volatile organic compounds (VOCs) using TiO_2 photoirradiated by an ozone-producing UV lamp: decomposition characteristics, identification of by-products and water-soluble organic intermediates.* Journal of Photochemistry and Photobiology A: Chemistry, 169(3): p. 279-287, **2005**
48. Wang, H., Wu, Z., Zhao, W., and Guan, B., *Photocatalytic oxidation of nitrogen oxides using TiO_2 loading on woven glass fabric.* Chemosphere, 66(1): p. 185-190, **2007**
49. Hüsken, G., Hunger, M., and Brouwers, H.J.H., *Experimental study of photocatalytic concrete products for air purification.* Building and Environment, 44(12): p. 2463-2474, **2009**
50. Yu, Q.L. and Brouwers, H.J.H., *Indoor air purification using heterogeneous photocatalytic oxidation. Part I: Experimental study.* Applied Catalysis B: Environmental, 92(3–4): p. 454-461, **2009**
51. Chin, S., Park, E., Kim, M., Jeong, J., Bae, G. N., and Jurng, J., *Preparation of TiO_2 ultrafine nanopowder with large surface area and its photocatalytic activity for gaseous nitrogen oxides.* Powder Technology, 206(3): p. 306-311, **2011**
52. Martinez, T., Bertron, A., Ringot, E., and Escadeillas, G., *Degradation of NO using photocatalytic coatings applied to different substrates.* Building and Environment, 46(9): p. 1808-1816, **2011**
53. Herrmann, J. M., *Photocatalysis fundamentals revisited to avoid several misconceptions.* Applied Catalysis, B: Environmental, 99(3–4): p. 461-468, **2010**
54. Uner, D., Bayar, I., and Tabari, T., *The influence of relative humidity on photocatalytic oxidation of nitric oxide (NO) over TiO_2.* Applied Surface Science, 354, Part B: p. 260-266, **2015**
55. Jeong, J., Jurng, J., Jin, S., and Kim, Y., *Optimization of the removal efficiency of nitrogen oxides in the air using a low-pressure Hg lamp.* Journal of Photochemistry and Photobiology A: Chemistry, 197(1): p. 50-54, **2008**

56. Maggos, T., Bartzis, J.G., Leva, P., and Kotzias, D., *Application of photocatalytic technology for NO_x removal.* Applied Physics A: Materials Science & Processing, 89(1): p. 81-84, **2007**
57. Melo, J.V.S. and Trichês, G., *Evaluation of the influence of environmental conditions on the efficiency of photocatalytic coatings in the degradation of nitrogen oxides (NO_x).* Building and Environment, 49: p. 117-123, **2012**
58. Toma, F., Bertrand, G., Klein, D., and Coddet, C., *Photocatalytic removal of nitrogen oxides via titanium dioxide.* Environmental Chemistry Letters, 2(3): p. 117-121, **2004**
59. Ao, C.H. and Lee, S.C., *Enhancement effect of TiO_2 immobilized on activated carbon filter for the photodegradation of pollutants at typical indoor air level.* Applied Catalysis B: Environmental, 44(3): p. 191-205, **2003**
60. Yu, Q.L., Ballari, M.M., and Brouwers, H.J.H., *Indoor air purification using heterogeneous photocatalytic oxidation. Part II: Kinetic study.* Applied Catalysis B: Environmental, 99(1–2): p. 58-65, **2010**
61. Demeestere, K., Visscher, A.D., Dewulf, J., Leeuwen, M.V., and Langenhove, H.V., *A new kinetic model for titanium dioxide mediated heterogeneous photocatalytic degradation of trichloroethylene in gas-phase.* Applied Catalysis B: Environmental, 54(4): p. 261-274, **2004**
62. Valencia, S., Cataño, F., Rios, L., Restrepo, G., and Marín, J., *A new kinetic model for heterogeneous photocatalysis with titanium dioxide: Case of non-specific adsorption considering back reaction.* Applied Catalysis B: Environmental, 104(3–4): p. 300-304, **2011**
63. Barka, N., Qourzal, S., Assabbane, A., and Ait-Ichou, Y., *Kinetic modeling of the photocatalytic degradation of methyl orange by supported TiO_2.* Journal of Environmental Science & Engineering, 4(5): p. 1-5, **2010**
64. Folli, A., Campbell, S.B., Anderson, J.A., and Macphee, D.E., *Role of TiO_2 surface hydration on NO oxidation photo-activity.* Journal of Photochemistry and Photobiology A: Chemistry, 220(2–3): p. 85-93, **2011**
65. Hunger, M., Hüsken, G., and Brouwers, H.J.H., *Photocatalytic degradation of air pollutants — From modeling to large scale application.* Cement and Concrete Research, 40(2): p. 313-320, **2010**

66. Paz, Y., *Photocatalytic Treatment of Air: From Basic Aspects to Reactors*, in *Advances in Chemical Engineering*, I.d.L. Hugo and R. Benito Serrano, Editors, Academic Press. p. 289-336, **2009**.
67. Paz, Y., *Application of TiO_2 photocatalysis for air treatment: Patents' overview.* Applied Catalysis, B: Environmental, 99(3–4): p. 448-460, **2010**
68. Spadavecchia, F., Cappelletti, G., Ardizzone, S., Bianchi, C.L., Cappelli, S., Oliva, C., Scardi, P., Leoni, M., and Fermo, P., *Solar photoactivity of nano-N-TiO_2 from tertiary amine: role of defects and paramagnetic species.* Applied Catalysis B: Environmental, 96(3–4): p. 314-322, **2010**
69. Águia, C., Ângelo, J., Madeira, L.M., and Mendes, A., *Influence of photocatalytic paint components on the photoactivity of P25 towards NO abatement.* Catalysis Today, 151(1–2): p. 77-83, **2010**
70. Ao, C.H., Lee, S.C., Mak, C.L., and Chan, L.Y., *Photodegradation of volatile organic compounds (VOCs) and NO for indoor air purification using TiO_2: promotion versus inhibition effect of NO.* Applied Catalysis, A: General, 42(2): p. 119-129, **2003**
71. Toma, F. L., Guessasma, S., Klein, D., Montavon, G., Bertrand, G., and Coddet, C., *Neural computation to predict TiO_2 photocatalytic efficiency for nitrogen oxides removal.* Journal of Photochemistry and Photobiology A: Chemistry, 165(1–3): p. 91-96, **2004**
72. Toma, F. L., Bertrand, G., Chwa, S.O., Meunier, C., Klein, D., and Coddet, C., *Comparative study on the photocatalytic decomposition of nitrogen oxides using TiO_2 coatings prepared by conventional plasma spraying and suspension plasma spraying.* Surface and Coatings Technology, 200(20–21): p. 5855-5862, **2006**
73. Peral, J. and Ollis, D.F., *Heterogeneous photocatalytic oxidation of gas-phase organics for air purification: Acetone, 1-butanol, butyraldehyde, formaldehyde, and m-xylene oxidation.* Journal of Catalysis, 136(2): p. 554-565, **1992**
74. Lewandowski, M. and Ollis, D.F., *A Two-Site kinetic model simulating apparent deactivation during photocatalytic oxidation of aromatics on titanium dioxide (TiO_2).* Applied Catalysis B: Environmental, 43(4): p. 309-327, **2003**

75. Tsoukleris, D.S., Maggos, T., Vassilakos, C., and Falaras, P., *Photocatalytic degradation of volatile organics on TiO_2 embedded glass spherules.* Catalysis Today, 129(1–2): p. 96-101, **2007**
76. Komazaki, Y., Shimizu, H., and Tanaka, S., *A new measurement method for nitrogen oxides in the air using an annular diffusion scrubber coated with titanium dioxide.* Atmospheric Environment, 33(27): p. 4363-4371, **1999**
77. Lim, T.H., Jeong, S.M., Kim, S.D., and Gyenis, J., *Photocatalytic decomposition of NO by TiO_2 particles.* Journal of Photochemistry and Photobiology A: Chemistry, 134(3): p. 209-217, **2000**
78. Matsuda, S. and Hatano, H., *Photocatalytic removal of NO_x in a circulating fluidized bed system.* Powder Technology, 151(1–3): p. 61-67, **2005**
79. Maggos, T., Bartzis, J.G., Liakou, M., and Gobin, C., *Photocatalytic degradation of NO_x gases using TiO_2-containing paint: A real scale study.* Journal of Hazardous Materials, 146(3): p. 668-673, **2007**
80. Allen, N.S., Edge, M., Verran, J., Stratton, J., Maltby, J., and Bygott, C., *Photocatalytic titania based surfaces: Environmental benefits.* Polymer Degradation and Stability, 93(9): p. 1632-1646, **2008**
81. Folli, A., Pade, C., Hansen, T.B., De Marco, T., and Macphee, D.E., *TiO_2 photocatalysis in cementitious systems: Insights into self-cleaning and depollution chemistry.* Cement and Concrete Research, 42(3): p. 539-548, **2012**
82. Kaneko, M. and Okura, I., *Photocatalysis: science and technology*: Kodansha, Vol. **2002**.
83. Rao, K.V.S., Subrahmanyam, M., and Boule, P., *Immobilized TiO_2 photocatalyst during long-term use: decrease of its activity.* Applied Catalysis B: Environmental, 49(4): p. 239-249, **2004**
84. Robert, D., Keller, V., and Keller, N., *Immobilization of a Semiconductor Photocatalyst on Solid Supports: Methods, Materials, and Applications*, in *Photocatalysis and Water Purification,* Wiley-VCH Verlag GmbH & Co. KGaA. p. 145-178, **2013**.
85. Varshney, G., Kanel, S.R., Kempisty, D.M., Varshney, V., Agrawal, A., Sahle-Demessie, E., Varma, R.S., and Nadagouda, M.N., *Nanoscale TiO_2 films and their*

application in remediation of organic pollutants. Coordination Chemistry Reviews, 306, Part 1: p. 43-64, **2016**

86. Baan, R., Straif, K., Grosse, Y., Secretan, B., El Ghissassi, F., and Cogliano, V., *Carcinogenicity of carbon black, titanium dioxide, and talc.* The Lancet Oncology, 7(4): p. 295-296, **2006**
87. Fernández, A., Lassaletta, G., Jimánez, V.M., Justo, A., Gonzáez-Elipe, A.R., Herrmann, J.M., Tahiri, H., and Ait-Ichou, Y., *Preparation and characterization of TiO_2 photocatalysts supported on various rigid supports (glass, quartz and stainless steel). Comparative studies of photocatalytic activity in water purification.* Applied Catalysis B: Environmental, 7: p. 49-63, **1995**
88. Herrmann, J.M., Tahiri, H., Ait-Ichou, Y., Lassaletta, G., González-Elipe, A.R., and Fernández, A., *Characterization and photocatalytic activity in aqueous medium of TiO_2 and Ag-TiO_2 coatings on quartz.* Applied Catalysis B: Environmental, 13(3–4): p. 219-228, **1997**
89. Kwon, C.H., Kim, J.H., Jung, I.S., Shin, H., and Yoon, K.H., *Preparation and characterization of TiO_2–SiO_2 nano-composite thin films.* Ceramics International, 29(8): p. 851-856, **2003**
90. Lim, L.L.P., Lynch, R.J., and In, S.I., *Comparison of simple and economical photocatalyst immobilisation procedures.* Applied Catalysis A: General, 365(2): p. 214-221, **2009**
91. Shan, A.Y., Ghazi, T.I.M., and Rashid, S.A., *Immobilisation of titanium dioxide onto supporting materials in heterogeneous photocatalysis: A review.* Applied Catalysis A: General, 389(1–2): p. 1-8, **2010**
92. Rajendran, K., Senthil Kumar, V., and Anitha Rani, K., *Synthesis and characterization of immobilized activated carbon doped TiO_2 thin films.* Optik - International Journal for Light and Electron Optics, 125(8): p. 1993-1996, **2014**
93. Páez, L.R. and Matousek, J., *Properties of sol-gel TiO_2 layers on glass substrate.* Ceramics - Silikáty, 48 (2): p. 66-71, **2004**
94. Chen, Y. and Dionysiou, D.D., *TiO_2 photocatalytic films on stainless steel: The role of Degussa P-25 in modified sol–gel methods.* Applied Catalysis B: Environmental, 62(3–4): p. 255-264, **2006**

95. Byun, D., Jin, Y., Kim, B., Kee Lee, J., and Park, D., *Photocatalytic TiO_2 deposition by chemical vapor deposition.* Journal of Hazardous Materials, 73(2): p. 199-206, **2000**
96. Ding, Z., Hu, X., Yue, P.L., Lu, G.Q., and Greenfield, P.F., *Synthesis of anatase TiO_2 supported on porous solids by chemical vapor deposition.* Catalysis Today, 68: p. 173-182, **2001**
97. Mills, A., Elliott, N., Parkin, I.P., O'Neill, S.A., and Clark, R.J., *Novel TiO_2 CVD films for semiconductor photocatalysis.* Journal of Photochemistry and Photobiology A: Chemistry, 151(1–3): p. 171-179, **2002**
98. Rachel, A., Subrahmanyam, M., and Boule, P., *Comparison of photocatalytic efficiencies of TiO_2 in suspended and immobilised form for the photocatalytic degradation of nitrobenzenesulfonic acids.* Applied Catalysis B: Environmental, 37(4): p. 301-308, **2002**
99. W. Zhang, S. Zhu, Y. Li, and Wang., F., *Photocatalytic Property of TiO_2 Films Deposited by Pulsed DC Magnetron Sputtering.* J. Mater. Sci. Technol., 20: p. 31-34, **2004**
100. Zhang, C., Ding, W., Wang, H., Chai, W., and Ju, D., *Influences of working pressure on properties for TiO_2 films deposited by DC pulse magnetron sputtering.* Journal of Environmental Sciences, 21(6): p. 741-744, **2009**
101. Byrne, J.A., Eggins, B.R., Brown, N.M.D., McKinney, B., and Rouse, M., *Immobilisation of TiO_2 powder for the treatment of polluted water.* Applied Catalysis B: Environmental, 17(1-2): p. 25-36, **1998**
102. Rachel, A., Lavedrine, B., Subrahmanyam, M., and Boule, P., *Use of porous lavas as supports of photocatalysts.* Catalysis Communications, 3(4): p. 165-171, **2002**
103. Hashimoto, K., Irie, H., and Fujishima, A., *TiO_2 Photocatalysis: A historical Overview and Future Prospect.* Japanese Journal of Applied Physics, 44(12): p. 8269-8285, **2005**
104. Masakazu, A., *Utilization of TiO_2 photocatalysts in green chemistry.* Pure and applied chemistry, 72: p. 1265-1270, **2000**
105. Osburn, L., *Literature review on the application of titanium dioxide reactive surfaces on urban infrastructure for depolluting and self-cleaning applications.*

5th Post Graduate Conference on Construction Industry Development, Bloemfontein, South Africa, 16-18 March 2008: p. 11, **2008**

106. Fujishima, A. and Zhang, X., *Titanium dioxide photocatalysis: present situation and future approaches.* Comptes Rendus Chimie, 9(5-6): p. 750-760, **2006**
107. Cassar, L., *Photocatalysis of Cementitious Materials: Clean Buildings and Clean Air.* MRS Bulletin, 29: p. 328-331, **2004**
108. Italcementi, *TX Active The Photocatalytic Active Principle*, in *Tecnical Report*: Bergamo, Italy, **2009**.
109. Pacheco-Torgal, F. and Jalali, S., *Nanotechnology: Advantages and drawbacks in the field of construction and building materials.* Construction and Building Materials, 25(2): p. 582-590, **2011**
110. Maggos, T., Plassais, A., Bartzis, J.G., Vasilakos, C., Moussiopoulos, N., and Bonafous, L., *Photocatalytic degradation of* NO_x *in a pilot street canyon configuration using* TiO_2*-mortar panels.* Environmental Monitoring and Assessment, 136(1-3): p. 35-44, **2008**
111. Boysen, Available from: http://www.knoxoutpaints.com/; [accessed **November 2015**].
112. EDSA, B.P., Available from: http://boysenknoxoutproject.com/; [accessed **November 2015**].
113. Laufs, S., Burgeth, G., Duttlinger, W., Kurtenbach, R., Maban, M., Thomas, C., Wiesen, P., and Kleffmann, J., *Conversion of nitrogen oxides on commercial photocatalytic dispersion paints.* Atmospheric Environment, 44(19): p. 2341-2349, **2010**
114. Ângelo, J., Andrade, L., and Mendes, A., *Highly active photocatalytic paint for* NO_x *abatement under real-outdoor conditions.* Applied Catalysis A: General, 484: p. 17-25, **2014**

PART II: Chapter 2

Highly active photocatalytic paint for NO_x abatement under real-outdoor conditions

Chapter 2.

Highly active photocatalytic paint for NO_x abatement under real-outdoor conditions

Joana Ângelo, Luísa Andrade and Adélio Mendes

(*Applied Catalysis A: General 2014, 484, 17–25*)

Abstract

In this work the photocatalytic activity of paints incorporating commercial titanium dioxide for outdoor nitrogen oxide (NO) photoabatement is assessed. The paint acts as a 3D support of the photocatalyst and thus allows a larger amount of TiO_2 nanoparticles to absorb light and to contact with pollutants, when compared with a 2D photocatalytic surface. NO conversion and selectivity towards nitrites and nitrates were determined according to the standard ISO 22197-1:2007 (E). Paint coatings were formulated and tested under laboratory and outdoor conditions. The best paint formulation incorporates CristalACTiV™ PC500 photocatalyst from Cristal and calcium carbonate extender, presenting a NO conversion of *ca.* 70 % and a selectivity of *ca.* 40 % under laboratory conditions. The same photocatalyst but characterized in the form of an optically thick film of compressed powder presented *ca.* 95 % and 45 % of conversion and selectivity, respectively. Under the real-outdoor conditions, the best performing paint showed a NO conversion of about 95 %.

Keywords

NO_x abatement; Photocatalysis; Titanium dioxide; Photocatalytic paint.

2.1 Introduction

NO_x pollution is responsible for well-known environmental problems such as production of tropospheric ozone, acid rains and global warming but it can also affect humans health, in particular the respiratory and immune systems. Photocatalysis with titanium dioxide (TiO_2) is now being seen as a very promising approach to decompose these pollutants [1-3]. Several materials incorporating photocatalytic titanium dioxide used for air purification were already reported, *e.g.* tiles, cement mortars and paints [4]. Mortars and paint coatings are the building materials most used for this kind of applications [5-10]. Although several works study the photoabatement of NO_x under lab conditions, there is a lack of studies reporting NO_x photoabatement under real outdoor conditions. In the first chapter of this thesis examples of outdoor studies were presented, such as the case of Borgo Palazzo Street in Bergamo, Italy [11]; the three artificial canyon streets. in France [12]; the Umberto I Tunnel in Rome, Italy [13]; the Vinci Car Park in Paris, France [14]; the playground of Sir John Cass School, in London [15, 16]; and the project EDSA – "Everyone Deserves Safe Air" in Philippines [17, 18]. More recently, project Light2Cat was presented concerning the development of a modified TiO_2 photocatalyst active under visible and UV light. The new photocatalyst, which can be incorporated in building elements such as concrete, was optimized to respond under typical solar radiation of a large range of latitudes [19]. On the other hand, Suárez *et al.*[20] described a new experimental setup for testing photocatalytic materials, SYPHOMA. This experimental setup allows determining the photocatalytic activity under sunlight for treating outdoor polluted air; it was assessed for NO_x photoabatement using photocatalytic-coated asphalts. NO_x concentrations, relative humidity, irradiance and temperature are recorded during all the experiments. All these efforts on assessing results under real-field applications foster the use of photocatalytic materials as an important agent to reduce pollutants concentrations in the air.

Considering the specific application of NO degradation, photocatalytic paints show two main advantages when compared with other kind of construction supports. Paint coatings can be applied in different constructive elements, such as streets, buildings, tunnels, and they present the advantage of being a 3D layer where TiO_2 nanoparticles are available for photocatalysis up to the paint film optic thickness, *ca.* 100 μm. A photocatalytic paint coating has a very large interfacial area available for photocatalysis, originating then very photoactive surfaces to degrade pollutants. Even though titanium dioxide is one of the major components on the formulation of a paint (its function is to give opacity to the paint), this titanium dioxide is pigmentary, mainly in rutile phase for preventing any photoactivity. Consequently, the paint formulation needs to be modified for incorporating photocatalytic titanium dioxide, normally or essentially, anatase. The presence of pigmentary TiO_2 in paints jeopardizes the photoactivity because it acts as a blocking agent for the solar radiation resulting in low levels of NO conversion and selectivity [21]. Thus, pigmentary TiO_2 should be removed from the paint formulation and replaced by extenders, which are beneficial for the photoactivity of the paint film. In the present work, an exterior water-based paint was formulated to incorporate two commercial photocatalysts: P25 from Evonik and PC500 from Cristal. The photocatalysts were characterized in powder form [21] and after incorporation in the formulated paint; the photocatalytic activity was assessed according to standard ISO 22197-1:2007 ["Fine ceramics (advanced ceramics, advanced technical ceramics) - Test method for air-purification performance of semiconducting photocatalytic materials - Part 1: Removal of nitric oxide"] and under real-outdoor conditions.

2.2 Experimental

2.2.1 Photocatalytic films

Two samples of commercial photocatalytic titanium dioxide were tested for NO photoabatement: P25 from Evonik and PC500 from Cristal. The photocatalysts properties are detailed in Table 2.1.

Table 2.1. Photocatalyst properties provide by manufacturers.

	P25	**PC500**
Manufacturer	Evonik	Cristal
Crystal structure	~80 % Anatase / ~20 % Rutile	>99 % Anatase
Crystal size (nm)	25	5-10
Shape	Primary particles	Agglomerates
Surface area (m^2g^{-1})	50	345
Agglomerate size (µm)	n.p.	1.2-1.7

The above described photocatalysts were then incorporated in a paint coating and characterized to assess photo-oxidation of NO. The developed photocatalytic paint was optimized from a commercial exterior water-based paint (vinyl paint) described elsewhere [22]. The main components of this commercial paint are: pigmentary TiO_2 (18 wt.%), water (30 wt.%), extenders (18 wt.%: $CaCO_3$ and silicates), polymer extender slurry (8 wt.%), binder slurry (20 wt.%) and additives slurry (6 wt.%). This paint has high porosity due to a pigment volume concentration (PVC) slightly above the critical value (CPVC), thus allowing the easy access of the photocatalyst to the pollutant.

Four different paint formulations were tested – Table 2.2 - loaded with two different commercial photocatalysts, P25 and PC500. The commercial vinyl paint has 18 wt.% of pigmentary TiO_2 in wet basis; this paint is hereafter named as *Reference Paint* (RP). The maximum photocatalyst content incorporated in the formulated paints was 9 wt.% (wet base): paints #1 and #3 contained 9 wt.% of pigmentary TiO_2 and 9 wt.% of photocatalytic TiO_2, while paints #2 and #4 contained 9 wt.% of calcium carbonate instead of the pigmentary TiO_2. The paint films were applied on aluminum slabs of 10 × 5 cm^2 with a wet thickness of 200 μm.

Table 2.2. Paint reformulation composition.

	Components			
Paint	*Pigmentary TiO_2*	*$CaCO_3$*	*P25*	*PC500*
Reference Paint	18 wt.%			
#1	9 wt.%		9 wt.%	
#2		9 wt.%	9 wt.%	
#3	9 wt.%			9 wt.%
#4		9 wt.%		9 wt.%

2.2.2 Photocatalytic tests

The performance of the photocatalyst was characterized by two parameters: conversion of NO (equation 2.1) and selectivity to the formation of ionic species (equation 2.2):

$$X_{NO} = \left(\frac{[NO]_{in} - [NO]_{out}}{[NO]_{in}} \right) \times 100 \qquad 2.1$$

$$S = \left(1 - \frac{[NO_2]_{out}}{[NO]_{in} - [NO]_{out}} \right) \times 100 \qquad 2.2$$

where X_{NO} is the conversion of NO, S is the selectivity to the formation of ionic species, $[NO]$ and $[NO_2]$ stand for the concentration of NO and NO_2, respectively, and the superscripts (*in* and *out*) refer to the reactor's inlet and outlet streams. The radicals $OH^{\bullet}$ are responsible for the oxidation of contaminants, as mentioned previously. When NO reacts with $OH^{\bullet}$ some species can be formed, such as HNO_2 ($H^+ + NO_2^-$), HNO_3 ($H^+ + NO_3^-$) and NO_2 – Figure 2.1. Since NO_2 is even more harmful than NO to human health, the desired reaction products are the ionic species (NO_2^- and NO_3^-).

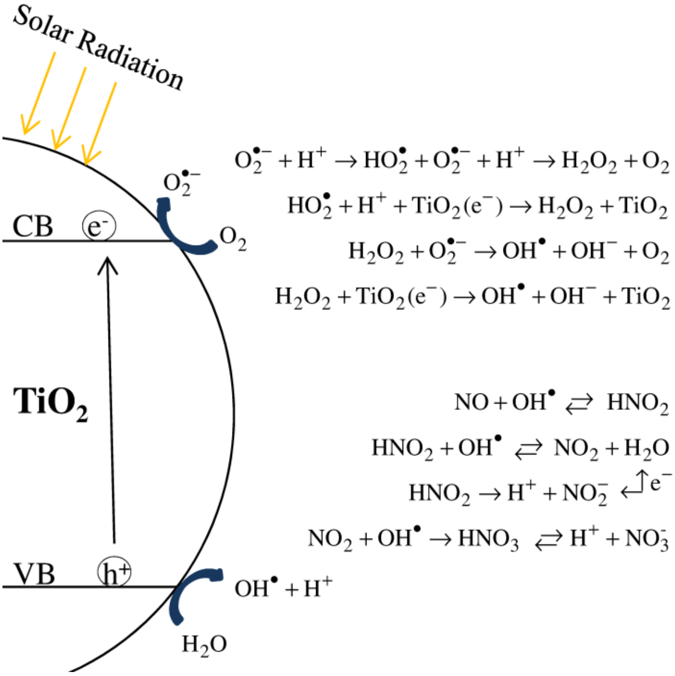

Figure 2.1. Mechanism of photocatalysis with main reactions.

(i) Laboratory experimental setup

An experimental setup based on standard ISO 22197-1:2007 [“Fine ceramics (advanced ceramics, advanced technical ceramics) - Test method for air-purification performance of semiconducting photocatalytic materials - Part 1: Removal of nitric oxide”] was used to evaluate the photocatalytic activity of powder pressed and paint films. This setup consists of four main sections: i) feed, ii) reactor, iii) NO_x quantification and iv) computer monitoring/control – Figure 2.2.

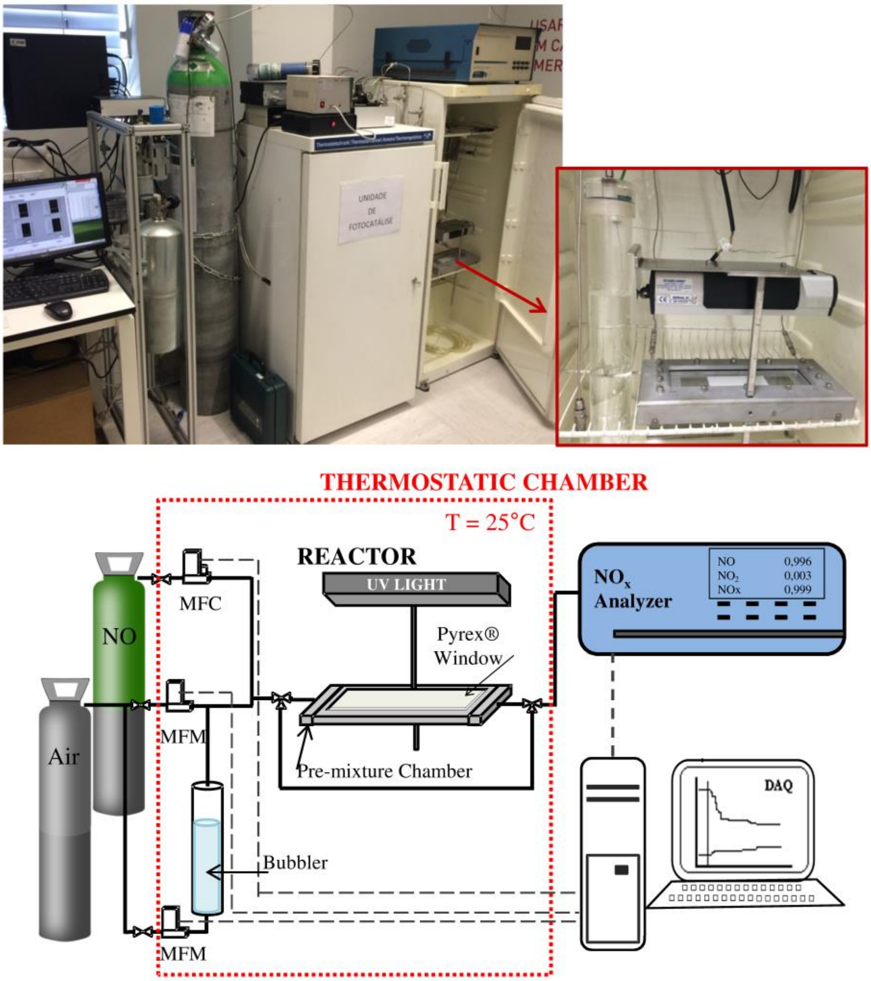

Figure 2.2. Experimental setup used for the laboratorial photocatalytic experiments.

In the first section, the gas stream with the desired NO concentration, relative humidity and flow rate, is prepared and fed to the photoreactor. The feeding system consists of a flow controller of NO (MFC 0-0.1 $L_N \cdot min^{-1}$ - Hi-Tech Bronkhorts), two flow meters for dry and wet air (MFM 0-1 $L_N \cdot min^{-1}$ - Hi-Tech Bronkhorts), respectively, and a bubbler used to humidify the dry air (100 % relative humidity under test temperature and feed flow rate); the latter allows to obtain a stream at any relative humidity between 0 and 100 %.

The reaction section is composed by a photoreactor (with a Pyrex® window) designed to hold the samples, minimizing dead and stagnant volumes. Above the reactor is the UV lamp (Vilbert Lourmat – BLB 365 nm, 2 lamps of 6 W each), which distance to the photoreactor window can be varied. NO and NO_2 concentrations are quantified using a chemiluminescence analyzer (Thermo Electron 42C), as suggested in the standard. A computer controls the experimental set-up and acquires the relevant data. The reactor is placed inside a thermostatic cabin to ensure controlled and constant temperature. Photocatalytic tests were performed at a feed rate of 0.7 $L \cdot min^{-1}$ of NO at 1 ppm_v in air and 50 % of relative humidity, at 25 °C with an irradiance of 10 $W \cdot m^{-2}$.

(ii) Outdoor experimental setup

An outdoor experimental setup was designed and assembled to determine the NO_x photoabatement efficiency of photocatalytic paints when irradiated directly by sunlight – Figure 2.3.

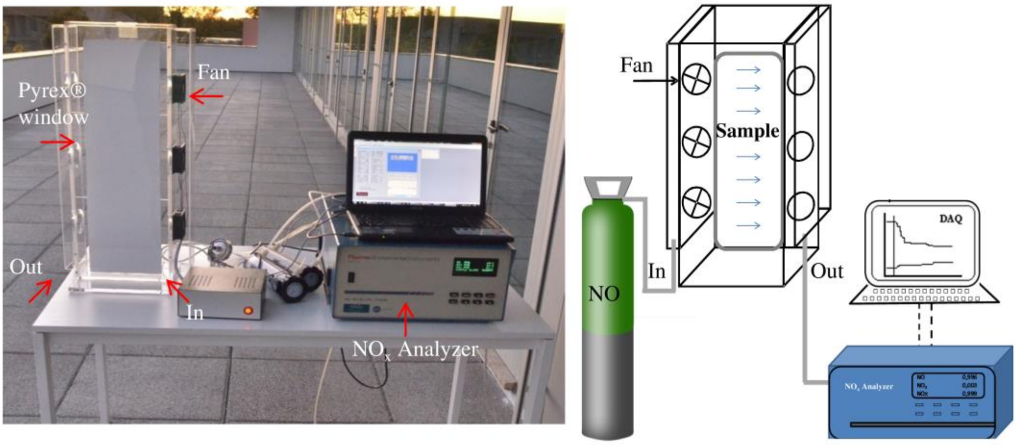

Figure 2.3. Experimental setup used for the outdoor experiments (in the setup sketch, blue arrows represent the gas flow direction).

This setup comprises also four main sections: i) feed, ii) reactor, iii) NO_x quantification and iv) computer acquisition and control. A NO stream in air (*ca.*150 - 200 ppb_v) was fed to the reactor. The photoreactor is made of acrylic material with a Pyrex® window. The paint samples are applied in a fiber cement board (70 × 20 cm^2, Figure 2.4) and they are placed on the back of the photoreactor.

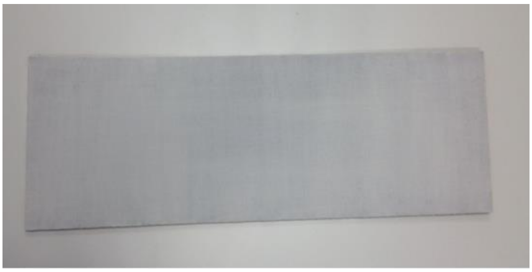

Figure 2.4. Example of one sample tested in outdoor characterization.

The flow passes through the reactor contacting with the samples; NO concentration is then quantified using a chemiluminescence analyzer (Thermo Electron 42C) and all the experiments are controlled using a computer.

2.2.3 Diffuse reflectance analyses

Diffuse reflectance spectroscopy can be used to obtain the absorption properties of crystalline and amorphous materials [23, 24]. The band gap of a sample can be obtained from the Tauc equation, which relates the diffuse reflectance and the Kubelka-Munk model with the excitation frequency [24]:

$$(h\nu\ \mathrm{F}(R_\infty))^{1/n} = A'(h\nu - E_{BG}) \qquad 2.3$$

where h is Planck's constant, ν is frequency of vibration, A' is a proportional constant and E_{BG} is the band gap energy. This equation is obtained by multiplying the Kubelka-Munk equation by the energy of the incident radiation ($E = h\nu$) and powered to a coefficient n, according to the type of the electronic transition of the material. For indirect transitions, n equals 2 and for direct transition n is 1/2. Plotting the modified Kubelka-Munk equation as a function of the incident radiation ($h\nu$ (eV)), the band gap of the semiconductor can be obtained extrapolating the linear part of this curve to the x-axis, the so-called Tauc plot; the band gap energy is read at the intersection. Diffuse reflectance of the different samples were obtained in a Shimatzu *UV-3600* UV-VIS-NIR spectrophotometer, equipped with a 150 mm integrating sphere and using $BaSO_4$ as 100 % reflectance standard. The samples were pressed to form a flat disc that fit into the spectrophotometer sample holder.

2.2.4 SEM and XRD analyses

The morphology and composition of the photocatalysts and photocatalytic paints were obtained from scanning electron microscopy (SEM) coupled with energy dispersive X-ray (EDS) analysis. A FEI Quanta 400FEG ESEM/EDAX Genesis X4M apparatus equipped with a Schottky field emission gun (for optimal spatial resolution) was used for the characterization of the surface morphology of the photocatalysts powders and for photocatalytic paints. These SEM/EDS analyses were made at CEMUP (Centro de Materiais da Universidade do Porto).

The crystallographic characterization of samples was obtained using the X-ray diffraction (XRD). The XRD pattern of the selected samples was collected using a Denchtop X-Ray Diffractometer RIGAKU, model MiniFlex II using Cu X-ray tube (30 KV/15 mA). The data was collected at 2θ angles (10 – 80°); with a step speed of 3.5°/min. Debye–Scherrer equation was used to determine the crystallite size. The obtained X-ray scans were compared to those of standard database and the phases were assigned comparing with data available in literature.

2.2.5 UVCON – Accelerated aging tests

Accelerated aging tests are a fast approach to evaluate the durability of paints when exposed to sunlight and humidity. These accelerated aging tests were performed according to standard ISO 11507:2011 with UVA-340 lamps (QUV-A test). A typical accelerated aging test performed in the paint industry is UVCON. This test aims to evaluate the paint film degradation caused by exposure to sunlight and water condensation. It is important to mention that there is no direct correlation between the UVCON results and the real behavior of paints under outdoor conditions, though it gives useful information about the kind of damages that often can occur. These damages are mainly color change, gloss loss, chalking and cracking.

2.3 Results and Discussion

2.3.1 Photocatalytic paint films

The photocatalytic activity for NO abatement was obtained for the four prepared paints, applied in aluminum slabs of 10 × 5 cm^2. The correspondent results are shown in Figure 2.5.

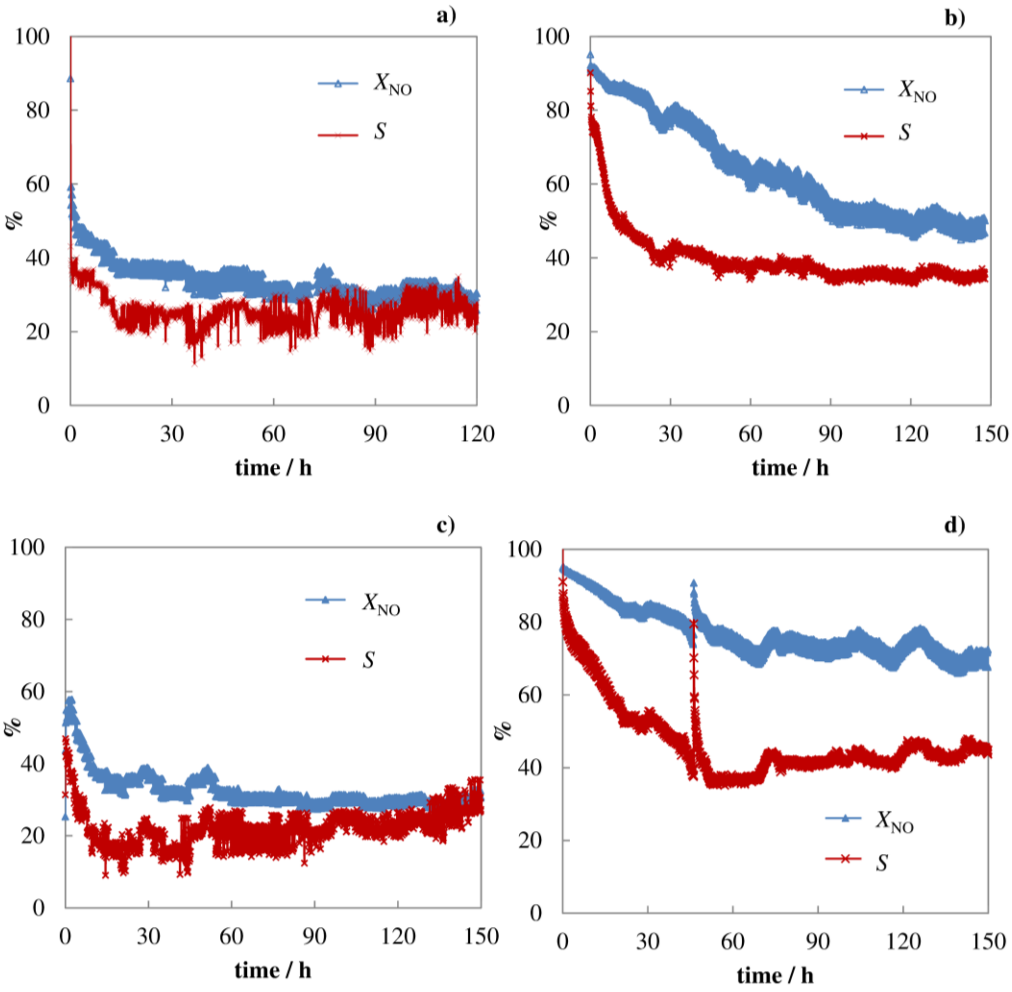

Figure 2.5. NO conversion (X_{NO}) and selectivity (S) histories for paints #1(a), #2 (b), paints #3(c) and #4 (d). Photocatalytic tests were performed at a feed rate of 0.7 $L_N \cdot min^{-1}$ of NO at 1 ppm_v in air and 50 % of relative humidity, at 25 °C with an irradiance of 10 $W \cdot m^{-2}$.

Calcium carbonate was selected as extender to be integrated in these formulations because it is a cheap material usually used in commercial paint formulations; it is more transparent to the UV light than the pigmentary TiO_2 and reacts with nitrate compounds, producing calcium nitrates that are easily washed off from the paint surface. Indeed, the NO conversion is favored since calcium carbonate assists the removal of nitrates from the photocatalyst surface, which are products of the NO photooxidation.

Analyzing Figure 2.5, it is possible to conclude that Paint #3 with 50 % of pigmentary TiO_2 and 50 % of PC500 shows better performance at steady-state conditions (conversion of 30 % and selectivity of 30 %) than Paint #1, which incorporates P25 instead of PC500 (conversion of 25 % and selectivity of 25 %). These results are in agreement with the ones obtained for compressed powder films reported in a previous work [21]. Moreover, a higher photocatalytic activity of paints incorporating PC500 was already expected because the surface area of PC500 photocatalyst is six times higher than P25. Paints #2 and #4, formulated without pigmentary TiO_2, showed a significantly higher photoactivity; in particular Paint #4, loaded with PC500, showed the highest performance (conversion of 70 % and selectivity of 45 %), followed by Paint #2 loaded with P25 (conversion of 50 % and selectivity of 35 %). In fact, Paint #4 presented a very interesting photocatalytic activity, comparable to the photoactivity of the corresponding compressed power film, reported elsewhere [21].

For comparison purposes, two commercial photocatalytic paints, Fotodecor and Fotosilox (from company Global Engineering acquired on 2010), were also tested under the same conditions and no significant conversion was observed – Figure 2.6.

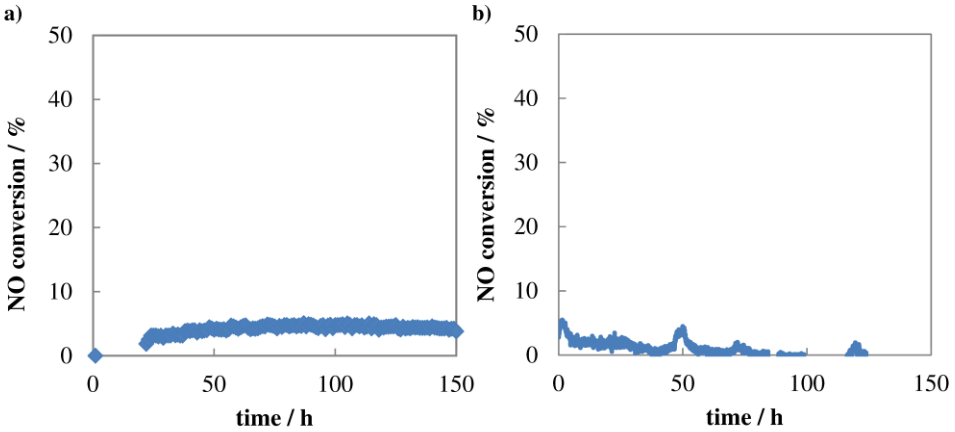

Figure 2.6. NO conversion for Fotodecor (a) and Fotosilox (b), commercial paints (Global Engineering). Photocatalytic tests were performed at a feed rate of 0.7 $L_N{\cdot}min^{-1}$ of NO at 1 ppm_v in air and 50 % of relative humidity, at 25 °C with an irradiance of 10 $W{\cdot}m^{-2}$.

The reference paint (RP) and the four formulated paints were tested in the outdoor experimental setup – Figure 2.3 – and the correspondent NO conversion was evaluated. Outdoor experiments lasted about 5 h. First, NO feeding concentration (with a NO feed of about 100 ppb_v and with no paint sample) was obtained for 2 hours. Then, the paint sample was placed in the setup and tested during 3 hours; at the end, the paint sample was removed and the NO concentration obtained for more *ca.* 60 min. This allowed to check the stability of the NO analyzer. The outdoor photoreactor was placed in Porto city (41° 11' N, 8° 36' W) and run on February and March of 2013. The NO content in the ambient air was observed to vary significantly with the time, making it difficult to compare the performances of the tested samples. A stable NO feed stream was then fed to the photoreactor (NO concentration was 100 ± 20 ppb_v). As expected, the reference paint exhibited no photoactivity (Figure 2.7). The histories of NO concentration during the three stages of the photocatalytic experiments are shown in Figure 2.8: i) the feeding concentration (NO_in); ii) venting concentration when the paint sample was in place (NO_out during 200 minutes); and iii) venting out concentration after removing the paint sample (NO_out during *ca.* 60 minutes). The vertical red line in Figure 2.8 marks the moment when the sample is removed. The results for NO conversion for the four paints are plotted in Figure 2.9.

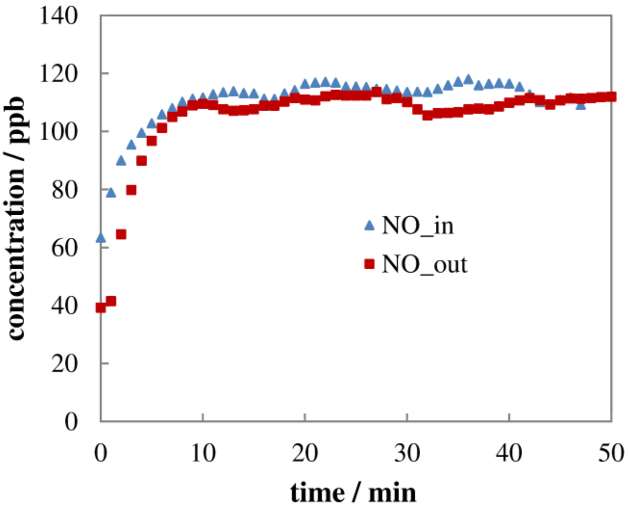

Figure 2.7. Feeding in NO concentration (NO_in) and venting out NO concentration (NO_out) history for the reference paint (RP).

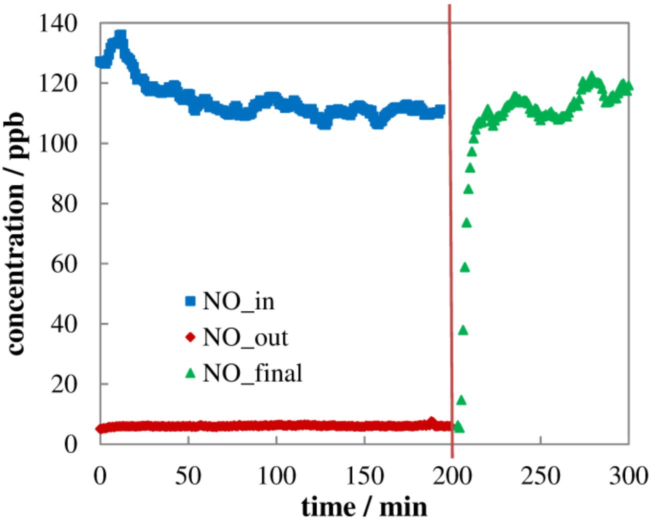

Figure 2.8. NO concentration histories for the reference paint sample: NO_in feed in concentration; NO_out venting out concentration with paint sample; NO_final venting out concentration without paint sample. The vertical line marks the end of the experiment with the paint sample.

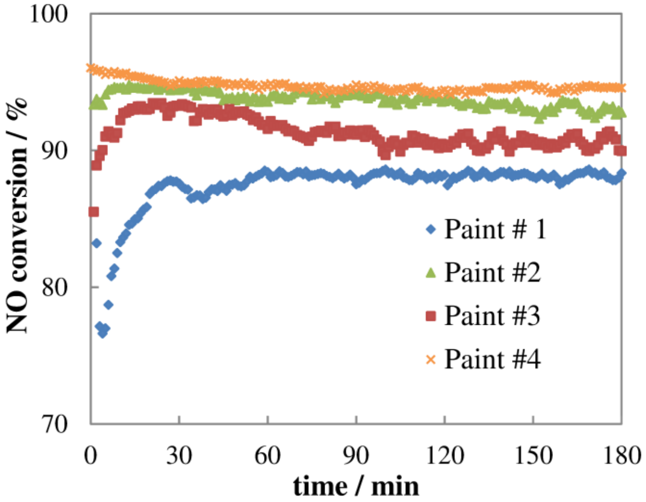

Figure 2.9. NO conversion for the four tested paints.

All the tested paints showed very good NO conversions, higher than 80 %. As for the lab results, the performance of the paint samples are from the best to the worst as follows: paints #4, #2, #3 and #1, even though the differences are not as notorious as for the lab results. Paint #4 showed a very high and stable NO conversion (*ca.* 95 % of conversion). The outdoor test unit has an average residence time of *ca.* 14 min, significantly higher than the residence time for the lab unit, 2.1 s, justifying the differences in conversion observed.

2.3.2 Diffuse reflectance analyses

The diffuse reflectance was obtained for photocatalysts P25 and PC500, Figure 2.10, and the band gap was obtained following the methodology described elsewhere [24]. In the case of P25, which has in its constitution both anatase and rutile [25], two inflection points were obtained and then two band gap values were computed – Table 2.3. These results are consistent with band gap values described in literature for anatase and rutile [26].

Table 2.3. Band gap energy of photocatalysts P25 and PC500.

Samples	**Band Gap Energy / eV**
P25	3.16 / 3.03
PC500	3.21

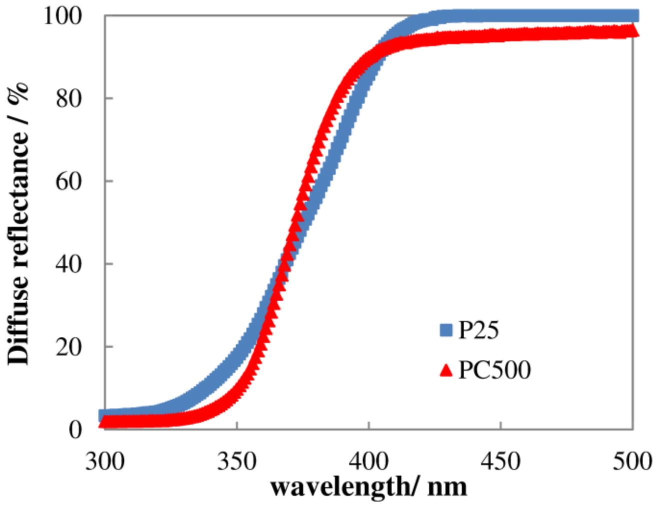

Figure 2.10. Diffuse reflectance of photocatalysts P25 and PC500.

2.3.3 *SEM and XRD analyses*

The SEM micrographs of powder catalysts (P25 and PC500) are in agreement with manufacturer's information (Figures 2.11 and 2.12), showing the primary particles of P25 with 20 – 30 nm particle-size and the presence of large agglomerates in the case of PC500.

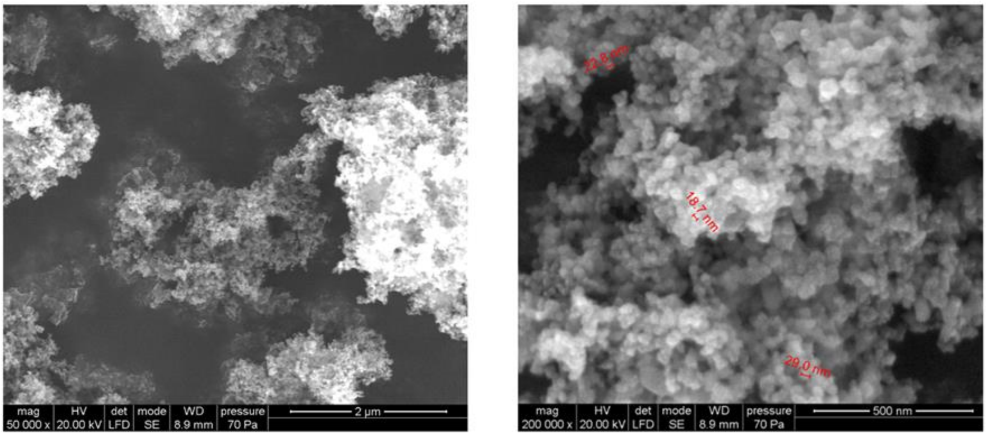

Figure 2.11. SEM micrographs of P25 (powder form) at magnifications of 50 000x and 200 000x.

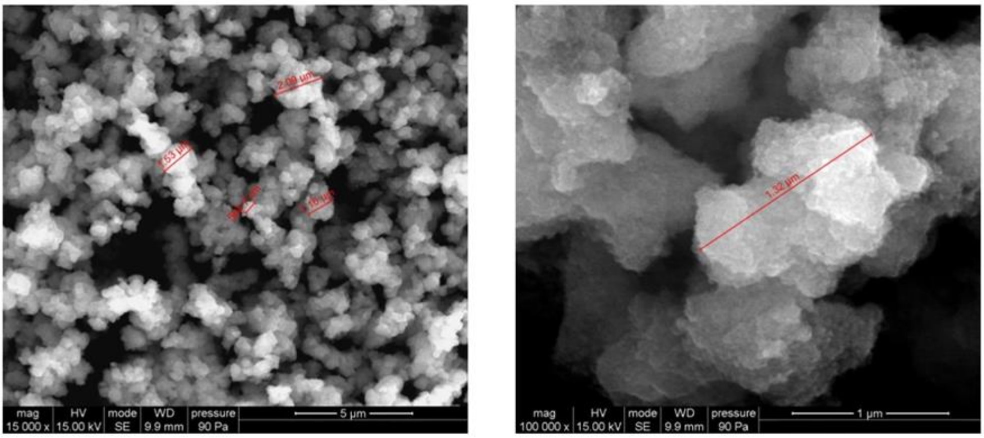

Figure 2.12. SEM micrographs of PC500 (powder form) at magnifications of 15 000x and 100 000x.

The commercial paint was also analyzed – Figure 2.13(a) – and smooth round hollow spheres were found, corresponding to a polymer extender used in this paint. Figures 2.13(b) and (c) show the morphology of photocatalytic paints #1 and #3. Photocatalyst and paint components are easily distinguished and it is visible that the photocatalyst is dispersed in the paint matrix. The photocatalytic paint with P25 seems to exhibit a better dispersion than paint with PC500 photocatalyst. However, the paint photocatalytic activity seems to be favored by a worse dispersion since more photocatalyst particles are uncoated with the polymer binder and then "free" to react with pollutants. Deeper deagglomerated P25 photocatalyst particles (higher dispersion) make the photocatalyst to contact more extensively with the paint binder and then to competitive degradation of the paint binder and the pollutants. Indeed, UVCON tests of paints with deeper deagglomerated P25 originate more intense chalking [21]. The SEM micrographs of photocatalytic paints with calcium carbonate extender substituting pigmentary TiO_2 are presented in Figures 2.14 to 2.16.

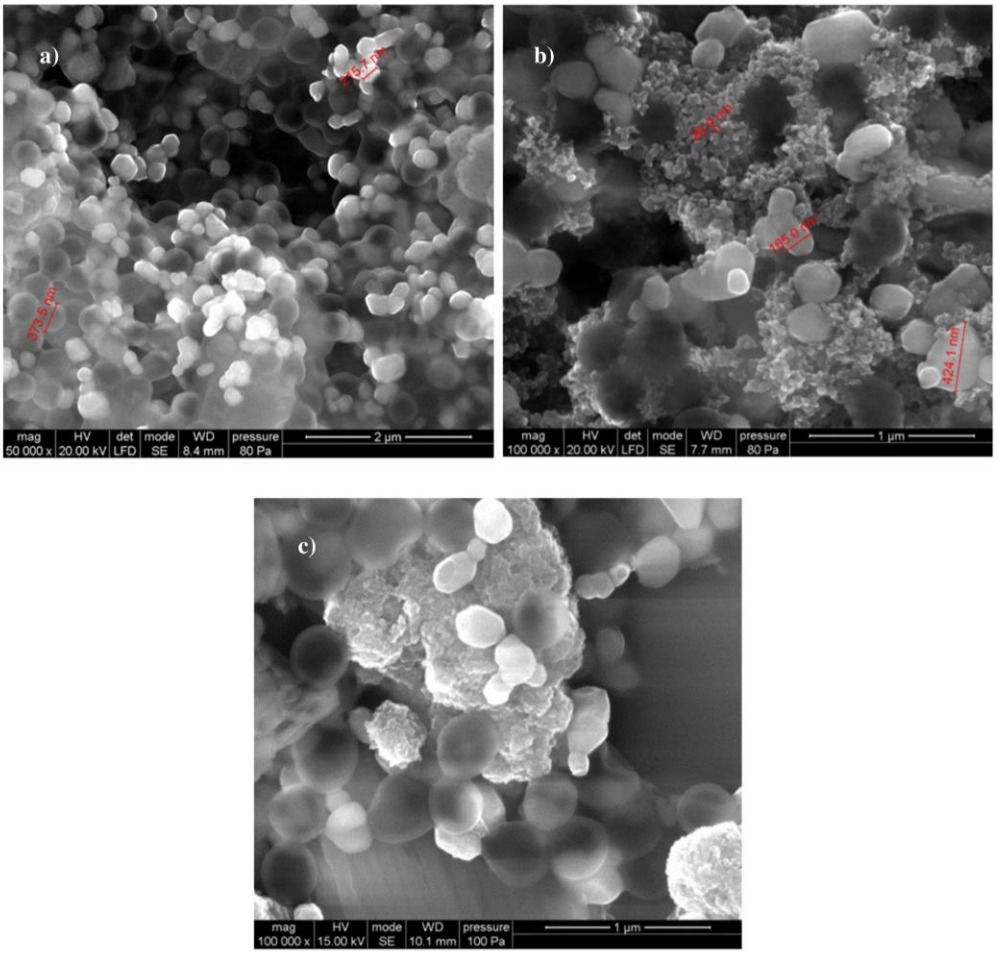

Figure 2.13. SEM micrographs of: (a) commercial paint; (b) Paint#1; and (c) Paint#3.

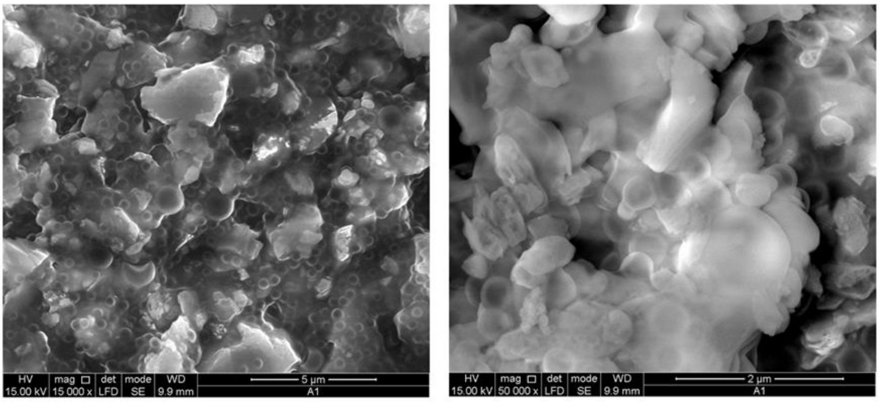

Figure 2.14. SEM micrographs of Reference Paint 2 (18 wt.% Calcium carbonate) at magnifications of 15 000x and 50 000x.

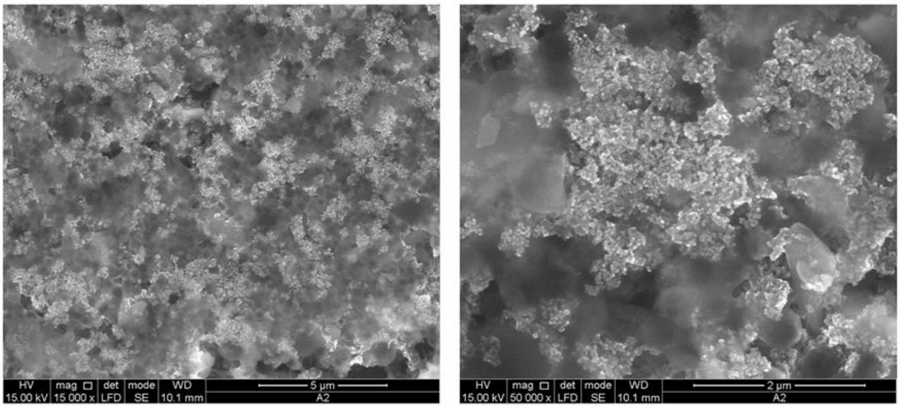

Figure 2.15. SEM micrographs of Paint#2 (9 wt.% $CaCO_3$ and 9 wt.% P25) at magnifications of 15 000x and 50 000x.

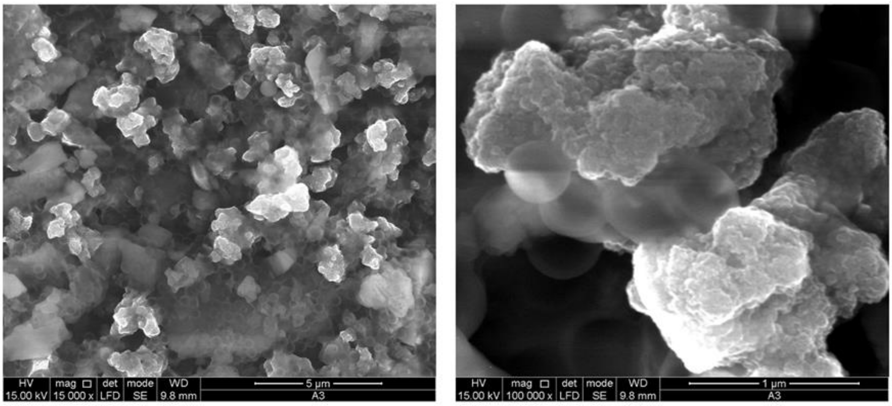

Figure 2.16. SEM micrographs of Paint#4 (9 wt.% $CaCO_3$ and 9 wt.% PC500) at magnifications of 15 000x and 100 000x.

The X-ray diffraction (XRD) patterns of titanium dioxide powders (Figure 2.17) show that P25 is composed of both rutile and anatase phases, whereas PC500 is only composed by anatase phase as indicated by manufactures. P25 presents crystallites-sizes of 19 nm (anatase) and 26 nm (rutile). In the case of PC500, crystallites of 12 nm-sizes (anatase) are found. Several authors studied the influence of crystallite size on photocatalytic performance of titanium dioxide for different photocatalytic reactions, claiming that ideal crystalline size is between 7-15 nm [27-29]. Smaller size crystallites lead to larger surface areas, improving pollutants adsorption and thus allowing better photocatalytic performance [30, 31]. Since PC500 photocatalyst particles are smaller, a higher photocatalytic activity of this photocatalyst was expected, which is actually in agreement with the experimental results.

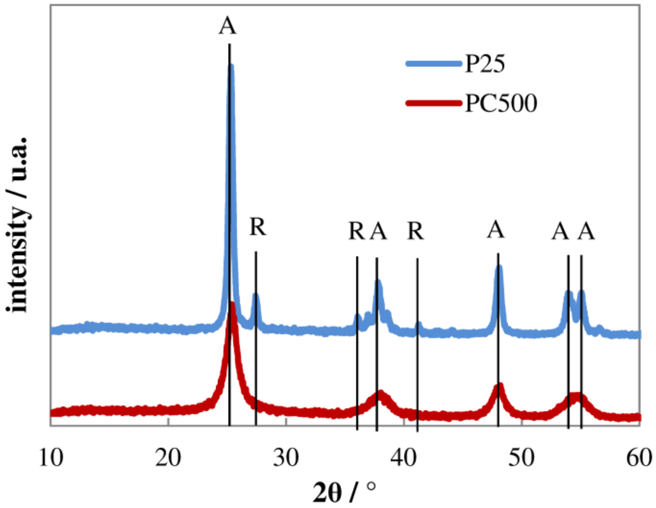

Figure 2.17. XRD patterns for commercial titanium dioxide, P25 and PC500 photocatalysts. The peaks corresponding to anatase and rutile phases are labelled by A and R, respectively.

XRD patterns of photocatalytic paints under study are also presented in Figure 2.18. Paints #1 and #3, containing 9 wt.% of pigmentary TiO_2 and 9 wt.% of photocatalytic TiO_2, were compared with a reference paint formulated with 18 wt.% of pigmentary TiO_2 (RP1); paints #2 and #4, which include calcium carbonate extender for substituting the pigmentary TiO_2, were compared with a reference paint formulated with 18 wt.% of $CaCO_3$ (RP2). As expected, peaks corresponding to the calcium carbonate response are observed in all pattern, being more intense for paints #2 and #4 since all the pigmentary TiO_2 was replaced by $CaCO_3$ extender. In case of paints #1 and #3, the main peak corresponding to TiO_2 rutile phase (27.5° and (110) facet) is higher due to the presence of pigmentary titanium dioxide (mainly rutile form).

Comparing the XRD patterns of the formulated paints with the reference paints without photocatalyst, it can be concluded that the addition of photocatalysts (P25 and PC500) does not lead to the crystalline properties change of these materials. Modifications in the crystal lattice are only observed when photocatalysts are added to the paints and the presence of the new peaks corresponding to titanium dioxide anatase for PC500 photocatalyst and anatase and rutile for P25 photocatalyst are distinguished.

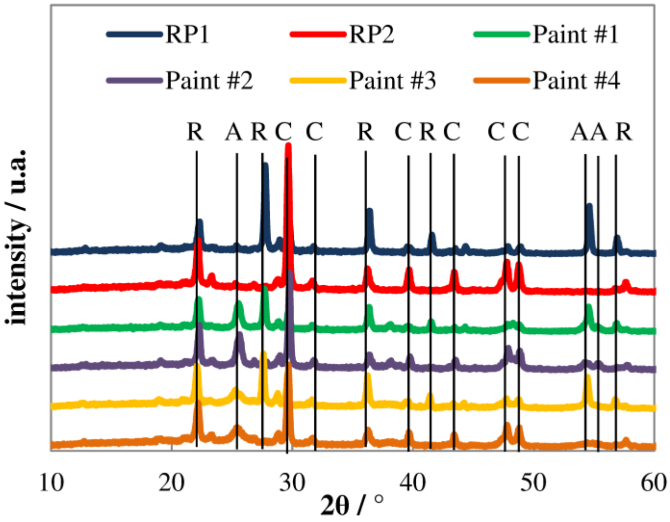

Figure 2.18. XRD patterns for paints #1 to #4 and respectively reference paints (RP1 and RP2). The peaks corresponding to anatase and rutile phases are labelled by A and R, respectively. The peaks of calcium carbonate are labelled by C.

2.3.4 UVCON tests

According to QUV-A results, paints #3 and #4 presented the highest resistance to degradation. The values (scale of 0-5, being 0 a surface without chalk) of the chalking test of paints #1 to #4 are given in Table 2.4. A commercial exterior water-based paint (vinyl paint) was also analyzed for comparison purposes. Chalking is the formation of fine chalky powder on the surface of the paint, which usually indicates binder degradation. Two other parameters can be obtained from the UVCON test: cracking and color changes; the prepared paints did not exhibit crack formation nor color change. The results obtained indicate that the best performing photocatalytic paints (Paint #3 and Paint #4) still show some chalking effect. Besides presenting very good photocatalytic activity these paints still have to be improved concerning chalking. This can be done by changing the binder for a more resistant one towards photocatalytic oxidation.

Table 2.4. Chalking values of UVCON test.

Paint \ Test duration	170 h	362 h	532 h	702 h	848 h	1060 h
Reference paint (without photocatalyst)	0	0	0	0	0	0
Paint #1	4	4/5	4/5	4/5	4/5	5
Paint #2	4	5	5	5	5	5
Paint #3	1	3	3	3	3	3
Paint #4	2	4	4	4	4	4

2.4 Conclusions

In the present study a commercial water-based paint was reformulated to host a photocatalyst; P25 from Evonik and PC500 from Cristal were chosen. Half of the pigmentary TiO_2 of the original paint was replaced by a photocatalytic TiO_2 and the remained pigmentary TiO_2 was either kept or replaced by calcium carbonate extender. Photocatalytic activity of these four paints was assessed according to the standard ISO 22197-1:2007. Comparing the best performing paints (Paints #2 and #4), it can be concluded that both do not incorporate pigmentary TiO_2; indeed this component blocks the light harvesting, decreasing the photocatalytic activity. Moreover, PC500-based paint (Paint #4) originates better NO conversions than P25-based paint (Paint #2), 70 % and 50 %, respectively, as well as it also originates better selectivities, 45 % and 35 %, respectively. This behavior was further studied based on SEM and XRD analyses. PC500 exhibits smaller TiO_2 particles compared with P25, which in principle favors the photoactivity of PC500. Moreover, the addition of photocatalysts to a paint does not introduce any changes in the original crystal lattice. Under outdoor tests, all paints showed a NO conversion higher than 80 %. The best performing paint was again Paint #4 (with PC500 and calcium carbonate), presenting a NO conversion of about 95 %. This validates the result obtained under lab-scale characterization.

Despite displaying some chalking, the exceptional high photocatalytic activity of Paint #4 is ascribed to several factors: paint PVC/CPVC ratio higher than one; high paint film thickness; complete removal of the pigmentary TiO_2 and use of a very active photocatalyst, PC500. Paint coatings are one of the best approaches to immobilize photo-TiO_2 since they create a 3D layer where TiO_2 nanoparticles are available for photocatalysis up to the optic thickness, which is around 100 μm. Actually, the prepared paints are an example of this.

Acknowledgements

This work is co-founded by FEDER (Fundo Europeu de Desenvolvimento Regional)/QREN (NOxOut project with reference FCOMP 01-0102- FEDER 005365) under the framework of “Programa Operacional Factor de Competitividade”. The authors also acknowledge financing from FCT through the project PTDC/EQU-EQU/115614/2009. Joana Ângelo is grateful to the Portuguese Foundation for Science and Technology (FCT) for her PhD Grant (Reference: SFRH/BD/79974/2011). Luísa Andrade acknowledges European Research Council for funding within project BI-DSC – Building Integrated Dye sensitized Solar Cells (Contract Number: 321315) and FCT-CAPES cooperation 2013-2014. The authors would like to acknowledge Dr. Cecilia Mateos Pedrero for the fruitful discussions about XRD analyzes.

References

1. Fujishima, A., Rao, T.N., and Tryk, D.A., *Titanium dioxide photocatalysis.* Journal of Photochemistry and Photobiology, C: Photochemistry Reviews, 1(1): p. 1-21, **2000**
2. Devahasdin, S., Fan Jr, C., Li, K., and Chen, D.H., *TiO_2 photocatalytic oxidation of nitric oxide: transient behavior and reaction kinetics.* Journal of Photochemistry and Photobiology, A: Chemistry, 156(1–3): p. 161-170, **2003**
3. Paz, Y., *Application of TiO_2 photocatalysis for air treatment: Patents' overview.* Applied Catalysis, B: Environmental, 99(3–4): p. 448-460, **2010**
4. Masakazu, A., *Utilization of TiO_2 photocatalysts in green chemistry.* Pure and applied chemistry, 72: p. 1265-1270, **2000**
5. Chen, J. and Poon, C.S., *Photocatalytic construction and building materials: From fundamentals to applications.* Building and Environment, 44(9): p. 1899-1906, **2009**
6. Chen, J., Kou, S.C., and Poon, C.S., *Photocatalytic cement-based materials: Comparison of nitrogen oxides and toluene removal potentials and evaluation of self-cleaning performance.* Building and Environment, 46(9): p. 1827-1833, **2011**
7. Folli, A., Pade, C., Hansen, T.B., De Marco, T., and Macphee, D.E., *TiO_2 photocatalysis in cementitious systems: Insights into self-cleaning and depollution chemistry.* Cement and Concrete Research, 42(3): p. 539-548, **2012**
8. Osburn, L., *Literature review on the application of titanium dioxide reactive surfaces on urban infrastructure for depolluting and self-cleaning applications.* 5th Post Graduate Conference on Construction Industry Development, Bloemfontein, South Africa, 16-18 March 2008: p. 11, **2008**
9. Lee, B.Y., Jayapalan, A.R., Bergin, M.H., and Kurtis, K.E., *Photocatalytic cement exposed to nitrogen oxides: Effect of oxidation and binding.* Cement and Concrete Research, 60(0): p. 30-36, **2014**
10. Tryba, B., Homa, P., Wróbel, R.J., and Morawski, A.W., *Photocatalytic decomposition of benzo-[a]-pyrene on the surface of acrylic, latex and mineral paints. Influence of paint composition.* Journal of Photochemistry and Photobiology A: Chemistry, 286(0): p. 10-15, **2014**

11. Italcementi, *TX Active The Photocatalytic Active Principle*, in *Tecnical Report*: Bergamo, Italy, **2009**.
12. Maggos, T., Plassais, A., Bartzis, J.G., Vasilakos, C., Moussiopoulos, N., and Bonafous, L., *Photocatalytic degradation of NO_x in a pilot street canyon configuration using TiO_2-mortar panels.* Environmental Monitoring and Assessment, 136(1-3): p. 35-44, **2008**
13. Guerrini, G.L., *Photocatalytic performances in a city tunnel in Rome: NO_x monitoring results.* Construction and Building Materials, 27(1): p. 165-175, **2012**
14. Maggos, T., Bartzis, J.G., Liakou, M., and Gobin, C., *Photocatalytic degradation of NO_x gases using TiO_2-containing paint: A real scale study.* Journal of Hazardous Materials, 146(3): p. 668-673, **2007**
15. Claire E. Bygott, Julie E. Maltby, John L. Stratton, and McIntyre, R., *Photocatalytic coatings for the construction industry*, in *International RILEM Symposium on Photocatalysis, Environment and Construction Materials* P.B.a.L. Casssar, Editor RILEM Publications SARL: Florence, Italy. p. 251 - 258. **2007**.
16. Allen, N.S., Edge, M., Verran, J., Stratton, J., Maltby, J., and Bygott, C., *Photocatalytic titania based surfaces: Environmental benefits.* Polymer Degradation and Stability, 93(9): p. 1632-1646, **2008**
17. Boysen, Available from: http://www.knoxoutpaints.com/; [accessed **November 2015**].
18. EDSA, B.P., Available from: http://boysenknoxoutproject.com/; [accessed **November 2015**].
19. Light2cat, Available from: http://www.light2cat.eu/; [accessed **November 2015**].
20. Suárez, S., Portela, R., Hernández-Alonso, M.D., and Sánchez, B., *Development of a versatile experimental setup for the evaluation of the photocatalytic properties of construction materials under realistic outdoor conditions.* Environmental Science and Pollution Research International, **2014**
21. Águia, C., Ângelo, J., Madeira, L.M., and Mendes, A., *Photo-oxidation of NO using an exterior paint - Screening of various commercial titania in powder pressed and paint films.* Journal of Environmental Management, 92(7): p. 1724-1732, **2011**

22. Águia, C., Ângelo, J., Madeira, L.M., and Mendes, A., *Influence of photocatalytic paint components on the photoactivity of P25 towards NO abatement.* Catalysis Today, 151(1–2): p. 77-83, **2010**
23. Boldish, S.I. and White, W.B., *Optical band gaps of selected ternary sulfide minerals.* American Mineralogist, 83: p. 865-871, **1998**
24. Murphy, A.B., *Band-gap determination from diffuse reflectance measurements of semicondutor films, and application to photoelectochemical water-splitting.* Solar Energy Materials and Solar Cells, 91: p. 1326-1337, **2007**
25. Ohtani, B., Prieto-Mahaney, O.O., Li, D., and Abe, R., *What is Degussa (Evonik) P25? Crystalline composition analysis, reconstruction from isolated pure particles and photocatalytic activity test.* Journal of Photochemistry and Photobiology, A: Chemistry, 216(2–3): p. 179-182, **2010**
26. Pleskov, Y.V., *Encyclopedia of Electrochemistry, Bard, A.J. and Stratmann, M., Eds., vol. 6, Semiconductor Electrodes and Photoelectrochemistry, Licht, S., Ed., Weinheim: Wiley–VCH, 2002.* Russian Journal of Electrochemistry (Translation of Elektrokhimiya), 39(3): p. 328-330, **2003**
27. Liu, S., Jaffrezic, N., and Guillard, C., *Size effects in liquid-phase photo-oxidation of phenol using nanometer-sized TiO_2 catalysts.* Applied Surface Science, 255(5, Part 2): p. 2704-2709, **2008**
28. Zhang, Q., Gao, L., and Guo, J., *Effects of calcination on the photocatalytic properties of nanosized TiO_2 powders prepared by $TiCl_4$ hydrolysis.* Applied Catalysis B: Environmental, 26(3): p. 207-215, **2000**
29. Maira, A.J., Yeung, K.L., Lee, C.Y., Yue, P.L., and Chan, C.K., *Size Effects in Gas-Phase Photo-oxidation of Trichloroethylene Using Nanometer-Sized TiO_2 Catalysts.* Journal of Catalysis, 192(1): p. 185-196, **2000**
30. Xie, M., Jing, L., Zhou, J., Lin, J., and Fu, H., *Synthesis of nanocrystalline anatase TiO_2 by one-pot two-phase separated hydrolysis-solvothermal processes and its high activity for photocatalytic degradation of rhodamine B.* Journal of Hazardous Materials, 176(1–3): p. 139-145, **2010**
31. Jiu, J., Wang, F., and Adachi, M., *Preparation of highly photocatalytic active nano-scale TiO_2 by mixed template method.* Materials Letters, 58(30): p. 3915-3919, **2004**

PART II: Chapter 3

Characterization of TiO_2-based semiconductors for photocatalysis by electrochemical impedance spectroscopy

Chapter 3.

Characterization of TiO_2-based semiconductors for photocatalysis by electrochemical impedance spectroscopy

Joana Ângelo, Pedro Magalhães, Luísa Andrade and Adélio Mendes

(*Applied Surface Science 2016, 387, 183–189*)

Abstract

The photocatalytic activity of a commercial titanium dioxide (P25) and of an in-house prepared P25/graphene composite is assessed according to standard ISO 22197-1:2007. The photoactivity performances of bare and composite TiO_2-based materials was further studied by electrochemical impedance spectroscopy (EIS) technique to better understand the function of the graphene in the composite. EIS experiments were performed using a three-electrode configuration, which allows obtaining more detailed information about the complex charge transfer phenomena at the semiconductor/electrolyte interface. The Randles equivalent circuit was selected as the most suitable for modelling the present photocatalysts. The use of the graphene composite allows a more effective charge separation with lower charge transfer resistance and less e-/h+ recombination on the composite photocatalyst, reflected in the higher values of NO conversion.

Keywords: Photoelectrochemical; Photocatalysis; Titanium dioxide; Pollutants degradation.

3.1 Introduction

Photocatalysis is a photoelectrochemical process where a semiconductor, normally in the form of nanoparticles, uses the adsorbed water as electrolyte and the sun or artificial light to degrade pollutants or for inactivating microorganisms [1]. Common semiconductors considered for photocatalysis are TiO2, ZnO, Fe2O3, CdS and ZnS [2]. In a photocatalytic process, as the semiconductor absorbs light, electrons from the valence band are injected to the conduction band, creating electron-hole pairs. Then, those electrons and holes move to the particle surface and react with water to form $OH^{\bullet}$ and $O_2^{\bullet-}$ radicals, enabling the oxidation of pollutants at the semiconductor surface. However, if electron-hole recombination occurs, the photocatalytic efficiency decreases. This recombination pathway is well-known as a key limitation for photocatalytic processes so several studies are being conducted to minimize it [3-6].

TiO_2 and TiO_2-based semiconductors, namely TiO_2/graphene composites, are promising candidates for degrading pollutants. Titanium dioxide is the most common photocatalyst used because it is cheap, nontoxic, thermally stable and chemically inert [3, 7, 8]. On the other hand, graphene presents unique and excellent electronic, thermal and mechanical properties. Graphene platelets have a large specific surface area (*ca.* 2600 $m^2 \cdot g^{-1}$), a high transparency, an excellent electron mobility and it can be optimized by chemical modification; which is an important advantage to be used in a composite material [9-13]. Therefore, several photocatalytic studies consider composite semiconductors of TiO_2/graphene for the degradation of pollutants [9, 14-17] since they exhibit higher photocatalytic activity than bare titanium dioxide. This enhanced photoactivity verified on the supported titanium dioxide on graphene platelets was ascribed to a smaller band gap, allowing the harvesting of a broader solar energy, and to better charge separation properties (less recombination) [9, 12]. The graphene layer, at the titanium dioxide/graphene composite, has also the advantage to provide a support for adsorbing the reactants [9], avoiding the spread of too small titanium dioxide nanoparticles in the environment, which was proved to be harmful [14].

Despite the great interest of the TiO_2/graphene photocatalysts, the function of the graphene in the composite is not fully understood and several arguments are suggested with no direct experimental evidences. Since the photocatalytic activity is limited by the charge transport kinetics on the semiconductor and by the redox reactions occurring at its surface, a deeper understanding of these phenomena is essential. Electrochemical impedance spectroscopy (EIS) is a useful technique to study the electrical behavior of photocatalytic systems and particularly to evaluate phenomena occurring at the semiconductor/electrolyte interface. In an EIS experiment, a small potential sinusoidal perturbation is applied to the system and the amplitude and phase shift of the resulting current response are recorded. EIS technique is easy to use but, sometimes, difficult to interpret, requiring the use of models based on electrical analogues. In particular, fitting the experimental data to specific arrangements of electrical elements, which may consist of resistors, capacitors, inductors and more complex elements, assembled in series or in parallel, can provide relevant information concerning reaction kinetics, charge transfer and even mass transfer phenomena occurring in photocatalytic systems. Actually, EIS technique is widely used in the study of photoelectrochemical and electrochemical systems since it allows discriminating the different phenomena proceeding at a different rate, such as series resistances; transport resistances; electron-hole recombination and consequently electron lifetime [18].

The present work reports the photocatalytic activity of two semiconductors for NO deep oxidation. The band gap of the semiconductors was obtained and the photoelectrochemical characterization was performed based on two techniques: current-potential characteristic curves and electrochemical impedance spectroscopy. Even though several works have reported the use of electrochemical impedance spectroscopy, applied to photocatalysts [9, 19-23], the main goal of this work is to use EIS technique to discriminate the charge transfer processes in the semiconductor/electrolyte interface and thus contribute for the interpretation of the graphene role in photocatalysts composites. Moreover, it is also envisaged the characterization of photocatalysts in the dark by EIS.

3.2 Experimental

3.2.1 Photocatalysts Materials

Photocatalyst Aeroxide® P25 (Evonik Industries, Germany) and an in-house prepared P25/graphene composite were studied. P25/graphene composite was prepared based on the hydrothermal method proposed by Zhang and co-workers [9]. Graphene nano-platelets (xGnP®from XG Sciences) were oxidized with an aqueous solution of $KMnO_4$

and H_2SO_4 to obtain graphene oxide (GO) - modified Hummer's method [24]. The detailed description of the P25/graphene composite preparation is given elsewhere [25].

3.2.2 Photocatalytic Characterization

The photocatalytic activity of the photocatalysts was achieved using an experimental setup based on standard ISO 22197-1:2007. The internal dimensions of photoreactor are 0.05 m x 0.23 m x 0.005 m (width x length x height). UV lamp system (Vilbert Lourmat – BLB 365 nm, 2 x 6 W) was placed over the reactor and a NO_x analyzer (Thermo electron 42C – chemiluminescence method) was used to measure the outlet concentrations. A detailed description of this setup is reported elsewhere [26].

The activity of the photocatalysts was assessed based on the NO conversion (Eq. 3.1) and selectivity to the formation of ionic species (Eq. 3.2):

$$X_{\mathrm{NO}} = \left(\frac{[\mathrm{NO}]_{\mathrm{in}} - [\mathrm{NO}]_{\mathrm{out}}}{[\mathrm{NO}]_{\mathrm{in}}} \right) \times 100 \qquad 3.1$$

$$S = \left(1 - \frac{[\mathrm{NO_2}]_{\mathrm{out}}}{[\mathrm{NO}]_{\mathrm{in}} - [\mathrm{NO}]_{\mathrm{out}}} \right) \times 100 \qquad 3.2$$

where X_{NO} is the conversion of NO, $[\mathrm{NO}]$ and $[\mathrm{NO_2}]$the concentration of NO and NO_2, respectively, and the superscripts (*in* and *out*) refer to the inlet and outlet of the photoreactor. The NO deep oxidation is required to form nitrate ($\mathrm{NO_3^-}$) and nitrite ($\mathrm{NO_2^-}$) species (the later formed in much less extend [27]) instead of nitrogen dioxide (NO_2), which is much more harmful than NO and easily formed in the presence of atmospheric oxygen. A detailed description of this characterization tool can be found elsewhere [28].

Photocatalytic tests were performed at a feed flowrate of 0.7 $\mathrm{L_N \cdot min^{-1}}$ containing 1 $\mathrm{ppm_v}$ of NO in air with 50 % of relative humidity. The photoreactor was inside a thermostatic cabinet at 25 °C and under UV light with an irradiance of 10 $\mathrm{W \cdot m^{-2}}$.

The band gap of the photocatalysts was obtained by diffuse reflectance spectroscopy using the Tauc equation as described elsewhere [26]. The modified Kubelka–Munk equation was plotted as a function of the incident radiation ($h\nu$ (eV)) and the band gap of the semiconductors obtained extrapolating the linear part of this curve to the *x*-axis;

the band gap energy was read at the intersection. The diffuse reflectance measurements were obtained in a Shimatzu UV-3600 UV-VIS-NIR spectrophotometer, equipped with a 150 mm integrating sphere and $BaSO_4$ was used as 100 % reflectance standard.

3.2.3 Photoelectrodes preparation

Photocatalysts were deposited on conducting fluorine doped tin oxide ($F:SnO_2$) glass substrates (TCO22-15, Solaronix, Switzerland) by spin coating. A suspension of photocatalyst (2 wt.%) in 9:1 mixture of water/ethanol were prepared and dispersed by ultrasounds during 80 min for breaking the photocatalyst agglomerates. The suspension was then spin coated on FTO glass substrates at 1500 rpm during 10 s; this process was repeated six times for each sample (six layers) and each layer was dried in a hot plate at 60 °C for 10 min. Finally, the samples were annealed in a blow drier during 30 min at 400 °C in the case of P25/graphene composite and at 550 °C in case of the P25. Thermogravimetric (TG) analyses were carried out for P25 and P25/graphene in air to measure the mass loss as a function of the temperature; it was determined that P25/graphene composite contained 1.0 wt.% of graphene.

The morphology and thickness of photoelectrodes were assessed by scanning electron microscopy technique analysis (FEI Quanta 400FEG ESEM/EDAX Genesis X4M apparatus equipped with a Schottky field emission gun). Thicknesses of the photoelectrodes were ca. 1.5 μm for P25 and 3 μm for P25/graphene composite.

3.2.4 Electrochemical Characterization

Electrochemical characterization was performed in a photoelectrochemical (PEC) cell known as “cappuccino” in a standard three-electrode configuration [29]. Prepared thin films (active area of ca. 0.238 cm^2) applied on the FTO coated substrates were used as working electrodes, 99.9 % platinum wire was used as counter-electrode (Alfa Aesar, Germany) and Ag/AgCl/ sat. KCl was used as reference electrode (Metrohm, Switzerland). The measurements were conducted using an aqueous solution of H_2SO_4 0.5 M as electrolyte (pH = 0.8).

The photocurrent density – potential (*J*–*V*) characterization was performed for the prepared thin films applying an external potential bias to the cell and measuring the generated photocurrent using a ZENNIUM workstation (Zahner Elektrik, Germany). These measurements were conducted in the dark and under UV illumination (30 $W\cdot m^2$,

$\lambda = 365$ nm) at a scan rate of 10 $mV \cdot s^{-1}$ for the potential range between 0.65 V_{RHE} and 1.65 V_{RHE}.

EIS measurements were performed with a ZENNIUM workstation under dark conditions, with a frequency range between 100 mHz and 100 kHz and the magnitude of the modulation signal was 10 mV. All the measurements were performed at room temperature at open-circuit potential. The experimental data were fitted to an equivalent electrical analogue using ZView® software.

3.3 Results and discussion

The photocatalytic activity for NO abatement was obtained for P25 and P25/graphene, as compressed powder films applied in aluminum slabs of 2 × 2 cm^2. The NO conversion and selectivity histories are shown in Figure 3.1. The photocatalysts were evaluated during 30 hours and a higher NO conversion and selectivity were obtained for the P25/graphene composite. The hydroxyl and superoxide radicals are responsible for NO photooxidation; these radical species are formed from the reaction of photogenerated electron and holes with oxygen and water, respectively. The higher NO conversion of P25/graphene was expected due to the ability of graphene to trap the photogenerated electrons from titanium dioxide, as suggested by several authors, improving the charge separation and decreasing e-/h+ recombination [30, 31]. However, no experimental evidences were ever reported for corroborating this fact, justifying the interest of the present work. On the other hand, NO photooxidation results in three main products: NO_2, NO_2^- and NO_3^-. NO_2 is more harmful than NO, so a higher selectivity to nitrate is desired for this process; considering that all the NO_2^- formed was consumed to produce NO_2 or HNO_3. A higher selectivity of P25/graphene composite to nitrates is expected since NO_2 is more absorbed on graphene. This interaction increases the probability of NO to be photooxidized to HNO_3 [32].

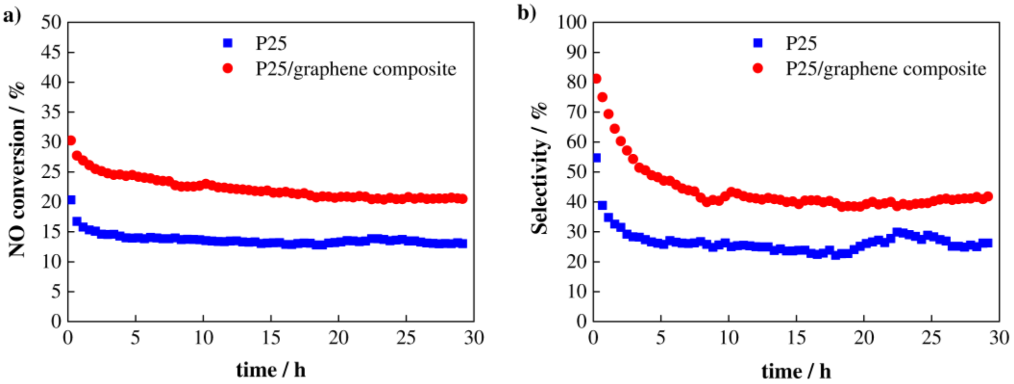

Figure 3.1. a) NO conversion and **b)** selectivity histories for P25 and for P25/graphene composite. Photocatalytic tests were performed at a feed rate of 0.7 $L_N \cdot min^{-1}$of NO at 1 ppm_v in air and 50 % of relative humidity, at 25 °C with an irradiance of 10 $W \cdot m^{-2}$.

Modified Kubelka–Munk function *versus* the incident irradiance is plotted in Figure 3.2 for P25 and P25/graphene composite photocatalysts. The band gap of P25 is 3.2 eV and the band gap of the composite photocatalyst is 2.9 eV; the determined band gap for P25 matches with the value reported in literature [33].

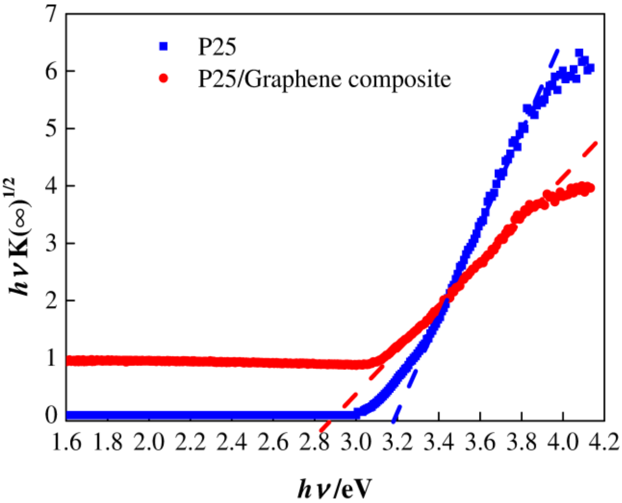

Figure 3.2. Modified Kubelka–Munk function *versus* incident irradiance for P25 and P25/graphene composite.

The composite photocatalyst exhibits a slightly lower band gap than P25, which means that it absorbs a wider range of wavelengths. The lower band gap of the composite can be explained by titanium dioxide doping by carbon from graphene, which can act as substitutional anion or an interstitial cation, substituting oxygen or titanium, respectively. The carbon doping of titanium dioxide leads then to a narrowing in band gap and a consequent red-shift in the absorption spectrum of the composite [25, 34]. The P25/graphene photocatalyst band gap is in good agreement with values reported for equivalent materials [15, 16, 35].

Figures 3.3 and 3.4 present SEM images of top view (a) and cross section (b) of P25 and P25/graphene composite photoelectrodes, respectively.

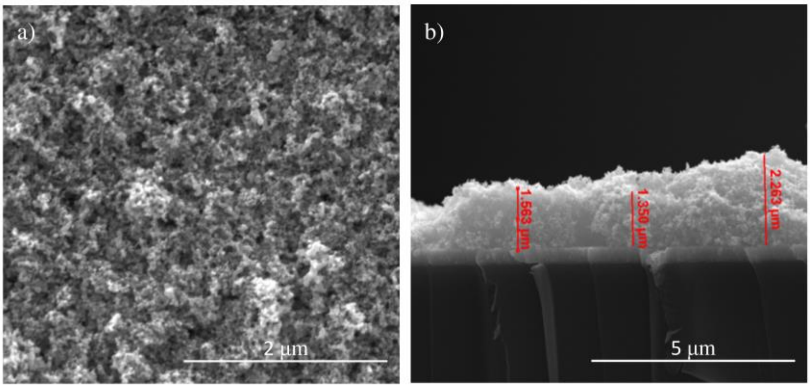

Figure 3.3. Top view (a) and cross-section (b) SEM images of P25 respectively at 50 000x and 20 000x magnifications.

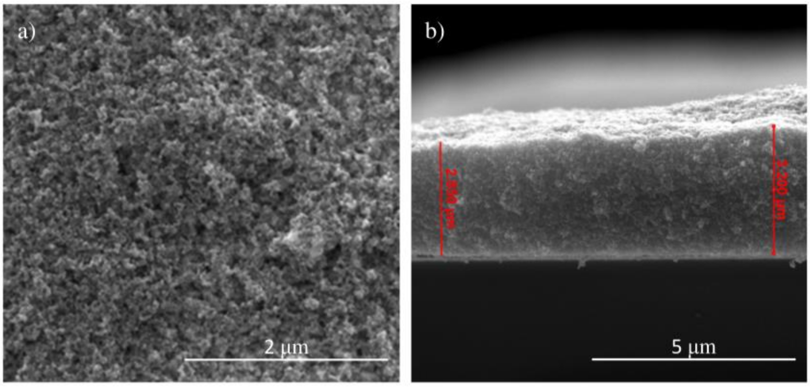

Figure 3.4. Top view (a) and cross-section (b) SEM images of P25/graphene composite respectively at magnifications 50 000x and 20 000x.

Analyzing the top view, it is not possible to recognize significant morphological differences between the two photocatalysts; both materials present high agglomeration of small primary particles. This morphology was reported by several authors for P25 photocatalyst; in the case of P25/graphene composite the same morphology was expected since a very small fraction of graphene is used. In what concerns the cross section images, the average thicknesses of photoelectrodes is ca. 1.5 μm for P25 and 3 μm for P25/graphene composite. On the other hand, it is possible to observe a more compact film for P25/graphene composite photoelectrode.

In a previous work [25], the crystallographic characterization of P25 and P25/graphene composite was performed by X-ray diffraction (XRD). These photocatalysts showed similar XDR patterns. In fact, the XRD pattern of P25/graphene composite did not show any diffraction peaks for carbon species, which it can be explained by the low diffraction intensity and low amount of graphene in the composite.

As mentioned before, several studies point out that the higher photoactivity of TiO_2/graphene composite can be assigned to its ability to absorb wider wavelengths, to a more effective separation of charges and to a more efficient transport of electrons compared with the bare semiconductor [9, 15-17]. However, the grounding of these conclusions was not completely discussed. This work applies specific techniques to analyze the charge transport and recombination on bare and graphene composite TiO_2 photocatalysts aiming at to conclude about the roots of the better photocatalysts performance.

First, the electrochemical performance of P25 and P25/graphene photocatalysts in a photoelectrochemical cell configuration were studied based on their characteristic curves (J–V) in the dark and under UV illumination (30 $W \cdot m^{-2}$, $\lambda = 365$ nm) – Figure 3.5.

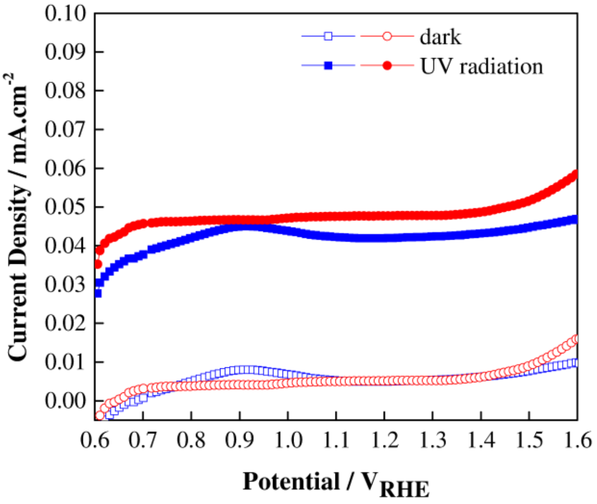

Figure 3.5. Photocurrent density-potential characteristics of P25 (blue) and P25/graphene composite (red) in the dark (-□- -○-) and under UV radiation (-■- -●-).

From Figure 3.5 it is possible to conclude that the P25/graphene composite shows under illumination a higher current density than P25 for the potential range studied. This higher current density was already expected due to its enhanced photocatalytic performance. In P25/graphene composite, the carbon support acts as an acceptor of electrons formed on titanium dioxide particles [9, 16]. Thus, considering the high electronic conductivity of graphene, the formed electrons are quickly removed from the particle surface, diminishing the surface recombination and ensuring an effective charge separation. At the graphene side, the excited electrons participate in reduction reactions and consequently more charge carriers are able to react and high photocurrents can be achieved allowing more efficient photocatalysis [9, 16, 17, 36].

Electrochemical impedance spectroscopy was used to characterize the thin film photoelectrodes of P25 and P25/graphene composite and further interpret the charge separation at the semiconductor/electrolyte interface. These measurements were performed using a three-electrode configuration in order to better study the electrochemical behavior of the semiconductor/electrolyte interface, which plays a very important role in the photocatalytic process since it dominates all reaction kinetics. Typical impedance spectra for the photocatalysts under study at 1.00 V_{RHE} are shown in Figure 3.6.

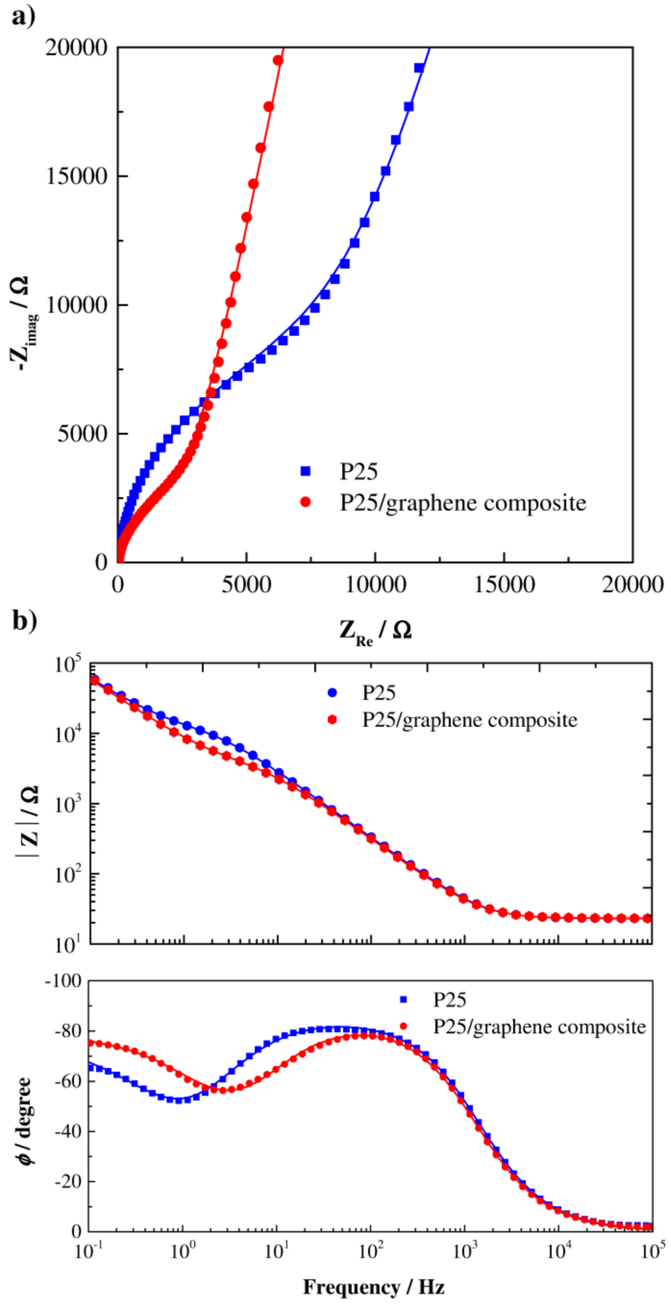

Figure 3.6. a) Nyquist diagram and **b)** Bode plots obtained in the dark at 1.00 V_{RHE} in a 3-electrode configuration. The solid lines represent the fittings based on the Randles circuit.

The Nyquist plot represents the opposite of the imaginary part of the complex impedance (-Z_{Imag}) as a function of the real part (Z_{Re}) for different values of frequency; the Bode diagram plots the magnitude impedance ($|Z|$) and the phase shift (Φ) as a function of frequency.

Electrical equivalent circuits are used to rationalize the charge-transfer and transport phenomena that take place in photoelectrochemical systems [37]. However, the interpretation of these phenomena in terms of resistive and capacitive elements is not straightforward due to the inherent complexity. The electron transport and charge separation in TiO_2 thin films have been widely studied [9, 22, 23] and several electrical analogues have been proposed. These electrical analogues were widely assessed within this work and a Randles circuit (Figure 3.7) was considered the most suitable for modelling the present photocatalysts. In particular, a transmission line model [18] and Roberts and Crowell model [20] were tested but with no success since they are especially applicable for porous structures of several micrometers.

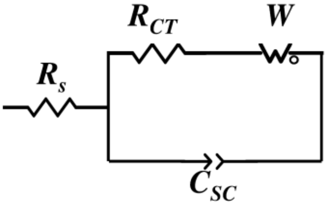

Figure 3.7. Randles circuit used to fit the impedance experimental data.

Moreover, in the Nyquist diagrams it is clearly noticed a “full” Randles equivalent circuit composed of two distinct contributions: i) the space-charge capacitance (C_{SC}) corresponding to the ability of storing charge in the double layer of the semiconductor/electrolyte interface; and ii) the faradaic process, represented as a series combination of the charge-transfer resistance (R_{CT}) at the same interface and a Warburg impedance (W) related to mass transfer (diffusion) resistance [38]. As excitation source frequency increases, the faradaic impedance approaches R_{CT} and so in the Nyquist diagram a semi-circle is observed (response to a parallel combination of C_{SC} and R_{CT}); for low-frequencies, the faradaic impedance can be viewed as a two resistances combined in series – one ascribed to electron-transfer in the semiconductor/electrolyte interface and the other to mass transport toward the electrode. Rs stands for the series resistance, which includes the TCO resistance of the glass substrate, the resistance related to the ionic conductivity in the electrolyte and the external contacts resistance (*e.g.* wire connections).

The impedance measurements of the two different samples were carried out under dark conditions within potential range of 0.95 V_{RHE} to 1.25 V_{RHE}, with a step of 50 mV. Fitting the proposed electrical circuit analogue to the experimental EIS data, parameters R_{CT} and C_{SC} were obtained. These parameters are plotted in Figure 3.8 as a function of the applied potential.

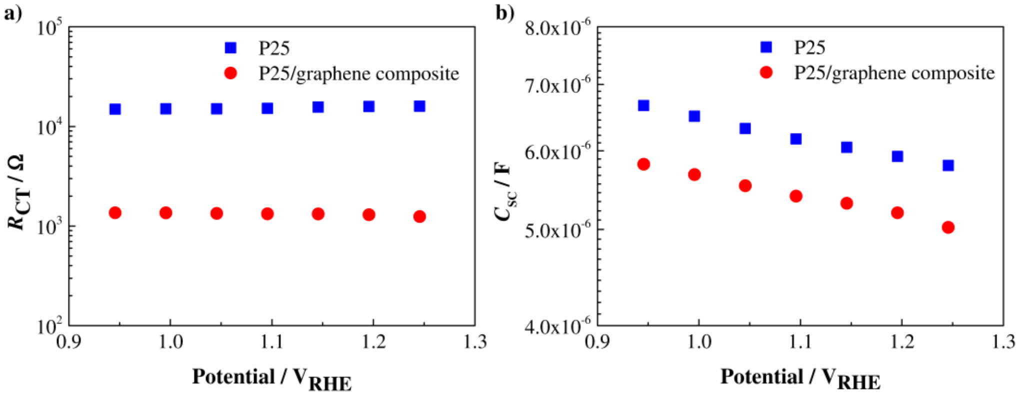

Figure 3.8. Impedance results obtained by fitting the experimental data to the equivalent electrical circuit shown in Figure 3.5 plotted versus the applied potential with reference to RHE: **a)** charge transfer resistance and **b)** space charge capacitance.

Analyzing Figure 3.8, it is possible to conclude that independently of the applied potential, P25 presents higher charge transfer resistance and higher space charge capacitance. On the other hand, the presence of graphene on the composite induces a decrease in the space charge capacitance and in the charge transfer resistance, as it can be observed in the Nyquist diagram (Figure 3.6a) by the shorter semicircle obtained in the higher frequency range. These results point out that in the bare P25 photocatalyst electrons have more difficulty to reach the semiconductor/electrolyte interface where the photocatalytic degradation takes place and more electrons have the possibility of recombining before reacting with pollutants. The better photocatalytic performance of the P25/graphene composite is then addressed to a smaller e^-/h^+ recombination since lower charge transfer resistance and space charge capacitance allow efficient charge separation of electron/hole pairs and fast conduction until the surface to react with contaminants.

For confirming the lower e^-/h^+ recombination at P25/graphene composite, the electron lifetime $\left(\tau_{e^-}\right)$ at the depletion layer of the semiconductor was calculated based on the values for the charge transfer resistance and space charge capacitance [39] - equation 3.3:

$$\tau_{e^-} = R_{\mathrm{CT}} C_{\mathrm{SC}} \qquad 3.3$$

Figure 3.9 presents the electron lifetime for P25 and P25/graphene composite. As expected, the composite shows a shorter lifetime comparatively to P25, meaning that the time that an electron spends in the depletion layer of the semiconductor is very low, diminishing the probability of surface recombining with a hole. Indeed, the charge transfer process of the electron to the semiconductor surface is faster, enabling the presence of a high amount of electrons in the surface for producing radicals that will react with the pollutants. The slow recombination of photogenerated carriers was then confirmed.

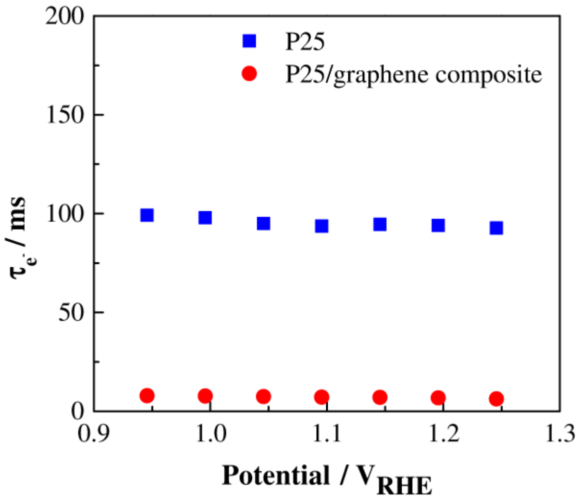

Figure 3.9. Electron lifetimes for the two photocatalysts under study plotted versus the applied potential with reference to RHE.

3.4 Conclusion

In the present study a commercial photocatalyst (P25 from Evonik®, Germany) and the correspondent graphene composite were electrochemically characterized. Photocatalytic activity of these two catalysts was assessed according to the standard ISO 22197-1:2007; the best performing photocatalyst was the P25/graphene composite. It can be concluded that the incorporation of graphene improves the performance of the photocatalyst, originating higher NO conversions than P25. This behavior was further studied based on electrochemical characterization. First, the photocurrent-potential (J–V) in the dark and under UV radiation was obtained; P25/graphene composite shows higher photocurrent under UV light than P25. Then electrochemical impedance spectroscopy (EIS) was used for assessing the charge transfer within the two photocatalysts. Indeed, this technique allows discriminating the different charge pathways that control the performance of photocatalysts. A three-electrode configuration was used and Randles electrical analogue was chosen to fit the experimental data. The model proved to fit quite well to the experimental results allowing obtaining the charge transfer resistance and the space charge capacitance of the photocatalysts. The composite sample exhibited lower values of R_{CT} and C_{SC}, supporting the higher photocatalytic activity for NO degradation and the higher photocurrent compared to P25. P25/graphene composite enhances charge mobility to the surface, decreasing the probability of electron/hole recombination. Additionally, the TiO_2/graphene photocatalyst enables the absorption of a wider range of wavelengths, band gap of 2.9 eV, allowing its use visible light photocatalysis.

Finally, it should be emphasized that electrochemical impedance spectroscopy is a suitable technique to characterize photocatalysts, providing meaningful and easy to obtain information concerning charge transfer and recombination.

Acknowledgements

Joana Ângelo and Pedro Magalhães are grateful to the Portuguese Foundation for Science and Technology (FCT) for their PhD Grants (Ref: SFRH/BD/79974/2011 and Ref: SFRH/BD/78827/2011, respectively). Luísa Andrade acknowledges European Research Council for funding within project BI-DSC – Building Integrated Dye sensitized Solar Cells (Contract Number: 321315). This work was financially supported by: Project POCI-01-0145-FEDER-006939 (Laboratory for Process Engineering, Environment, Biotechnology and Energy – LEPABE funded by FEDER funds through COMPETE2020 - Programa Operacional Competitividade e Internacionalização (POCI) – and by national funds through FCT - Fundação para a Ciência e a Tecnologia. The authors are very thankful to CEMUP for the SEM analyses.

References

1. Ohko, Y., Tatsuma, T., and Fujishima, A., *Characterization of TiO_2 Photocatalysis in the Gas Phase as a Photoelectrochemical System: Behavior of Salt-Modified Systems.* The Journal of Physical Chemistry B, 105(41): p. 10016-10021, **2001**
2. Hoffmann M.R., Martin S.T., Choi W. and Bahnemann D.W., *Environmental Applications of Semiconductor Photocatalysis*. Chemical Reviews, 95: p. 69-96, **1995**
3. Fujishima, A., Rao, T.N., and Tryk, D.A., *Titanium dioxide photocatalysis*. Journal of Photochemistry and Photobiology, C: Photochemistry Reviews, 1(1): p. 1-21, **2000**
4. Teh, C.M. and Mohamed, A.R., *Roles of titanium dioxide and ion-doped titanium dioxide on photocatalytic degradation of organic pollutants (phenolic compounds and dyes) in aqueous solutions: A review.* Journal of Alloys and Compounds, 509(5): p. 1648-1660, **2011**
5. Hager, S. and Bauer, R., *Heterogeneous photocatalytic oxidation of organics for air purification by near UV irradiated titanium dioxide.* Chemosphere, 38(7): p. 1549-1559, **1999**
6. Luo L., Yang Y., Zhang A., Wang M., Liu Y., Bian L., Jiang F. and Pan X., *Hydrothermal synthesis of fluorinated anatase TiO_2/reduced graphene oxide nanocomposites and their photocatalytic degradation of bisphenol A*. Applied Surface Science, 353: p. 469-479, **2015**
7. Ângelo, J., Andrade, L., Madeira, L.M., and Mendes, A., *An overview of photocatalysis phenomena applied to NO_x abatement.* Journal of Environmental Management, 129: p. 522-539, **2013**
8. Zhao F., Dong B., Gao R., Su G., Liu W., Shi L., Xia C. and Cao L., *A three-dimensional graphene-TiO_2 nanotube nanocomposite with exceptional photocatalytic activity for dye degradation*. Applied Surface Science, 351: p. 303-308, **2015**
9. Zhang, H., Lv, X., Li, Y., Wang, Y., and Li, J., *P25-Graphene Composite as a High Performance Photocatalyst. ACSNano*, 4: p. 380-386, **2010**
10. Geim, A., *Graphene: status and prospects.* Science, 324: p. 1530-1534, **2009**

11. Hsieh S.H., Chen W.J. and Yeh T.H., *Effect of various amounts of graphene oxide on the degradation characteristics of the ZnSe/graphene nanocomposites*. Applied Surface Science, 358 (Part A): p. 63-69, **2015**
12. Rahimi R., Zargari S., Yousefi A., Yaghoubi Berijani M., Ghaffarinejad A. and Morsali A., *Visible light photocatalytic disinfection of E. coli with TiO_2–graphene nanocomposite sensitized with tetrakis(4-carboxyphenyl)porphyrin*. Applied Surface Science, 355: p. 1098-1106, **2015**
13. Xiang Q., Yu J. and Jaroniec M., *Graphene-based semiconductor photocatalysts*. Chemical Society Reviews, 41: p. 782-796, **2012**
14. Tanaka, D. and Mendes, A., *Composite Grapheno-Metal Oxide Platelet Method of Preparation and Applications*, in *PCT/IB2010/055598*. **2010**.
15. Nguyen-Phan, T. D., Pham, V.H., Shin, E.W., Pham, H. D., Kim, S., Chung, J.S., Kim, E.J., and Hur, S.H., *The role of graphene oxide content on the adsorption-enhanced photocatalysis of titanium dioxide/graphene oxide composites.* Chemical Engineering Journal (Lausanne), 170(1): p. 226-232, **2011**
16. Liu, S., Sun, H., Liu, S., and Wang, S., *Graphene facilitated visible light photodegradation of methylene blue over titanium dioxide photocatalysts.* Chemical Engineering Journal (Lausanne), 214(0): p. 298-303, **2013**
17. Shi, M., Shen, J., Ma, H., Li, Z., Lu, X., Li, N., and Ye, M., *Preparation of graphene–TiO_2 composite by hydrothermal method from peroxotitanium acid and its photocatalytic properties.* Colloids and Surfaces A: Physicochemical and Engineering Aspects, 405: p. 30-37, **2012**
18. Fabregat-Santiago, F., Garcia-Belmonte, G., Bisquert, J., Zaban, A., and Salvador, P., *Decoupling of Transport, Charge Storage, and Interfacial Charge Transfer in the Nanocrystalline TiO_2/Electrolyte System by Impedance Methods.* The Journal of Physical Chemistry B, 106(2): p. 334-339, **2002**
19. Lana-Villarreal, T., Bisquert, J., Mora-Seró, I., and Salvador, P., *Experimental Evidence of a UV Light-Induced Long-Range Electric Field in Nanostructured TiO_2 Thin Films in Contact with Aqueous Electrolytes.* The Journal of Physical Chemistry B, 109(20): p. 10355-10361, **2005**

20. Baram, N. and Ein-Eli, Y., *Electrochemical Impedance Spectroscopy of Porous TiO_2 for Photocatalytic Applications.* The Journal of Physical Chemistry C, 114(21): p. 9781-9790, **2010**
21. Rüdiger, C., Maglia, F., Leonardi, S., Sachsenhauser, M., Sharp, I.D., Paschos, O., and Kunze, J., *Surface analytical study of carbothermally reduced titania films for electrocatalysis application.* Electrochimica Acta, 71: p. 1-9, **2012**
22. Hasan, M.R., Lai, C.W., Bee Abd Hamid, S., and Jeffrey Basirun, W., *Effect of Ce Doping on RGO-TiO_2 Nanocomposite for High Photoelectrocatalytic Behavior.* International Journal of Photoenergy, 2014: p. 8, **2014**
23. Bloh, J.Z., Folli, A., and Macphee, D.E., *Adjusting Nitrogen Doping Level in Titanium Dioxide by Codoping with Tungsten: Properties and Band Structure of the Resulting Materials.* The Journal of Physical Chemistry C, 118(36): p. 21281-21292, **2014**
24. Hummers, W.S. and Offeman, R.E., *Preparation of Graphitic Oxide.* Journal of the American Chemical Society, 80(6): p. 1339-1339, **1958**
25. Magalhães, P., Ângelo, J., Sousa, V., Nunes, O., Andrade, L., and Mendes, A., *Synthesis and Assessment of a Graphene-based Composite Photocatalyst.* Biochemical Engineering Journal, 104: p. 20-26, **2015**
26. Ângelo, J., Andrade, L., and Mendes, A., *Highly active photocatalytic paint for NO_x abatement under real-outdoor conditions.* Applied Catalysis A: General, 484: p. 17-25, **2014**
27. Devahasdin, S., Fan Jr, C., Li, K., and Chen, D.H., *TiO_2 photocatalytic oxidation of nitric oxide: transient behavior and reaction kinetics.* Journal of Photochemistry and Photobiology, A: Chemistry, 156(1–3): p. 161-170, **2003**
28. Águia, C., Ângelo, J., Madeira, L.M., and Mendes, A., *Photo-oxidation of NO using an exterior paint - Screening of various commercial titania in powder pressed and paint films.* Journal of Environmental Management, 92(7): p. 1724-1732, **2011**
29. Lopes, T., Andrade, L., Ribeiro, H.A., and Mendes, A., *Characterization of photoelectrochemical cells for water splitting by electrochemical impedance spectroscopy.* International Journal of Hydrogen Energy, 35(20): p. 11601-11608, **2010**

30. Aleksandrzak M., Adamski P., Kukułka W., Zielinska B. and Mijowska E., *Effect of graphene thickness on photocatalytic activity of TiO_2-graphene nanocomposites*. Applied Surface Science, 331: p. 193-199, **2015**
31. Yang Y., Luo L., Xiao M., Li H., Pan X. and Jiang F., *One-step hydrothermal synthesis of surface fluorinated TiO_2/reduced graphene oxide nanocomposites for photocatalytic degradation of estrogens*. Materials Science in Semiconductor Processing, 40: p. 183-193, **2015**
32. Trapalis A., Todorova N., Giannakopoulou T., Boukos N., Speliotis T., Dimotikali D. and Yu J., *TiO_2/graphene composite photocatalysts for NO_x removal: A comparison of surfactant-stabilized graphene and reduced graphene oxide*. Applied Catalysis B: Environmental, 180: p. 637-647, **2016**
33. Allen J. Bard, M.S., Stuart Licht *Fundamentals of Semiconductor Electrochemistry and Photoelectrochemistry*, in *Encyclopedia of Electrochemistry - Semiconductor Electrodes and Photoelectrochemistry,* Wiley-VCH, **2002**.
34. Leary R. and Westwood A., *Carbonaceous nanomaterials for the enhancement of TiO_2 photocatalysis.* Carbon, 49: p. 741-772, **2011**
35. Jing, J., Zhang, Y., Li, W., and Yu, W.W., *Visible light driven photodegradation of quinoline over TiO_2/graphene oxide nanocomposites.* Journal of Catalysis, 316: p. 174-181, **2014**
36. Wang W., Yu J., Xiang Q. and Cheng B., *Enhanced photocatalytic activity of hierarchical macro/mesoporous TiO_2–graphene composites for photodegradation of acetone in air*. Applied Catalysis B: Environmental, 119–120: p. 109-116, **2012**
37. Krishnan, R., *Fundamentals of Semiconductor Electrochemistry and Photoelectrochemistry*, in *Encyclopedia of Electrochemistry,* Wiley-VCH Verlag GmbH & Co. KGaA, **2007**
38. V.F. Lvovich, Impedance Spectroscopy: Applications to Electrochemical and Dielectric Phenomena, Wiley, **2012**
39. Andrade, L., Zakeeruddin, S.M., Nazeeruddin, M.K., Aguilar Ribeiro, H., Mendes, A., and Grätzel, M., *Influence of Sodium Cations of N3 Dye on the Photovoltaic Performance and Stability of Dye-Sensitized Solar Cells.* ChemPhysChem, 10(7): p. 1117-1124, **2009**

PART II: Chapter 4

Modelling of NO photoabatement using commercial titanium dioxide

Chapter 4.

Modelling of NO photoabatement using commercial titanium dioxide

Joana Ângelo, Pedro Magalhães, Luísa Andrade, Luís M. Madeira and Adélio Mendes

(*To be submitted, 2016*)

Abstract

Photocatalysis was appointed as a suitable process for the photoabatement of atmospheric pollutants. The photooxidation mechanism on TiO_2 has been widely studied. However, recent studies demonstrated that the ever-assumed photooxidation intermediated by the hydroxyl radical cannot explain all the experimental observations.

This chapter contributes for the development of a phenomenological model for the photooxidation of NO. First, the adsorption equilibrium isotherms of NO, NO_2 and H_2O on the photocatalyst, Aeroxide® P25 from Evonik Industries, were obtained. Also, the concentration of hydroxyl radicals was determined by photoluminescence confirming that this radical is not the main intermediate species for the photooxidation of NO. A comprehensive design of experiments was then followed; NO conversion and selectivity towards nitrite and nitrate ions were obtained as a function of the relative humidity, irradiance, NO inlet concentration and residence time, following a response surface methodology (RSM). These results were then used to validate a new phenomenological model. This model assumes that the photooxidation is mainly intermediated by surface lattice oxygen radicals and the injected electron reacts with oxygen to produce superoxide ions. The proposed model fits reasonably well the experimental results.

Keywords: Photocatalysis; Adsorption; Kinetic model; Titanium dioxide; Pollutants degradation.

4.1 Introduction

Photocatalysis with titanium dioxide (TiO_2) is a promising approach to the oxidation of atmospheric pollutants such as NO_x [1-4]. Nitrogen oxides (NO) can be easily oxidized into nitric acid (HNO_3) when titanium dioxide is irradiated with UV light. The mechanism for photocatalytic oxidation of NO with titanium dioxide has been studied and discussed by several authors and different oxidation pathways have been proposed [5-10]. The photocatalytic phenomenon comprises five main pathways: generation of charge carries, recombination, adsorption/desorption of reagents and products, trapping and oxidation of pollutants – Figure 4.1 [5, 11]. TiO_2 absorbs photons with sufficient energy to inject electrons from the valence to its conduction band, generating electron-hole pairs. The formed holes can be trapped or can react directly with surface adsorbed species. On the other hand, electrons react with oxygen molecules to form the superoxide anion $\left(O_2^{\bullet -}\right)$.

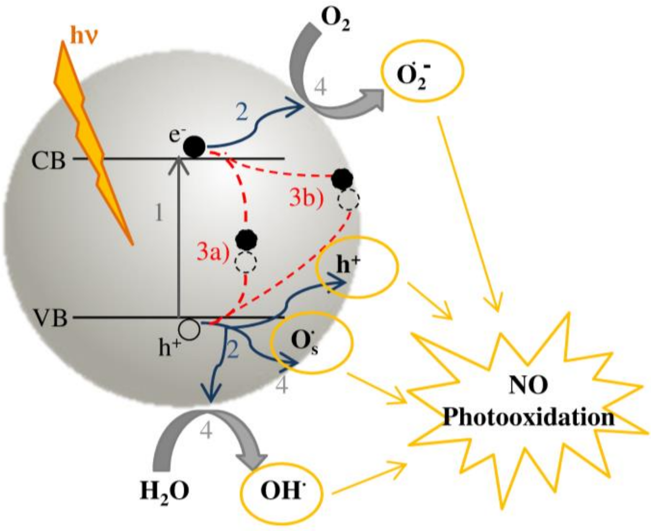

Figure 4.1. Photocatalysis mechanism with main reactions: **1)** electron-hole pair generation, **2)** charge separation and migration to surface reaction sites, **3a)** bulk recombination, **3b)** surface recombination and **4)** trapping of charge carries.

The NO photooxidation mechanism at TiO_2 is still largely controversial. A large number of studies assume that hydroxyl radical is the main oxidant intermediate in photocatalytic reactions [5-7, 12, 13]; other studies claim that holes can react directly with pollutants [5, 7, 8] and more recently Ohko *et al.* [9, 10] suggested that lattice oxygen radicals are the responsible for NO oxidation.

Ishibaschi and co-workers [14] studied the role of hydroxyl radicals and photogenerated holes on the photooxidation by titanium dioxide. These authors used terephthalic acid as a fluorescent probe for quantitatively determining the hydroxyl radicals concentration. Furthermore, they used the iodo-starch reaction to quantify I_2 formed from the photooxidation of I^- at titanium dioxide photocatalyst. These two experiments were performed under the same conditions. Comparing the quantum yield for I_2 and $OH^\bullet$ formation, these authors concluded that hydroxyl radicals could not be the only species responsible for the photooxidation process. Thus, they claimed that holes play an important role on the photocatalytic mechanism. Additionally, experiments with electron paramagnetic resonance (EPR) spectroscopy showed that generated holes are trapped at titanium dioxide surface originating oxygen anion radicals [14, 15]. The reaction between holes and TiO_2 surface lattice oxygen ions was then studied by other authors [16, 17]. Photoinduced oxygen isotopic exchange and surface spectroscopy techniques in combination with high-resolution scanning tunneling microscopy were used to study the interaction of H_2O and O_2 species with the TiO_2 surface [17]. These studies concluded that when electron-holes are formed, the holes are trapped by lattice oxygen ions of titanium dioxide surface generating surface lattice radicals able to react with pollutants [16, 17]. More recently, Muñoz-Batista and co-workers [7] reported that the direct oxidation rate of pollutants by holes is slower than the oxidation intermediated by hydroxyl radicals.

Since surface lattice radicals are the most important oxidation intermediate species on TiO_2-based photocatalysis, the adsorption of NO on the active sites of the semiconductor is a critical step for its photooxidation. Thus, in the majority of photocatalytic studies reported Langmuir-Hinshelwood kinetic models have been considered to describe the oxidation reaction rate.

Several factors, such as air humidity, temperature, NO concentration, flow rate/residence time, photocatalyst film thickness and irradiance influence the photodegradation rate of NO. The photocatalytic phenomenon starts with TiO_2 particles absorbing a photon and the consequent formation of an electron-hole pair, [12, 18, 19]. The role of the relative humidity (*RH*) is one of the most discussed factors on photocatalysis. As hydroxyl radical is considered by several authors to be the main oxidant, it is expectable that increasing *RH* the NO conversion increases. However, it was reported that conversion increases with *RH* until a certain limit, becoming constant afterwards [2, 20]. On the other hand, oxygen has an important role in the photodegradation mechanism since this species is responsible for trapping the free electrons [5, 7]. The influence of temperature is less discussed in literature since photocatalytic processes normally work at room temperature [21]. In case of inlet concentration (for continuous flow reactor), numerous studies demonstrated that lower feed concentrations yield higher NO conversion [2, 20]. Concerning the flow rate, it is expected that higher flows (smaller residence times) result in lower NO conversions [2, 22]. The same goes for TiO_2 film thickness, until reaching the optical thickness. This optical thickness is the one at which the film becomes opaque [21, 23].

A design of experiments was performed in this chapter to study the influence of relative humidity, irradiance, inlet NO concentration and residence time in the photooxidation. The effect of these operation conditions was assessed based on NO conversion and selectivity towards nitrite and nitrate ions. Thereafter, a phenomenological model was proposed using as reference semiconductor P25 photocatalyst. This model assumes the adsorption of reagents and products in active sites of titanium dioxide. The adsorption equilibrium isotherms of H_2O, NO and NO_2 were obtained experimentally by the gravimetric method. The proposed model was fitted to experimental values and a good agreement was achieved.

4.2 Experimental

4.2.1 *Design of Experiments – Response Surface Methodology*

A response surface methodology (RSM) with a central composite design (CCD) was followed to study the role of different operating conditions on NO photooxidation. NO conversion and selectivity to other products rather than NO_2 (e.g. HNO_2 and HNO_3) on P25 were assessed under different operating conditions. These variables are given by equations 4.1 and 4.2:

$$X_{\mathrm{NO}} = \left(\frac{[\mathrm{NO}]_{\mathrm{in}} - [\mathrm{NO}]_{\mathrm{out}}}{[\mathrm{NO}]_{\mathrm{in}}} \right) \times 100 \qquad 4.1$$

$$S = \left(1 - \frac{[\mathrm{NO_2}]_{\mathrm{out}}}{[\mathrm{NO}]_{\mathrm{in}} - [\mathrm{NO}]_{\mathrm{out}}} \right) \times 100 \qquad 4.2$$

where X_{NO} is the conversion of NO, $[\mathrm{NO}]$ and $[\mathrm{NO_2}]$ the concentrations of NO and NO_2, respectively, and the subscripts (in and out) refer to the inlet and outlet of the photoreactor.

An experimental setup partially implementing standard ISO 22197-1:2007 was used to obtain the conversion and selectivity data, as described elsewhere [24] (cf. chapter 2). The photoreactor, with a photoactive area of 0.05 m x 0.23 m x 0.005 m (width x length x height), was placed in a thermostatic cabinet and illuminated using a UV lamp (Vilbert Lourmat – BLB 365 nm, 2 x 6 W). A chemiluminescence analyzer (Thermo electron 42C) was used to control the inlet and outlet concentrations of NO and NO_2.

The design of experiments was run in commercial software JMP 7, SAS. RSM is a very useful tool to study and model processes with a dependence between responses and operating conditions, where model parameters are estimated using the least squares method [25]. The CCD is usually applied for processes with multiple factors and complex interactions [26]. The selected experimental factors are air humidity (RH), UV irradiance (I), residence time (τ) and inlet NO concentration $\left([\mathrm{NO}]_{\mathrm{in}}\right)$; Table 4.1 presents the design factors and respective levels. The central point value of the factors was chosen based on the suggested values by standard ISO 22197-1:2007, except for the residence time, where the chosen value was $\tau = 1.3$ s. This last factor was defined by flow rate limitations (≈ 0.6-0.7 $L_N{\cdot}min^{-1}$) of the NO_x analyzer equipment (Thermo electron 42C).

Table 4.1. CCD factors and respective levels.

Factor	Symbol	Level		
		-1	0	+1
RH / %	χ_1	25	50	75
I / $W{\cdot}m^{-2}$	χ_2	5	10	15
τ / s	χ_3	0.4	1.3	2.1
$[NO]_{in}$ / ppm	χ_4	0.5	1	1.5

The process responses can be described by a second order polynomial equation:

$$\begin{aligned} y = a_0 + a_1\chi_1 + a_2\chi_2 + a_3\chi_3 + a_4\chi_4 + a_{12}\chi_1\chi_2 + a_{13}\chi_1\chi_3 + a_{14}\chi_1\chi_4 + a_{23}\chi_2\chi_3 \\ + a_{24}\chi_2\chi_4 + a_{34}\chi_3\chi_4 + a_{11}\chi_1^2 + a_{22}\chi_2^2 + a_{33}\chi_3^2 + a_{44}\chi_4^2 \end{aligned} \quad 4.3$$

where y is the process response; χ_1, χ_2, χ_3 and χ_4 are the dimensionless process factors; a_0 is the interception coefficient; a_1, a_2, a_3 and a_4 are the coefficients of the factors; a_{12}, a_{13}, a_{14}, a_{23}, a_{24} and a_{34} are the cross interaction coefficients and a_{11}, a_{22}, a_{33}, a_{44} are the coefficients of the quadratic factors.

The dimensionless factors ($\chi_1, \chi_2, \chi_3, \chi_4$) are calculated according to:

$$\chi_1 = \frac{RH - 50}{25} \quad 4.4$$

$$\chi_2 = \frac{I - 10}{5} \quad 4.5$$

$$\chi_3 = \frac{\tau - 1.286}{0.857} \quad 4.6$$

$$\chi_4 = \frac{[\mathrm{NO}]_{\mathrm{in}} - 1}{0.5} \quad 4.7$$

4.2.2 Adsorption equilibrium isotherms

The adsorption isotherms of NO, NO_2 and water vapor were determined by the gravimetric method. In this method, photocatalyst (P25) is exposed to the gas and the weight variation is measured along time for different pressures and the adsorbed amount is determined. These trials were conducted in a magnetic suspension balance from Rubotherm at 25ºC. A detailed description of the experimental setup is given elsewhere [27].

4.2.3 Quantification of hydroxyl radicals

Hydroxyl radicals produced by P25 were determined by photoluminescence (PL). Coumarin (COU) was chosen as probe molecule since this species reacts stoichiometrically with $OH^{\bullet}$ producing a highly fluorescent product, 7-hydroxycoumarin (7HC) [28-31]. First, different concentrations of 7-hydroxycoumarin were prepared and photoluminescence signal was measured at 456 nm (PL signal of 7HC) to obtain the photoluminescence calibration curve. This calibration curve allowed the quantification of photogenerated $OH^{\bullet}$. For these experiments titanium dioxide (P25) was dispersed in 100 mL of 10^{-3} M coumarin and kept in dark for 30 min to reach the adsorption-desorption equilibrium. After this period, the solution was irradiated (UV light - 10 $W \cdot m^{-2}$) for three hours, and samples were collected each 30 minutes. They were then centrifuged and analyzed on a spectrofluorophotometer (*RF*-5301, Shimadzu) at 456 nm. The measurements were performed for two concentrations of P25 at room temperature with an excitation wavelength of 332 nm, setting the emission and excitation slits to 3.0 nm.

4.3 Results and discussion

4.3.1 Design of Experiments – Response Surface Methodology

According to RSM analysis, 26 experiments were conducted to evaluate the effect of the four factors under study. All experiments were run at 25 °C and lasted 24 h to guarantee that the steady state was reached; the other operating conditions and response results are shown in Table 4.2.

Table 4.2. Experimental conditions and observed values of process responses.

Run#	**Experimental conditions**				**Responses**	
	***RH* / %**	***I* / W·m^{-2}**	**τ / s**	**[NO]$_{in}$ / ppm**	**X$_{NO}$ / %**	**S / %**
1	25	15	0.4	1.5	42.0	31.8
2	25	15	0.4	0.5	49.4	21.4
3	25	5	0.4	1.5	26.9	5.2
4	25	15	2.1	0.5	96.1	37.3
5	75	5	0.4	1.5	13.7	16.6
6	25	5	2.1	0.5	93.2	34.4
7	50	10	1.3	1.5	54.4	49.0
8	75	15	0.4	1.5	25.5	21.8
9	25	10	1.3	1.0	70.2	42.2
10	50	10	1.3	1.0	60.3	35.4
11	50	10	0.4	1.0	30.3	22.1
12	50	10	1.3	1.0	60.4	34.1
13	50	10	1.3	0.5	89.9	37.8
14	75	10	1.3	1.0	49.7	33.7
15	75	5	2.1	1.5	46.4	39.4
16	50	5	1.3	1.0	51.2	31.0
17	75	5	0.4	0.5	27.4	28.4
18	75	15	2.1	0.5	91.2	36.7
19	50	15	1.3	1.0	69.8	36.8
20	75	15	2.1	1.5	66.8	57.6
21	75	15	0.4	0.5	37.6	34.5
22	25	5	0.4	0.5	41.2	23.6
23	75	5	2.1	0.5	72.9	33.0
24	50	10	2.1	1.0	78.0	46.5
25	25	15	2.1	1.5	82.4	71.0
26	25	5	2.1	1.5	72.9	68.0

The response values were taken as an average over the last 3 hours. Runs #10 and #12 were performed under the same operating conditions (center of the domain) and the values obtained for the respective responses were very similar, validating a good reproducibility. The analysis of variance (ANOVA) of responses was made and it was observed that p-values of t-student test were lower than 0.05, which is an indication of the model significance. The obtained R^2 coefficients were close to the unit: 0.980 for X_{NO} and 0.949 for S, which is also relevant for the validation of the model used.

Table 4.3. Analysis of variance for the models parameters of the responses.

X_{NO}			S		
Parameter	*Estimated*	*Prob* >|*t*|	*Parameter*	*Estimated*	*Prob* >|*t*|
a_0	62.716	<0.0001*	b_0	37.094	<0.0001*
a_1	-7.950	<0.0001*	b_1	-1.844	0.1438
a_2	6.389	0.0002*	b_2	3.850	0.0073*
a_3	-9.328	<0.0001*	b_3	4.072	0.0052*
a_4	22.550	<0.0001*	b_4	12.139	<0.0001*
a_{12}	1.563	0.2369	b_{12}	0.181	0.8867
a_{13}	-1.313	0.3159	b_{13}	-3.531	0.0160*
a_{14}	-0.750	0.5604	b_{14}	-3.956	0.0087*
a_{23}	1.075	0.4078	b_{23}	2.656	0.0559
a_{24}	0.363	0.7771	b_{24}	-0.494	0.6988
a_{34}	-2.338	0.0881	b_{34}	7.944	<0.0001*
a_{11}	-3.554	0.2791	b_{11}	0.074	0.9814
a_{22}	-3.004	0.3566	b_{22}	-3.976	0.227
a_{33}	8.646	0.0183*	b_{33}	5.524	0.103
a_{44}	-9.354	0.0122*	b_{44}	-3.576	0.2741

*Parameters with significance.

On the other hand, the p-values of the model parameters allow determining the influence of which factor in the responses; a small p-value (less than 0.05) means a significant influence of factor in response result [25] - Table 4.3. The model was run again considering only the parameters with a significant influence on the responses. The final NO conversion and selectivity polynomial response became:

$$y_{X_{NO}} = 61.72 - 7.95\chi_1 + 6.39\chi_2 - 9.33\chi_3 + 22.55\chi_4 + 6.09\chi_3^2 - 11.91\chi_4^2 \qquad 4.8$$

$$y_S = 35.74 - 1.84\chi_1 + 3.85\chi_2 + 4.07\chi_3 + 12.14\chi_4 - 3.53\chi_1\chi_3 - 3.96\chi_1\chi_4 + 7.94\chi_3\chi_4 \qquad 4.9$$

Figures 4.2 and 4.3 compare the experimental results as a function of the fitting data for the two responses. These figures show a good agreement between experimental and predicted values with R^2 coefficients close to the unit.

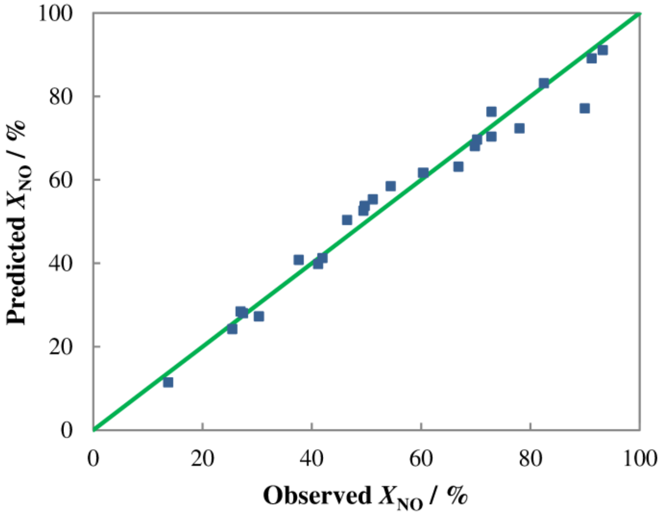

Figure 4.2. Parity plot of experimental *vs.* predicted NO conversion values (R^2=0.980).

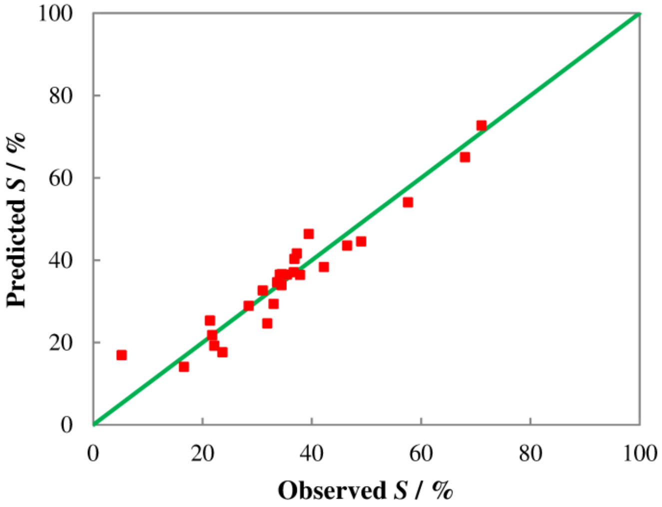

Figure 4.3. Parity plot of experimental vs. predicted selectivity values (R^2=0.948).

Equations 4.8 and 4.9 were plotted as a function of the four factors studied to give the response hypersurfaces of X_{NO} and S – Figures 4.4 and 4.5.

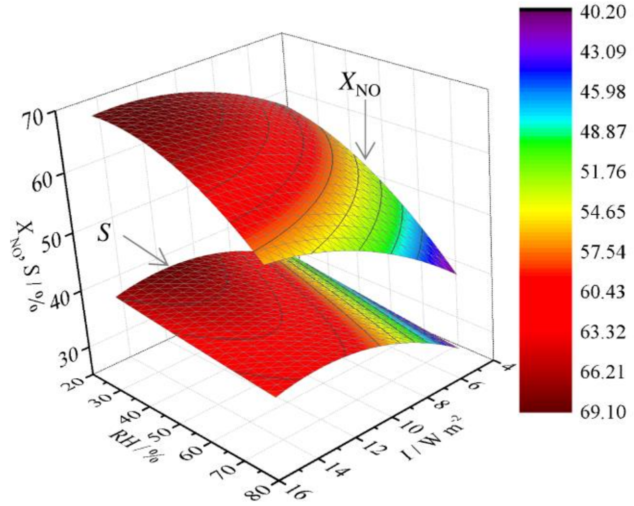

Figure 4.4. Predicted NO conversion (X_{NO}) and selectivity (S) as function of relative humidity (RH) and UV irradiance (I), keeping $[NO]_{in}$ and τ at middle value (10 ppm and 1.3 s, respectively).

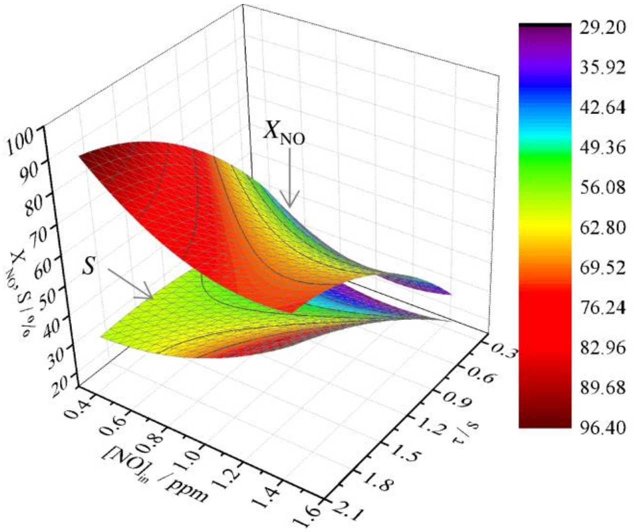

Figure 4.5. Predicted NO conversion and selectivity as function of $[NO]_{in}$ and residence time (τ), keeping RH and I at middle value (50 % and 10 W·m^{-2}, respectively).

NO conversion and selectivity increase for the highest values of irradiance and residence time. However, the influence of inlet NO concentration is different for the two responses; the NO conversion is higher for smaller concentrations but selectivity is higher for higher concentrations. On the other hand, a smaller relative humidity presents the highest values of NO conversion and selectivity.

The influence of the operating conditions was different for each response making the overall optimisation more complex. The JMP software uses a desirability function, which allows assigning different weights to the responses. In this study, three different desirability functions were established – Table 4.4:

1. Same weight to the NO conversion and selectivity;
2. Only the NO conversion was considered;
3. Only the selectivity was considered.

Table 4.4. Optimal conditions and respective (predicted and observed) response results.

	Maximize X_{NO} and S	**Maximize X_{NO}**	**Maximize S**
RH / %	25	25	25
I / W·m^{-2}	15.0	13.0	15.0
$[NO]_{in}$ / ppm	1.5	0.5	1.5
τ / s	2.1	2.1	2.1
$X_{NOpredicted}$ / %	83.2 ± 7.4	[100.0, 93.7]	83.2 ± 7.4
$X_{NOobserved}$ / %	82.4 ± 0.3	96.12 ± 0.2	82.4 ± 0.3
$S_{predicted}$ / %	72.7 ± 7.5	40.3 ± 6.3	72.7 ± 7.5
$S_{observed}$ / %	71.0 ± 0.3	37.3 ± 0.7	71.0 ± 0.3

The importance of water in photocatalytic processes has been widely discussed [5, 16, 32]. To shade light on that, it was decided to perform two additional experiments for $RH = 12.5$ % and $RH \approx 0$ %, enlarging the initially selected domain (between 25 % and 75 %). To obtain a $RH \approx 0$ %, the photoreactor was initially first placed in an oven for 24 h at 150 ºC in N_2 atmosphere. However, it was not possible to obtain a complete dry stream because it was used compressed air with a dew point of -40 ºC, which represents *ca.* 200 ppm of H_2O.

Table 4.5 shows the new NO conversions and selectivities, besides the previously obtained for relative humidities of 25 % and 75 %, where the other operating conditions were: $[NO]_{in} = 1.5$ ppm; $I = 15$ W·m^{-2} and $\tau = 2.1$ s. For $RH = 50$ % the value was taken from the model. From Table 4.5 it can be concluded that the relative humidity favors the photocatalytic process until a value close to $RH = 25$ %.

Table 4.5. NO conversion and selectivity for different values of RH ($[NO]_{in}$ = 1.5 ppm; I = 15 W·m^{-2} and τ = 2.1 s).

RH / %	X_{NO} / %	S / %
75	66.8	57.6
50	75.5*	57.0*
25	82.4	71
12.5	81.8	73.8
≈ 0	75.7	60.7

*Model value

Since it was found that water is not required for the NO conversion, it was decided to assess the role of oxygen in the feeding stream. A set of experiments using a feed stream made of nitrogen and NO (1 ppm) were then performed at $RH \approx 0$ and $RH = 25$ %. It was concluded that without oxygen there is no NO conversion. This is a very significant result that should be further explored. Oxygen should be the only present species able to receive the injected electron from the semiconductor [5].

4.3.2 Adsorption Isotherms

The water vapor adsorption equilibrium isotherm on P25 was obtained at 25 ºC – Figure 4.6. The adsorption equilibrium isotherm shows a Type II behavior for adsorption and desorption, indicating that a monolayer and successive multi-layers of adsorbed water were formed. The experimental data was fitted to the Aranovich-Donohue-Langmuir [33, 34] equation:

$$q = q_m \left[\frac{bP}{(1+bP)[1-(P/P_0)]^d} \right] \tag{4.10}$$

where q is the adsorbed concentration, q_m is the saturation adsorbed concentration, P is the equilibrium partial pressure, P/P_0 the relative pressure, b is the adsorption affinity constant and d a model parameter.

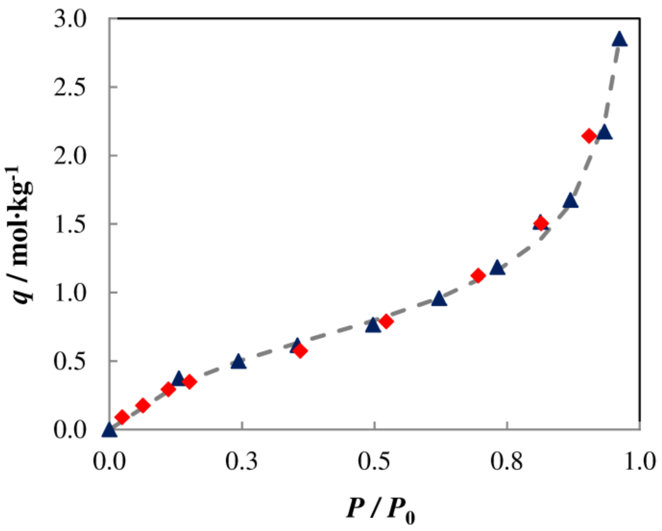

Figure 4.6. Water adsorption (blue) and desorption (red) equilibrium isotherms on P25 at 25 °C. The dashed line is the Aranovich-Donohue-Langmuir isotherm fitting equation 4.10.

From the experimental results it can be concluded that a RH close to 25 % favors the photocatalytic performance of P25. Assuming that the area occupied by an adsorbed water molecule is 0.105 nm^2 [35] the surface area occupied by water at $RH = 25$ % is *ca.* 32 m^2·g^{-1}. This value is close to the surface area of P25, which is ca. 50 m^2·g^{-1} (Manufacturer information).

The adsorption equilibrium isotherms of NO and NO_2 on P25 were obtained also at 25 ºC – Figure 4.7. Dual-site Langmuir equation [34, 36] was used to fit the corresponding adsorption equilibrium isotherms. The Dual-site Langmuir model assumes two types of adsorption sites with no interactions between them[34, 37].

$$q = q_{m,1} \frac{b_{\mathrm{L},1} P}{1 + b_{\mathrm{L},1} P} + q_{m,2} \frac{b_{\mathrm{L},2} P}{1 + b_{\mathrm{L},2} P} \qquad 4.11$$

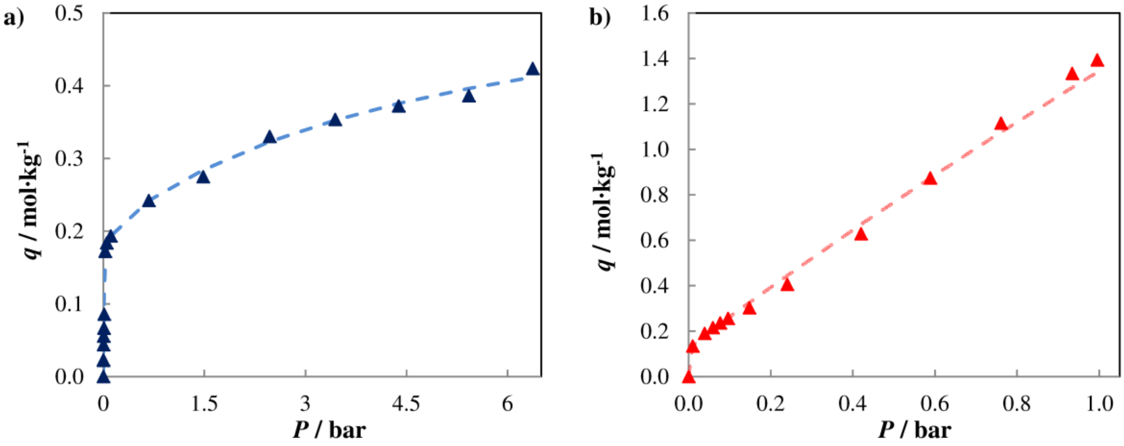

Figure 4.7. Nitrogen oxide **(a)** and nitrogen dioxide **(b)** adsorption isotherms on P25 at 25 °C. Dashed lines represent the isotherm fittings for NO (blue) and NO_2 (red), equation 4.11.

The fitting parameters were estimated minimizing the relative deviations (Δq) between experimental data and the fitting equation, according to equation 4.12[33]; these results are presented in Table 4.6.

$$\Delta q(\%) = \frac{100}{k}\sum_{j=1}^{k}\frac{\left|q_j^{\exp} - q_j^{cal}\right|}{q_j^{\exp}} \qquad 4.12$$

In equation 4.12, $q_j^{\exp}$ is the experimental adsorbed concentration, q_j^{cal} the adsorbed concentration calculated using the fitting equations and k the number of observations.

For low pressures NO and NO_2 isotherms approach to the henry's law [34, 37]. Since NO and NO_2 concentrations in this work are lower than 1.5 ppm, and the reactor is operated at nearly atmospheric pressure, the assumption of linear isotherms holds. The obtained Henry's constants for NO and NO_2 are 21 $mol\cdot bar^{-1}\cdot kg^{-1}$ and 198 $mol\cdot bar^{-1}\cdot kg^{-1}$, respectively, and for H_2O is 111 $mol\cdot bar^{-1}\cdot kg^{-1}$ up to *ca.* 25 % RH.

Table 4.6. Parameters of the adsorption equilibrium isotherms of water, NO and NO_2 on P25.

	Aranovich-Donohue-Langmuir Model	
Water vapor	q_m / mol·kg^{-1}	0.869
	b / bar^{-1}	134.6
	d	0.431
	Δq / %	3.31
	Dual-Site-Langmuir Model	
Nitrogen oxide (NO)	$q_{m,1}$/ mol·kg^{-1}	0.201
	$q_{m,2}$/ mol·kg^{-1}	0.386
	$b_{L,1}$/ bar^{-1}	105.4
	$b_{L,2}$/ bar^{-1}	0.188
	Δq, %	9.54
Nitrogen dioxide (NO_2)	$q_{m,1}$/ mol·kg^{-1}	12.95
	$q_{m,2}$/ mol·kg^{-1}	0.131
	$b_{L,1}$/ bar^{-1}	0.103
	$b_{L,2}$/ bar^{-1}	1704
	Δq, %	4.01

4.3.3 Quantification of hydroxyl radicals

Hydroxyl radicals are formed from the reaction between holes and adsorbed H_2O/OH^- on titanium dioxide surface. The determination of these radicals concentration was performed using a photoluminescence technique with coumarin. The reaction between coumarin and hydroxyl radicals originates a stoichiometric amount of 7-hydroxycoumarin (fluorescent species). A solution with coumarin and P25 was irradiated over time and the photoluminescence signal for 7-hydroxycoumarin was followed using a spectrofluorometer (RF-5301, Shimadzu). PL signal of 7-hydroxycoumarin is proportional to irradiance time, following zero-order reaction rate within the concentrations of P25 and coumarin tested [38]. Thus, plotting 7HC concentration as a function of irradiance time, a linear response is obtained; the kinetic constant for the formation of hydroxyl radical was determined from the slope of this line. Three concentrations of P25 were considered on estimating the photogenerated rate of $OH^{\bullet}$; the respective kinetic values are presented in Table 4.7.

Table 4.7 Values of kinetic constant for the formation of hydroxyl radical for the three photocatalyst concentrations studied.

[P25] / g·L^{-1}	**k_{OH} / µM·min^{-1}**
0.50	0.0010 ± 0.0003
1.25	0.0013 ± 0.0002
2.00	0.0009 ± 0.0001

The obtained values for kinetic constants are in straight agreement with literature [31]. This result confirms that low concentrations of hydroxyl radicals are formed when titanium dioxide is irradiated.

4.3.4 Kinetic Model

The first step of the photocatalytic process is the photon absorption by the semiconductor, with subsequent generation of an electron-hole pair – equation 4.13.

$$TiO_2 + h\nu \longrightarrow e^- + h^+ \qquad 4.13$$

Equations 4.14 to 4.16 describe the charge carriers trapping. The electron is trapped by oxygen and the hole trapped by H_2O_{ads}/OH^-_{ads} [6, 13, 39]:

$$O_2 + e^- \xrightarrow{k_{e^-}} O_2^{\bullet -} \qquad 4.14$$

$$H_2O/OH^-_{ads} + h^+ \xrightarrow{k_{h^+}} OH^{\bullet}_{ads} \qquad 4.15$$

Dillert *et al.* [5] claimed that oxygen is the only species able to trap an electron, being crucial for NO photocatalytic degradation. However, some authors claim that holes are trapped by terminal lattice oxygen ions $\left(>\mathrm{O}_s^{2-}\right)$ of TiO_2 surface resulting in a new radical species $\left(\mathrm{O}_s^{\bullet-}\right)$ able to react with external species [9, 10, 16].

$$\mathrm{h}^+ + \left(>\mathrm{O}_s^{2-}\right) \xrightarrow{k_1} \mathrm{O}_s^{\bullet-} \qquad 4.16$$

However, charge carriers can recombine; this is an undesirable reaction which leads to a decrease in photocatalytic activity of the photocatalyst:

$$\mathrm{e}^- + \mathrm{h}^+ \xrightarrow{k_2} heat \qquad 4.17$$

Adsorption/desorption phenomena of reagents (NO, O_2 and H_2O) and products (NO_2, HNO_2, HNO_3) are very important for the photocatalytic degradation of NO. These species are adsorbed in active sites (S) of titanium dioxide, the equilibrium is reached and the photocatalytic reaction with NO occurs in the adsorbed phase [8, 39, 40]:

$$\mathrm{H_2O + S} \rightleftarrows \mathrm{H_2O_{ads}} \qquad 4.18$$

$$\mathrm{O_2 + S} \rightleftarrows \mathrm{O_{2\,ads}} \qquad 4.19$$

$$\mathrm{NO + S} \rightleftarrows \mathrm{NO_{ads}} \qquad 4.20$$

$$\mathrm{NO_2 + S} \rightleftarrows \mathrm{NO_{2\,ads}} \qquad 4.21$$

For this study, it was considered that the adsorption of H_2O, NO and NO_2 competes for the same active sites (S), while adsorption of O_2 occurs in different active sites (S^*) [6, 12, 39]. Following experimental results of adsorption equilibrium isotherms, linear isotherms were assumed for NO and NO_2. Thus the concentration of adsorbed species is given by:

$$[\mathrm{H_2O_{ads}}] = \frac{K_{\mathrm{H_2O}}[\mathrm{S}][\mathrm{H_2O}]}{1 + K_{\mathrm{H_2O}}[\mathrm{H_2O}]} \qquad 4.22$$

$$[\mathrm{NO_{ads}}] = K_{\mathrm{NO}}[\mathrm{NO}] \qquad 4.23$$

$$[\mathrm{NO_{2ads}}] = K_{\mathrm{NO_2}}[\mathrm{NO_2}] \qquad 4.24$$

$$[\mathrm{O_{2\,ads}}] = \frac{K_{\mathrm{O_2}}[\mathrm{S}^*][\mathrm{O_2}]}{1 + K_{\mathrm{O_2}}[\mathrm{S}^*][\mathrm{O_2}]} \qquad 4.25$$

As mentioned before, the kind of oxidizing species for the degradation of pollutants has been widely discussed. Some studies claim that hydroxyl radical is the main oxidant (equations 4.26 to 4.28) [5-7, 12, 13], but other studies report lattice oxygen radicals as being also responsible for NO oxidation (equations 4.29 to 4.34) [9, 10]. Moreover, other authors suggest a direct reaction between generated holes and adsorbed pollutants (equations 4.35 to 4.37) [5, 7, 8]:

$$NO_{ads} + OH^{\bullet}_{ads} \xrightarrow{k_3} HNO_{2\,ads} \qquad 4.26$$

$$HNO_{2\,ads} + OH^{\bullet}_{ads} \xrightarrow{k_4} NO_{2\,ads} + H_2O \qquad 4.27$$

$$NO_{2\,ads} + OH^{\bullet}_{ads} \xrightarrow{k_5} HNO_{3ads} \rightleftarrows NO^{-}_{3ads} + H^{+} \qquad 4.28$$

$$\begin{aligned} &O_s^{\bullet -} + NO_{ads} + H_2O_{ads} \xrightarrow{k_6} HNO_{2\,ads} + V[O_s^{2-}] + OH^{-}_{ads} \\ &\longrightarrow HNO_{2\,ads} + O_s^{2} + H^{+} \end{aligned} \qquad 4.29$$

$$O_s^{\bullet -} + HNO_{2ads} \xrightarrow{k_7} NO_{2\,ads} + O_s^{2-} + H^{+} \qquad 4.30$$

$$O_s^{\bullet -} + HNO_{2ads} \xrightarrow{k_8} HNO^{-}_{3\,ads} + V[O_s^{2-}] \qquad 4.31(a)$$

$$V[O_s^{2-}] + OH^{-}_{ads} \longrightarrow O_s^{2} + H^{+} \qquad 4.31\ (b)$$

$$O_s^{\bullet -} + HNO^{-}_{3\,ads} \xrightarrow{k_9} HNO_{3\,ads} + O_s^{2-} \qquad 4.32$$

$$\begin{aligned} &O_s^{\bullet -} + NO_{2\,ads} + H_2O_{ads} \xrightarrow{k_{10}} HNO_{3\,ads} + V[O_s^{2-}] + OH^{-}_{ads} \\ &\longrightarrow HNO_{3\,ads} + O_s^{2} + H^{+} \end{aligned} \qquad 4.33$$

$$O_s^{\bullet -} + NO_{2ads} \xrightarrow{k_{11}} NO^{-}_{3\,ads} + V[O_s^{2-}] \qquad 4.34\ (a)$$

$$V[O_s^{2-}] + OH^{-}_{ads} \longrightarrow O_s^{2} + H^{+} \qquad 4.34\ (b)$$

$$h^{+} + NO_{ads} + H_2O_{ads} \longrightarrow HNO_{2\,ads} + H^{+} \qquad 4.35$$

$$h^{+} + HNO_{2\,ads} \longrightarrow NO_{2\,ads} + H^{+} \qquad 4.36$$

$$h^{+} + NO_{2\,ads} + H_2O_{ads} \longrightarrow HNO_{3\,ads} + H^{+} \qquad 4.37$$

where O_s^{2-} represents terminal (bridging) oxygen ions and $V[O_s^{2-}]$ are the bridging oxygen vacancies.

Since lattice oxygen radicals are the main oxidizing intermediate species, the reaction rates of NO and NO_2 are described as follows:

$$r_{NO} = -k_6[NO_{ads}][H_2O_{ads}][O_s^{\bullet-}] \qquad 4.38$$

$$r_{NO_2} = -k_7[HNO_{2\,ads}][O_s^{\bullet-}] - k_B[NO_{2\,ads}][H_2O_{ads}][O_s^{\bullet-}] \qquad 4.39$$

The rate of electron-hole pairs generation (4.13) along with the photocatalytic film thickness (t) is described as [39]:

$$r = \int_{y=0}^{y=t}\int_{\lambda} \phi_\lambda e_{S,\lambda}^{a}(y)\, d\lambda\, dy = \int_{y=0}^{y=t}\int_{\lambda} \phi_\lambda S_g \rho D_{TiO_2} \kappa_\lambda I_\lambda(y)\, d\lambda\, dy \qquad 4.40$$

where ϕ_λ is the primary quantum yield, $e_{S,\lambda}^{a}$ is the local superficial rate of photon absorption, S_g is the specific surface area, ρ is the photocatalyst density, D_{TiO_2} is the fraction of active catalyst, κ_λ is the radiation absorption coefficient of photocatalyst and I_λ the irradiance for the applied light source.

Using the Beer-Lambert law to define the radiation extinction in film thickness,

$$I_\lambda(y) = I_\lambda e^{-\kappa_\lambda y} \qquad 4.41$$

Equation 4.40 can be rewritten considering that all properties are constant for the film thickness [39]:

$$r = I\int_{\lambda} \phi_\lambda S_g \rho D_{TiO_2}(1 - e^{-\kappa_\lambda t})\, d\lambda \;= \alpha I \qquad 4.42$$

where, I is the irradiance on photocatalyst and $\alpha = \int_{\lambda} \phi_\lambda S_g \rho D_{TiO_2}(1 - e^{-\kappa_\lambda t})\, d\lambda$.

Assuming a local equilibrium for lattice oxygen radicals, holes and electrons – steady state behavior - the reaction rate of these species is given by:

$$\begin{aligned} r_{O_s^{\bullet-}} &= k_1[h^+] - k_6[NO_{ads}][H_2O_{ads}][O_s^{\bullet-}] - k_A[HNO_{2\,ads}][O_s^{\bullet-}] \\ &\quad - k_9[HNO_{3ads}^-][O_s^{\bullet-}] - k_B[NO_{ads}][H_2O_{ads}][O_s^{\bullet-}] = 0 \end{aligned} \qquad 4.43$$

where $k_{\mathrm{A}} = k_7 + k_8$ and $k_{\mathrm{B}} = k_{10} + \dfrac{k_{11}}{[\mathrm{H_2O}]}$.

$$\left[\mathrm{O_s^{\bullet -}}\right] = \frac{k_1\left[\mathrm{h^+}\right]}{k_6\left[\mathrm{NO_{ads}}\right]\left[\mathrm{H_2O_{ads}}\right] + k_{\mathrm{A}}\left[\mathrm{HNO_{2\,ads}}\right] + k_9\left[\mathrm{HNO^-_{3ads}}\right] + k_B\left[\mathrm{NO_{2\,ads}}\right]\left[\mathrm{H_2O_{ads}}\right]} \qquad 4.44$$

$$r_{h^+} = \alpha I - k_1[\mathrm{h^+}] - k_2[\mathrm{e^-}][\mathrm{h^+}] = 0 \qquad 4.45$$

$$r_{\mathrm{e^-}} = \alpha I - k^*_{e^-}[\mathrm{e^-}] - k_2[\mathrm{e^-}][\mathrm{h^+}] = 0 \qquad 4.46$$

where, $k^*_{e^-} = k_{e^-}[\mathrm{O_{2\,ads}}] = k_{e^-}\dfrac{K_{\mathrm{O_2}}[\mathrm{S^*}][\mathrm{O_2}]}{1 + K_{\mathrm{O_2}}[\mathrm{S^*}][\mathrm{O_2}]}$.

$$[\mathrm{h^+}] = \frac{\sqrt{k^{*2}_{e^-}k_1^2 + 4\alpha I k^*_{e^-}k_2k_1} - k^*_{e^-}k_1}{2k_2k_1} \qquad 4.47$$

$$\left[\mathrm{O_s^{\bullet -}}\right] = \frac{\dfrac{\sqrt{k^{*2}_{\mathrm{e^-}}k_1^2 + 4\alpha I k^*_{\mathrm{e^-}}k_1} - k^*_{\mathrm{e^-}}k_1}{2k_2}}{2k_6\left[\mathrm{NO_{ads}}\right]\left[\mathrm{H_2O_{ads}}\right] + \dfrac{k_8}{k_{\mathrm{A}}}k_6\left[\mathrm{NO_{ads}}\right]\left[\mathrm{H_2O_{ads}}\right] + k_B\left[\mathrm{NO_{2\,ads}}\right]\left[\mathrm{H_2O_{ads}}\right]} \qquad 4.48$$

Finally, the reaction rates of NO and $\mathrm{NO_2}$ become:

$$r_{\mathrm{NO}} = -\frac{1}{2}\,\frac{1}{2 + \dfrac{k_8}{k_A} + \dfrac{k_B K_{\mathrm{NO_2}}[\mathrm{NO_2}]}{k_6 K_{\mathrm{NO}}[\mathrm{NO}]}}\left(\sqrt{\beta^2 + 4\alpha I\beta} - \beta\right) \qquad 4.49$$

$$r_{\mathrm{NO_2}} = \frac{1}{2}\,\frac{\left(\dfrac{k_7}{k_A}k_6K_{\mathrm{NO}}[\mathrm{NO}] - k_BK_{\mathrm{NO_2}}[\mathrm{NO_2}]\right)}{2k_6K_{\mathrm{NO}}[\mathrm{NO}] + \dfrac{k_8}{k_A}k_6K_{\mathrm{NO}}[\mathrm{NO}] + k_BK_{\mathrm{NO_2}}[\mathrm{NO_2}]}\left(\sqrt{\beta^2 + 4\alpha I\beta} - \beta\right) \qquad 4.50$$

where $\beta = \dfrac{k^*_{e^-}k_1}{k_2}$.

According to Brouwers and co-workers [39, 41, 42], a plug flow can be used to describe the consumption/generation of NO and $\mathrm{NO_2}$ at the photoreactor. Following the mass balance equations for this type of reactor at steady-state and the obtained reaction rate expressions (equations 4.49 and 4.50), the following can be written:

$$v_{air} \frac{dC}{dx} = a_v r \qquad 4.51$$

Considering as boundary condition that $C(x=0) = C_{in}$, where C_{in} is the feed concentration, the previous equation can be rearranged:

$$v_{air} \frac{C_{i+1} - C_i}{x_{i+1} - x_i} = a_v r \qquad 4.52$$

which implements the Euler method that can be applied to obtain NO and NO_2 concentrations profiles along the reactor axial coordinate *x*. This method, however, introduces numerical dispersion such as Pe = 2*N* [43], where Pe is the peclet number and *N* is the number of discretising intervals. Replacing the reaction rate equations (4.49 and 4.50) in equation 4.52:

$$[\text{NO}]_{i+1} = -\frac{1}{2} \frac{x_{\text{i+1}} - x_i}{v_{air}} a_v \frac{k_6 K_{\text{NO}} [\text{NO}]_{\text{i}}}{\left(2 + \frac{k_8}{k_A}\right) k_6 K_{\text{NO}} [\text{NO}]_{\text{i}} + k_B K_{\text{NO}_2} [\text{NO}_2]_{\text{i}}} \left(\sqrt{\beta^2 + 4\alpha I \beta} - \beta\right) + [\text{NO}]_i \qquad 4.53$$

$$[\text{NO}_2]_{i+1} = \frac{1}{2} \frac{x_{i+1} - x_i}{v_{air}} a_v \left[\frac{\left(\frac{k_7}{k_A} k_6 K_{\text{NO}} [\text{NO}]_i - k_B K_{\text{NO}_2} [\text{NO}_2]_i \right)}{2k_6 K_{\text{NO}} [\text{NO}]_i + \frac{k_8}{k_A} k_6 K_{\text{NO}} [\text{NO}]_i + k_B K_{\text{NO}_2} [\text{NO}_2]_i} \right] \left(\sqrt{\beta^2 + 4\alpha I \beta} - \beta\right) + [\text{NO}_2]_i \qquad 4.54$$

The active surface area per unit reactor volume $\left(a_v\right)$ is obtained from:

$$a_v = \frac{D_{\text{TiO}_2} A_{\text{act}}}{V_{\text{reactor}}} \qquad 4.55$$

The air velocity $\left(v_{air}\right)$ was obtained from the Reynolds number – equation 4.56.

$$\text{Re} = \frac{v_{\text{air}} D_{\text{h}} \rho_{\text{air}}}{\eta_{\text{air}}} \qquad 4.56$$

where ρ_{air} is the air density and η_{air} is the dynamic viscosity. The hydraulic diameter for a rectangular reactor can be obtained from:

$$D_h = \frac{4A_\mathrm{s}}{P_\mathrm{reactor}} = \frac{2\mathrm{WH}}{\mathrm{W+H}} \qquad 4.57$$

where P_reactor is the perimeter of reactor, A_S is the cross-sectional area, W is the width of reactor and H is the height of reactor.

Thus, the Reynolds number can be rewritten as follows:

$$\mathrm{Re} = \frac{2Q}{(\mathrm{W+H})\mu_{air}} \qquad 4.58$$

where μ_{air} is the kinematic viscosity, equal to $\frac{\eta_\mathrm{air}}{\rho_\mathrm{air}}$.

Parameters in equations 4.53 and 4.54 were obtained fitting these equations to the experimental values using "Solver" optimization tool from Microsoft Excel. Experimental data are from the design of experiments applied to factors *RH*, *I*, $[\mathrm{NO}]_\mathrm{in}$ and *τ*. However, the phenomenological model only considers $[\mathrm{NO}]_\mathrm{in}$, $[\mathrm{NO_2}]_\mathrm{in}$ and *I* as independent variables (factors). *RH* factor plays a minor role on the NO conversion and selectivity and its contribution can be neglected. Nevertheless, the residence time has a significant impact in the NO conversion and selectivity. Consequently, the parameters of the phenomenological model were estimated separately for three values of residence time – Table 4.8.

Table 4.8. Phenomenological model parameters for different residence times.

	τ / s		
Model Parameters	**0.43**	**1.3**	**2.1**
k_6K_NO / m^7 mol^{-2} s^{-1}	3.09×10^{-4}	8.08×10^{-4}	1.50×10^{-4}
$k_BK_\mathrm{NO_2}$ / m^7 mol^{-2} s^{-1}	5.31×10^{-4}	1.92×10^{-4}	1.32×10^{-5}
α / mol W^{-1} s^{-1}	1.56×10^{-3}	5.17×10^{-4}	7.79×10^{-4}
β / mol m^{-2} s^{-1}	1.21×10^{-4}	7.21×10^{-6}	1.15×10^{-6}
k_7/k_A	9.99×10^{-4}	1.00×10^{-4}	1.00×10^{-1}
k_8/k_A	9.99×10^{-1}	1.00×10^{0}	1.00×10^{-1}

Figures 4.8 and 4.9 show the parity plots of experimental and simulated exiting concentrations of NO and NO_2 for three values of residence time. A reasonably good agreement was achieved between experimental and model values, mainly for smaller values of residence time. Since the feed flow rate was kept constant, smaller residence times were obtained decreasing the length of the active photocatalyst film. Since the size of the photoreactor is constant, smaller photocatalyst film lengths should have a more developed flow pattern, allowing the phenomenological model to better represent the corresponding experimental values. Actually, increasing the number of discrete integration elements of the phenomenological model (Pe = 2*N*) it was possible to get a slightly better fitting of the experimental values for the highest residence time.

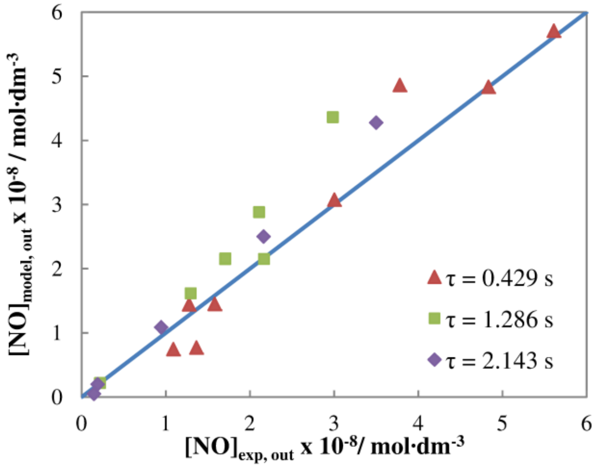

Figure 4.8. Parity plot of experimental vs. predicted exiting NO concentration.

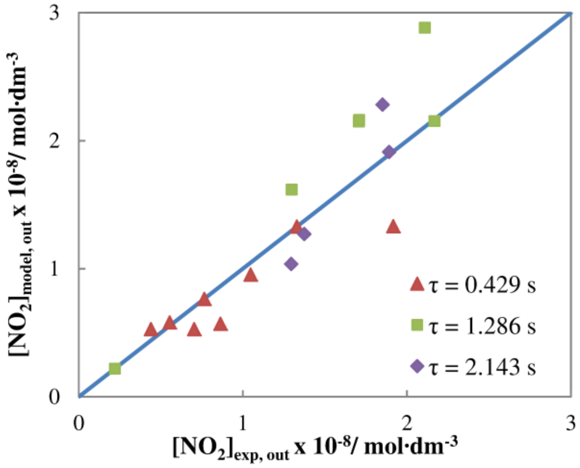

Figure 4.9. Parity plot of experimental vs. predicted exiting NO_2 concentration.

4.4 Conclusions

In this chapter, the influence of operating conditions on NO photoabatement was studied. The operating conditions considered were the relative humidity, irradiance, NO inlet concentration and residence time, and the evaluated responses were NO conversion and selectivity to other species rather than NO_2. The response hyper-surfaces were obtained fitting a second order polynomial equation to the experimental data using a response surface methodology (RSM) approach. For the range of operating conditions considered it was concluded that increasing in irradiance and residence time results in higher NO conversion and selectivity values. The NO inlet concentration affects differently conversion and selectivity; conversion increases for lower inlet concentrations, while selectivity decreases. Conversion and selectivity peak as a function of the relative humidity for $RH \approx 25$ %. The operating conditions that maximize NO conversion and selectivity were $RH = 25$ %, $I = 15\ W \cdot m^{-2}$, $[NO]_{in} = 1.5$ ppm and $\tau = 2.1$ s. Finally, it was concluded experimentally that oxygen was required for the NO photooxidation.

The adsorption equilibrium isotherms of water vapor, nitrogen oxide and nitrogen dioxide on P25 were obtained at 25 ºC and fitted to known models. For low pressures, the Henry's constants for NO, NO_2 are respectively $21\ mol \cdot bar^{-1} \cdot kg^{-1}$, $198\ mol \cdot bar^{-1} \cdot kg^{-1}$ and for H_2O is $111\ mol \cdot bar^{-1} \cdot kg^{-1}$ up to *ca.* 25 % RH.

It was recently concluded that the usual photooxidation model based on the intermediated hydroxyl radical could not explain the all reaction process; instead, the photooxidation intermediated by lattice oxygen radicals is now the preferred model. Accordingly, a phenomenological model assuming the adsorption of reagents in active sites of titanium dioxide and oxidation by lattice oxygen radicals and reduction intermediated by superoxide ion was proposed for the first time for NO photoabatement. The proposed model was fitted to the experimental values and a good agreement was achieved.

Acknowledgements

Joana Ângelo and Pedro Magalhães are grateful to the Portuguese Foundation for Science and Technology (FCT) for their PhD Grants (Ref: SFRH/BD/79974/2011 and Ref: SFRH/BD/78827/2011, respectively). Luísa Andrade acknowledges European Research Council for funding within project BI-DSC – Building Integrated Dye sensitized Solar Cells (Contract Number: 321315).

References

1. Fujishima, A., Rao, T.N., and Tryk, D.A., *Titanium dioxide photocatalysis.* Journal of Photochemistry and Photobiology, C: Photochemistry Reviews, 1(1): p. 1-21, **2000**
2. Devahasdin, S., Fan Jr, C., Li, K., and Chen, D.H., *TiO_2 photocatalytic oxidation of nitric oxide: transient behavior and reaction kinetics.* Journal of Photochemistry and Photobiology, A: Chemistry, 156(1–3): p. 161-170, **2003**
3. Paz, Y., *Application of TiO_2 photocatalysis for air treatment: Patents' overview.* Applied Catalysis, B: Environmental, 99(3–4): p. 448-460, **2010**
4. Ângelo, J., Andrade, L., Madeira, L.M., and Mendes, A., *An overview of photocatalysis phenomena applied to NO_x abatement.* Journal of Environmental Management, 129: p. 522-539, **2013**
5. Dillert, R., Engel, A., Grosse, J., Lindner, P., and Bahnemann, D.W., *Light intensity dependence of the kinetics of the photocatalytic oxidation of nitrogen(II) oxide at the surface of TiO_2.* Physical Chemistry Chemical Physics, 15(48): p. 20876-86, **2013**
6. Ballari, M.M., Yu, Q.L., and Brouwers, H.J.H., *Experimental study of the NO and NO_2 degradation by photocatalytically active concrete.* Catalysis Today, 161(1): p. 175-180, **2011**
7. Munoz-Batista, M.J., Ballari, M.M., Cassano, A.E., Alfano, O.M., Kubacka, A., and Fernandez-Garcia, M., *Ceria promotion of acetaldehyde photo-oxidation in a TiO_2-based catalyst: a spectroscopic and kinetic study.* Catalysis Science & Technology, 5(3): p. 1521-1531, **2015**
8. Ollis, D.F., *Kinetic Disguises in Heterogeneous Photocatalysis.* Topics in Catalysis, 35(3): p. 217-223, **2005**
9. Ohko, Y., Nakamura, Y., Negishi, N., Matsuzawa, S., and Takeuchi, K., *Photocatalytic oxidation of nitrogen monoxide using TiO_2 thin films under continuous UV light illumination.* Journal of Photochemistry and Photobiology A: Chemistry, 205(1): p. 28-33, **2009**
10. Ohko, Y., Nakamura, Y., Negishi, N., Matsuzawa, S., and Takeuchi, K., *Unexpected release of HNO_3 and related species from UV-illuminated TiO_2*

surface into air in photocatalytic oxidation of NO_2. Environmental Chemistry Letters, 8(3): p. 289-294, **2009**

11. Upadhya, S. and Ollis, D.F., *Simple Photocatalysis Model for Photoefficiency Enhancement via Controlled, Periodic Illumination.* The Journal of Physical Chemistry B, 101(14): p. 2625-2631, **1997**
12. Brosillon, S., Lhomme, L., Vallet, C., Bouzaza, A., and Wolbert, D., *Gas phase photocatalysis and liquid phase photocatalysis: Interdependence and influence of substrate concentration and photon flow on degradation reaction kinetics.* Applied Catalysis B: Environmental, 78(3–4): p. 232-241, **2008**
13. Ochiai, T. and Fujishima, A., *Photoelectrochemical properties of TiO_2 photocatalyst and its applications for environmental purification.* Journal of Photochemistry and Photobiology C: Photochemistry Reviews, 13(4): p. 247-262, **2012**
14. Ishibashi, K.-i., Fujishima, A., Watanabe, T., and Hashimoto, K., *Quantum yields of active oxidative species formed on TiO_2 photocatalyst.* Journal of Photochemistry and Photobiology A: Chemistry, 134(1–2): p. 139-142, **2000**
15. Micic, O.I., Zhang, Y., Cromack, K.R., Trifunac, A.D., and Thurnauer, M.C., *Trapped holes on titania colloids studied by electron paramagnetic resonance.* The Journal of Physical Chemistry, 97(28): p. 7277-7283, **1993**
16. Montoya, J.F., Ivanova, I., Dillert, R., Bahnemann, D.W., Salvador, P., and Peral, J., *Catalytic Role of Surface Oxygens in TiO_2 Photooxidation Reactions: Aqueous Benzene Photooxidation with $Ti^{18}O_2$ under Anaerobic Conditions.* The Journal of Physical Chemistry Letters, 4(9): p. 1415-1422, **2013**
17. Montoya, J.F., Peral, J., and Salvador, P., *Surface Chemistry and Interfacial Charge-Transfer Mechanisms in Photoinduced Oxygen Exchange at O_2–TiO_2 Interfaces.* ChemPhysChem, 12(5): p. 901-907, **2011**
18. Xu, Y. and Langford, C.H., *Variation of Langmuir adsorption constant determined for TiO_2-photocatalyzed degradation of acetophenone under different light intensity.* Journal of Photochemistry and Photobiology A: Chemistry, 133(1–2): p. 67-71, **2000**
19. Ollis, D.F., *Kinetics of Liquid Phase Photocatalyzed Reactions: An Illuminating Approach.* The Journal of Physical Chemistry B, 109(6): p. 2439-2444, **2005**

20. Chin, S., Park, E., Kim, M., Jeong, J., Bae, G.N., and Jurng, J., *Preparation of TiO_2 ultrafine nanopowder with large surface area and its photocatalytic activity for gaseous nitrogen oxides.* Powder Technology, 206(3): p. 306-311, **2011**
21. Herrmann, J.M., *Heterogeneous photocatalysis: State of the art and present applications.* Topics in Catalysis, 34(1-4): p. 49-65, **2005**
22. Wang, H., Wu, Z., Zhao, W., and Guan, B., *Photocatalytic oxidation of nitrogen oxides using TiO_2 loading on woven glass fabric.* Chemosphere, 66(1): p. 185-190, **2007**
23. Martinez, T., Bertron, A., Ringot, E., and Escadeillas, G., *Degradation of NO using photocatalytic coatings applied to different substrates.* Building and Environment, 46(9): p. 1808-1816, **2011**
24. Águia, C., Ângelo, J., Madeira, L.M., and Mendes, A., *Photo-oxidation of NO using an exterior paint - Screening of various commercial titania in powder pressed and paint films.* Journal of Environmental Management, 92(7): p. 1724-1732, **2011**
25. Montgomery, D.C., *Design and Analysis of Experiments*, New York: John Wiley & Sons, Vol. **2001**.
26. Andreson, M.J. and Whitcomb, P.J., *RSM Simplified: Optimizing Processes Using Response Surface Methods For Design of Experiments*, New York: Productivity Press, Vol. **2005**.
27. Campo, M.C., Lagorsse, S., Magalhães, F.D., and Mendes, A., *Comparative study between a CMS membrane and a CMS adsorbent: Part II. Water vapor adsorption and surface chemistry.* Journal of Membrane Science, 346(1): p. 26-36, **2010**
28. Marques, J., Oliveira, L.F., Pinto, R.T., Coutinho, P.J.G., Parpot, P., Góis, J.R., Coelho, J.F.J., Magalhães, F.D., and Tavares, C.J., *Release of Volatile Compounds from Polymeric Microcapsules Mediated by Photocatalytic Nanoparticles.* International Journal of Photoenergy, 2013: p. 9, **2013**
29. Louit, G., Foley, S., Cabillic, J., Coffigny, H., Taran, F., Valleix, A., Renault, J.P., and Pin, S., *The reaction of coumarin with the OH radical revisited: hydroxylation product analysis determined by fluorescence and chromatography.* Radiation Physics and Chemistry, 72(2–3): p. 119-124, **2005**

30. Czili, H. and Horváth, A., *Applicability of coumarin for detecting and measuring hydroxyl radicals generated by photoexcitation of TiO_2 nanoparticles.* Applied Catalysis B: Environmental, 81(3–4): p. 295-302, **2008**
31. Černigoj, U., Štangar, U.L., Trebše, P., and Sarakha, M., *Determination of catalytic properties of TiO_2 coatings using aqueous solution of coumarin: Standardization efforts.* Journal of Photochemistry and Photobiology A: Chemistry, 201(2–3): p. 142-150, **2009**
32. Montoya, J.F., Peral, J., and Salvador, P., *Comprehensive Kinetic and Mechanistic Analysis of TiO_2 Photocatalytic Reactions According to the Direct–Indirect Model: (I) Theoretical Approach.* The Journal of Physical Chemistry C, 118(26): p. 14266-14275, **2014**
33. Ferreira, D., Magalhães, R., Taveira, P., and Mendes, A., *Effective Adsorption Equilibrium Isotherms and Breakthroughs of Water Vapor and Carbon Dioxide on Different Adsorbents.* Industrial & Engineering Chemistry Research, 50(17): p. 10201-10210, **2011**
34. Do, D.D., *Adsorption Analysis: Equilibria and Kinetics*. 916, Vol. **1998**.
35. Müller, E.A., Rull, L.F., Vega, L.F., and Gubbins, K.E., *Adsorption of Water on Activated Carbons: A Molecular Simulation Study.* The Journal of Physical Chemistry, 100(4): p. 1189-1196, **1996**
36. Ferreira, D., Magalhães, R., Bessa, J., Taveira, P., Sousa, J., Whitley, R.D., and Mendes, A., *Study of AgLiLSX for Single-Stage High-Purity Oxygen Production.* Industrial & Engineering Chemistry Research, 53(40): p. 15508-15516, **2014**
37. Ruthven, D.M., *Principles of Adsorption and Adsorption Processes*: Wiley, Vol. **1984**.
38. Xiang, Q., Yu, J., and Wong, P.K., *Quantitative characterization of hydroxyl radicals produced by various photocatalysts.* Journal of Colloid and Interface Science, 357(1): p. 163-167, **2011**
39. Yu, Q.L., Ballari, M.M., and Brouwers, H.J.H., *Indoor air purification using heterogeneous photocatalytic oxidation. Part II: Kinetic study.* Applied Catalysis B: Environmental, 99(1–2): p. 58-65, **2010**
40. Hashimoto, K., Wasada, K., Osaki, M., Shono, E., Adachi, K., Toukai, N., Kominami, H., and Kera, Y., *Photocatalytic oxidation of nitrogen oxide over*

titania–zeolite composite catalyst to remove nitrogen oxides in the atmosphere. Applied Catalysis B: Environmental, 30(3–4): p. 429-436, **2001**

41. Hunger, M., Hüsken, G., and Brouwers, H.J.H., *Photocatalytic degradation of air pollutants — From modeling to large scale application.* Cement and Concrete Research, 40(2): p. 313-320, **2010**
42. Ballari, M.M., Hunger, M., Hüsken, G., and Brouwers, H.J.H., *NO_x photocatalytic degradation employing concrete pavement containing titanium dioxide.* Applied Catalysis B: Environmental, 95(3–4): p. 245-254, **2010**
43. Wankat, P.C., *Separation Process Engineering*: Pearson Education, Vol. **2006**.

PART III: Chapter 5

Final Conclusions

Chapter 5

Conclusions and Future Work

The increasing levels of air pollution in the last decades and their consequences on urban environments, human health and population well-being are motivating the development of new regulations to control the pollutants emissions. Several methods and technologies have been developed in order to control NO_x emissions and, in particular, photocatalysis with titanium dioxide appears as a promising and effective technology for NO_x abatement. The photocatalytic activity of titanium dioxide semiconductor has been widely studied and it is known that it strongly depends on several operating and process conditions when used in continuous reactors, namely: inlet concentration of the pollutant; air humidity; light intensity and light spectrum; flow rate/residence time; photocatalyst concentration per active area; substrates where TiO_2 is deposited. On the other hand, it has been also reported that TiO_2 photocatalytic activity can be enhanced by three main approaches: bandgap tuning for visible light harvesting, electron/hole recombination inhibition and promotion of the forward reaction at the surface of the photocatalyst. Nevertheless, several studies refer that a higher surface area should be an important feature to enhance the photocatalytic activity and TiO_2 immobilization should be the way of get it. Paint coatings are an efficient way of immobilizing photocatalysts as they present a 3D layer where TiO_2 nanoparticles are available for photocatalysis. However, a major challenge to immobilize TiO_2 material is to find a way of doing it in a photodegradation-resistant substrate.

A commercial water-based paint (vinyl base) was reformulated to incorporate photocatalytic titanium dioxide and to be used for NO_x photoabatement. The commercial titanium dioxide P25 (Evonik) and PC500 (Cristal) were chosen and four different paints were produced. In the formulation of these new paints half of the pigmentary TiO_2 of the original paint was replaced by a photocatalytic TiO_2 and the remained pigmentary TiO_2 was either kept or replaced by calcium carbonate extender. The effect of these variations was assessed by means of their photocatalytic activity according to the standard ISO 22197-1:2007. The two studied parameters were NO conversion and selectivity. The paints without pigmentary TiO_2 presented the highest conversion of NO; indeed, it was concluded that this component blocks the light harvesting, decreasing the photocatalytic activity. On the other hand, paints with PC500 photocatalyst also originated better NO conversion and selectivity comparatively to P25-based paints. PC500 shows a larger surface area (smaller TiO_2 particles) than P25, which in principle improves the photoactivity. The main goal of immobilizing photocatalysts in a paint matrix is its usage in house facades or roads in order to decrease the pollution levels in atmosphere, and so outdoor tests were conducted for real-field performance and stability evaluation. All paints showed a NO conversion higher than 80 %. The best performing paint (paint with PC500 and calcium carbonate) showed a NO conversion of about 95 %. The high photocatalytic performance of this paint was ascribed to the photocatalyst high activity, to the removal of the pigmentary TiO_2 and to the PVC/CPVC ratio higher than one. This paint displays, however, some chalking; titanium dioxide also degrades the paint binder allowing pigments and extenders to come out from the paint film surface. This study concluded that the use of paint coatings is one of the best approaches to immobilize TiO_2 since they create a 3D layer where TiO_2 nanoparticles are available for photocatalysis.

Photocatalysis is a photoelectrochemical phenomenon where the semiconductor absorbs light and a pair electron-hole is created; indeed, the recombination of these pairs is a key limitation for photocatalytic activity. Thus, the study of electrical behavior of semiconductors is crucial for acquiring relevant information to improve the photocatalytic efficiency. Within this thesis, P25 and P25/graphene composite were studied based on photocatalytic efficiency and electrochemical characterization. P25/graphene composite showed a higher photocatalytic activity than bare P25. Graphene improves the performance of the photocatalyst; EIS was used for assessing the charge transfer within the two photocatalysts. The values of charge transfer resistance and space charge capacitance were obtained in a three-electrode configuration. For that, a “full” Randles electrical analogue was used, which proved to fit quite well the experimental results. The P25/graphene composite exhibited lower values of R_{CT} and C_{SC}, supporting the observed higher photocatalytic activity for NO degradation. In a composite sample the probability of electron/hole recombination decreases because the charge mobility to the surface was enhanced by graphene presence. Furthermore, the TiO_2/graphene photocatalyst has also the advantage of enabling the absorption of a wider range of wavelengths, corresponding to a band gap of 2.9 eV, so allowing its use under visible light photocatalysis. Electrochemical impedance spectroscopy is essential to discriminate these different phenomena, contributing to the production of more efficient photocatalysts.

NO photooxidation depends on several operating conditions, so a design of experiments methodology was implemented to study the influence of humidity, irradiance, inlet NO concentration and residence time on NO conversion and selectivity. This study allowed concluding that NO conversion and selectivity were favored by the irradiance and residence time and peak at ca. $RH = 25$ %. NO concentration, on the other hand, favors the selectivity while NO conversion is favored for lower NO concentrations. A desirability function was applied to optimize the NO conversion and selectivity, assigning the same weight to each response; the obtained optimal operating conditions were $RH = 25$ %, $I = 15$ W·m^{-2}, $[NO]_{in} = 1.5$ ppm and $\tau = 2.143$ s.

Finally, and following the design of experiments study, a phenomenological model of NO photooxidation was proposed using P25 as reference photocatalyst. The proposed model assumes that lattice oxygen radicals are the main intermediate species responsible for the NO oxidation and the injected electron reacts with oxygen to produce superoxide ions. The adsorption equilibrium isotherms of H_2O, NO and NO_2 were obtained experimentally by the gravimetric method.

Most of photocatalytic studies are empirical and only recently this tendency is being inverted. A more fundamental/systematic approach must be followed if significant advancements are envisioned. The development of photocatalytic materials can be divided into photocatalyst optimization and optimization of substrate to incorporate the photocatalyst. When a photocatalyst is prepared, several properties need to be considered, such as band gap, band edges, recombination rate and charge transfer resistance. The band gap of semiconductors determines the fraction of solar spectrum that they can absorb, which has a great relevance to guarantee the generation of pairs e^-/h^+. On the other hand, the band edges positions (valence band and conduction band position) indicate the thermodynamic energy of the electron/hole available for the redox reactions. Finally, lower recombination rates and charge transfer resistances conduct to more efficient photocatalysts. Thus, the optimization of photocatalyst should be focused in bandgap tuning to visible light harvesting and minimization of electron-hole recombination and charge transfer resistances. The use of visible light with titanium dioxide can be obtained by semiconductor sensitization, doping, co-doping, among others. In case of recombination, an improvement in photocatalyst particles is crucial; the recombination is favored by particle defects and it is less probable for small (nano) particles. These two points are controversial because the production of nanoparticles brings more surface defects, so a balance is needed between particles size and number of particle defects. That way, synthesis routes need to be explored and improved.

The choice of substrate to incorporate the titanium dioxide needs to follow some specific requirements. The support has to be chemically inert and compatible with the environment, it should have a large specific surface area and provide a good adhesion to the semiconductor particles. In the particular case of photocatalytic paints, it has been reported high efficiencies for NO degradation, despite the chalking of the paint matrix. Thus, further studies must be conducted to minimize this degradation pathway. The use of different binders and extenders are one of the approaches that should be followed; perfluoro, silicone, silicate or acrylic base binders are more stable towards photodegradation and should be considered to prepare the paint coatings. Within this thesis calcium carbonate extender was studied but others as barium sulphate, talcum or other carbonates should be assessed.

The proposed phenomenological model considers only lattice oxygen radicals as the intermediate species for NO photooxidation. A model considering two competitive mechanisms for NO oxidation should be developed, one intermediated by TiO_2 lattice oxygen radical, and the other intermediated by $OH^{\bullet}$ radical – conventional approach.

Additionally, a computational fluid dynamics (CFD) approach can be very useful to determine the kinetic parameters of NO photooxidation mechanism. Since the photocatalytic degradation of NO is influenced by several operating conditions and the use of CFD approach allows describing in detail the flow pattern at the reactor and the species transport through the photocatalytic layer, more accurate kinetic parameters could be obtained. This will strongly contribute for a deeper understanding of the photooxidation mechanism of NO on titanium dioxide.